

VON KÁRMÁN GAS DYNAMICS FACILITY

ARO, INC.

Technical Developments



DISTRIBUTION STATEMENT A
Approved for Public Release
Distribution Unlimited

1964

20040123 098

ARNOLD ENGINEERING DEVELOPMENT CENTER
AIR FORCE SYSTEMS COMMAND
UNITED STATES AIR FORCE



Professor Theodore von Kármán, 1881-1963

*Portrait by Marie Elizabeth Wrede,
drawn in Aachen, Germany in April 1962*

Add to Shopping Cart

Save for Later

Technical Reports Collection

Citation Format: Full Citation (1F)

Accession Number :

AD0427313

Citation Status:

Active

Citation Classification:

Unclassified

SBI Site Holding Symbol:

RSIH

Corporate Author:

ARNOLD ENGINEERING DEVELOPMENT CENTER ARNOLD AFS TN

Unclassified Title:

PUBLICATIONS OF VON KARMAN GAS DYNAMICS FACILITY, ARO, INC.

Title Classification:

Unclassified

Report Date:

01 Jan 1964

Media Count:

1 Page(s)

Cost:

\$7.00

Report Classification:

Unclassified

Distribution Statement:

Availability: Document partially illegible.

Descriptors:

(*REPORTS, , RESEARCH MANAGEMENT), AERODYNAMIC CHARACTERISTICS, THERMODYNAMICS, HYPERSONIC WIND TUNNELS, SUPERSONIC WIND TUNNELS, TEST, INSTRUMENTATION, HYPERVELOCITY GUNS, TERMINAL BALLISTICS, CALIBRATION

Abstract:

This is a listing of widely-distributed publications (reports, articles, proceedings, etc.) of the von Karman Gas Dynamics Facility, ARO, Inc., issued before January 1, 1964. The publications are listed in chronological order according to subject and an author index is provided. (Author)

Abstract Classification:

Unclassified

Annotation:

Publications of the von karman gas dynamics facility ARO, Inc.

Distribution Limitation(s):

01 - APPROVED FOR PUBLIC RELEASE

23 - DOCUMENT PARTIALLY ILLEGIBLE

Source Code:

042550

Document Location:

DTIC

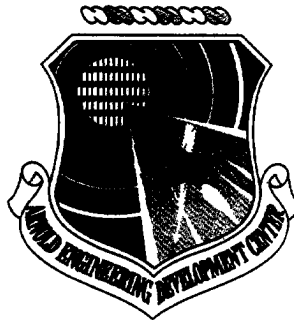
DTIC -

We are surplusing the attached report.
Can you use for your collection?

VON KÁRMÁN GAS DYNAMICS FACILITY

ARO, INC.

Technical Developments



1964

ARNOLD ENGINEERING DEVELOPMENT CENTER
AIR FORCE SYSTEMS COMMAND
UNITED STATES AIR FORCE

CONTENTS

	<u>Page</u>
INTRODUCTION - J. Lukasiewicz.	1
► AERODYNAMICS	5
ANALYTICAL STUDIES.	5
The Inviscid Flow Field of Blunt, Axisymmetric Bodies - C. H. Lewis.	5
The Blast-Hypersonic Flow Analogy - J. Lukasiewicz and C. H. Lewis	8
Skin Friction and Heat Transfer for Laminar Boundary-Layer Flows - C. H. Lewis.	11
Thermodynamic Properties of High Temperature Air and Nitrogen and Their Applications - C. H. Lewis and Martin Grabau.	14
SUPERSONIC AND HYPERSONIC FLOWS:	
VISCOUS INTERACTION AND LOW-DENSITY	17
Hypersonic Aerodynamics of Blunt, Slender Cones - J. D. Whitfield.	17
Research on Low-Density, Hypersonic Flow - J. L. Potter	21
Research on Boundary-Layer Transition - J. L. Potter and J. D. Whitfield	25
AERODYNAMIC CONTROLS.	29
On Control Surfaces Submerged in Thick Boundary Layers - J. D. Gray	29
Interactions Produced by Sonic Lateral Jets Located on Surfaces in a Supersonic Stream - W. T. Strike and C. J. Schueler.	30
BOUNDARY-LAYER CONTROL AT SUPERSONIC SPEEDS	33
Influence of Suction on Turbulent Boundary- Layer Separation - W. T. Strike.	33
Laminar Flow Control - C. J. Schueler and S. R. Pate	34
► HYPERVELOCITY IMPACT	39
Formation of Craters - E. H. Goodman	39
Target Rear Surface Fracture Resulting from High-Speed Impact - R. Kinslow.	41
► EXPERIMENTAL TECHNIQUES.	47
SUPERSONIC AND HYPERSONIC TUNNELS	47
Development of Air Heaters for Continuous, Hypersonic Tunnels - R. M. James	47
Development of Continuous, Hypersonic Tunnels - J. C. Sivells.	49
THE HOTSHOT STORY	52
Development of Hotshot-Type Wind Tunnels - J. Lukasiewicz and R. Jackson.	52
Inductance Energy Storage Systems - R. R. Walker, III.	58
LOW-DENSITY FACILITY.	61
Low-Density, Hypersonic (LDH) Wind Tunnel "L" - J. L. Potter.	61
HYPERVELOCITY RANGES.	64
Development of Launchers for Aeroballistic and Impact Ranges - W. B. Stephenson	64
Hypervelocity Range Measurements - P. L. Clemens.	67
INSTRUMENTATION	72
Dynamic Stability Measurements - L. K. Ward	72
Transducers - D. S. Bynum.	73

INTRODUCTION

By

J. Lukasiewicz, Chief

VKF, ARO, Inc.

The von Kármán Gas Dynamics Facility (VKF) is one of the four major laboratories of the Arnold Engineering Development Center (AEDC), Air Force Systems Command, USAF, located near Tullahoma, Tennessee. The test facilities at the AEDC, including the VKF, are operated by a private company, ARO, Inc. (subsidiary of Sverdrup and Parcel, Inc.) under a contract with the U.S. Air Force.

The AEDC's main purpose is to provide advanced and large-scale test facilities for use by the Air Force, other government agencies, and contractors. The VKF's responsibility is in the fields of supersonic and hypersonic aerodynamics and hypervelocity impact.

The tests which have been conducted in the VKF included support for the following major weapon and space systems:

USAF: F103, F105, F106, B58, B70, X15, Dynasoar, Atlas, Titan, Minuteman, Skybolt
U.S. Army: Redstone, Pershing, Nike-Zeus
U.S. Navy: Polaris, Sparrow
NASA: X15, Mercury, Gemini, Apollo, Saturn

Actually, components of practically all of the existing and now planned weapon and space systems have been tested in the VKF. Also, many tests of a more basic nature have been made for USAF, ARPA, and other agencies.

In addition to conducting tests for the industry, a considerable amount of VKF's effort is spent in internal research and in the development of advanced test facilities. The purpose of this publication is to acquaint the reader with these latter activities; the contributions here collected were authored by senior members of the VKF staff and prepared with the object of giving worthwhile technical information rather than a mere summary of what has been already published. The contributions are assembled under more general subject headings and are briefly introduced to better orient the reader in the purpose and significance of the particular investigations.

Inasmuch as VKF is probably one of the largest and most active installations of its kind, it may be of interest to some readers to consider in general the present performance of VKF's experimental facilities and development, now underway, of the new ones. As regards description of present VKF facilities, the reader is referred to the widely distributed VKF brochures issued in 1959, 1960, and 1961 and to the frequently revised Vol. 4 of the AEDC Test Facilities Handbook.

PRESENT PERFORMANCE OF VKF TUNNELS

The 12-in. supersonic intermittent Tunnel D was the first to come into operation in VKF in 1953. Between 1958 and 1962 all other VKF tunnels began to operate, the latest addition being the 100-in. test section, Mach 20, hotshot-type Tunnel F. A listing of VKF wind tunnels and of their major characteristics is given in Table 1. Figure 1 indicates the tunnels' aerodynamic range of operation in terms of Reynolds number and Mach number, the former being based on test section height or diameter, or, in the case of hotshot-type and low density tunnels, on diameter of the isentropic and uniform flow core. This being the case, the Reynolds number as shown is indicative of the model size. All of the tunnels listed are fully calibrated and instrumented for force, pressure, and heat-transfer tests.

It is evident from Fig. 1 that an extremely wide M-Re range is being covered by the VKF tunnels. This has proven to be most advantageous in many investigations, for example, in the studies of hypersonic, viscous interaction described in this collection.

Also included in Fig. 1 are some proposed future extensions of tunnels' performance. The Mach 10 Tunnel C is to be equipped with a Mach 12 nozzle and a suitable 2000°F air heater, to provide a choice of Mach 10 or Mach 12. Tunnel F operation is to be extended toward higher Reynolds numbers and lower Mach numbers. A larger, low-density, hypersonic (LDH) tunnel is proposed, covering higher Mach and Reynolds numbers and filling in the M-Re area between the present, small low-density Tunnel L and the large hotshot F.

Table 1
VKF Wind Tunnels

Tunnel	Type	Test Section Size, in.	Mach No. Range	P ₀ Range, psia	T ₀ , °K	Re/lft x 10 ⁻⁶ Range
A	Continuous	40 x 40	1.5-6	1-200	310-420	0.2-9.3
B	Continuous	50 diam	8	100-900	750	0.4-3.8
C	Continuous	50 diam	10	175-2000	1060	0.3-2.4
D	Intermittent	12 x 12	1.5-5	0.8-60	300	0.25-18.7
E	Intermittent	12 x 12	5-8	70-1300	310-750	0.9-14.6
H	Hotshot	50 diam	18-22	3,000-15,000	2500-4500	0.025-0.35
F	Hotshot	100 diam	16-22	3,000-15,000	2500-4500	0.025-0.35
L	Continuous Arc-Heated (Nitrogen, Argon)	1 diam (Core Size)	9-11	10-20	1500-4000	0.005-0.012

Note: A hotshot tunnel, having a 16-in. diam test section, is mentioned several times in this volume. The performance of this tunnel, no longer in existence, was similar, in terms of free-stream conditions, to that of the 50-in. hotshot H, listed above.

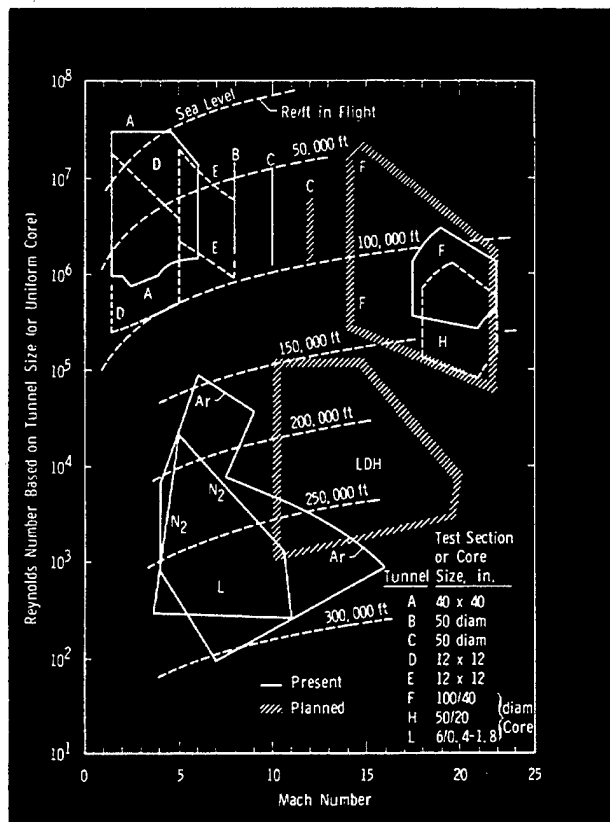


Fig. 1 Range of Operation of VKF Wind Tunnels

The choice of the coordinates in Fig. 1 is deliberate in that the wind tunnels shown provide true simulation in terms of Mach and Reynolds numbers only and do not purport to provide hypervelocity flow in which the so-called real gas effects are significant. In spite of the hopes which have been expressed by many laboratories (including the VKF) in the past of attaining hypervelocity flight simulation and duplication in wind tunnels, this goal has yet to be achieved. To date, the techniques used in the VKF to obtain relatively high stagnation temperatures (4000°K corresponding to 10,000 ft/sec) relied on application of electric arc discharge, either of short duration and large current, as in hotshot-type tunnels, or of continuous type, as in the low-density, hypersonic tunnel. Although successful and extremely useful in

Table 2
Hypervelocity Range Facilities

Range	Type	Size, ft	Pressure Range, mm Hg	Launcher Caliber, in.	Velocity
S-1	Impact	3-diam Target Chamber	10 ⁻⁴ - 760	0.3 or 0.5	26 kft/sec, 1/16-in. Al Sphere
S-2	Impact	6-diam Target Chamber	10 ⁻⁶ - 760	0.5	30 kft/sec, 1/8-in. Cu Sphere
K	Aeroballistics	100 x 6 diam	0.1 - 760	0.5 - 1	32 kft/sec, 0.5 gram
G*	Aeroballistics	1000 x 10 diam	15 x 10 ⁻³ - 760	2.5	*25 kft/sec, 250 grams

*Planned to start testing in 1964; estimated performance.

both applications, these techniques have been judged limited as regards extension into the hypervelocity range of interest (say in excess of 10,000°K or 20,000 ft/sec).

DEVELOPMENT OF HYPERVELOCITY WIND TUNNELS

It is thus apparent that a rather well-defined stage has been reached in the hypersonic wind tunnel technology: the available techniques have been well exploited in terms of Mach and Reynolds numbers, while new techniques have to be developed and present ones pushed well beyond the current technology in order to enter the true hypervelocity regime.

With this realization, work directed toward development of 20,000-ft/sec-plus tunnels started in VKF in 1962. The shock-tube tunnel technique has been chosen, although application of unsteady expansion methods is also being investigated experimentally. The emphasis has been placed on attainment of both hypervelocity and equilibrium flow, the latter requirement necessitating expansion from extremely high reservoir pressures. So far, the results indicate that development of a suitable shock-tube driver may well be the critical factor. Large-scale experimental work with a 4-in.-diam, 5000-atm shock tube will start in VKF early this year.

The approach here mentioned is of course only one of the many on which work is proceeding at AEDC and elsewhere. Since interplanetary flight missions involve velocities completely out of reach of the well-established wind tunnel techniques, it seems evident that radically new methods have to be developed. In particular, such velocities are most unlikely to be obtained by expansion of gas from a state of high pressure and enthalpy; rather, direct acceleration methods may offer promise. Investigation of application of such methods under both high and very low-density conditions are in progress in the VKF.

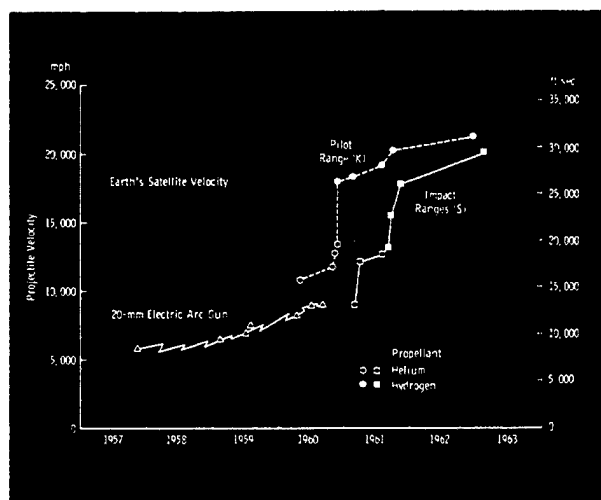


Fig. 2 Development of VKF Hypervelocity Launchers through the Years

HYPERVELOCITY RANGE TECHNIQUE

The aeroballistic range technique - one of the oldest aerodynamic tools - antedates wind tunnels by many years. Provided a suitable launcher can be developed, it offers exact duplication of free-stream conditions, at the expense of data acquisition, a task much more difficult than in wind tunnel testing. In view of the wind tunnel limitations discussed above, preliminary investigations of high-speed launchers were initiated in VKF in 1957, the effort being stepped up in 1960 and leading toward bringing into operation this year a large, 1000-ft-long hypervelocity range facility.

The ballistic technique lends itself also to investigation of hypervelocity impact phenomena, such as may occur in space flight due to collision with man-made or natural objects. The VKF has been engaged, since 1961, in impact studies at velocities up to 30,000 ft/sec.

In Table 2, the VKF aerodynamic and impact range facilities are listed together with the major performance parameters. The course of development of hypervelocity launchers is depicted in Fig. 2. The beneficial effect of the use of hydrogen in lieu of helium as the propellant in the two-stage guns is clearly evident.

It has been indicated that a plateau of wind tunnel development has been reached and that radically new approaches are required to enter the true hypervelocity field.

Although at a different velocity level, the situation seems to be analogous with respect to the launcher development. In Fig. 3 a plot is shown of total launch weight versus velocity. The data have been extracted from publications of all major contributors to this field and are identified by initials of the various organizations. Through the points of maximum velocity at any given weight, a line has been drawn labeled "Record 1962" and substantially represents the maximum claims of the major aeroballistic test facilities. There are two interesting observations to be made concerning Fig. 3. First, it is evident that the maximum velocity is strictly a function of weight and that therefore claims of absolute maximum velocity reached are of little significance. Secondly, an extrapolation of the "record" curve leads to negligible weights at velocities of about 35,000 ft/sec. Since the higher velocities plotted in Fig. 3 were invariably obtained with some type of a light-gas gun, the extrapolation of this curve might, in fact, indicate the limitations of this type of launcher.

Such limitations are also apparent from correlation of theoretical analyses of light-gas launchers with experimentally determined performance.

It would thus appear that, in order to substantially increase the launch velocity, resort must be made to new techniques. Two general approaches are possible: augmentation of performance of light-gas guns

and development of radically different techniques. At present, the former approach has been chosen at the VKF.

The basic problem of imparting substantial acceleration to a projectile already traveling at 30 kft/sec presents a serious challenge. The first step considered necessary before augmentation can be attempted is a detailed investigation of kinematics of the existing, high performance light-gas guns, and work in this direction is proceeding in the VKF.

COUNTERFLOW RANGE TECHNIQUE

From the previous discussion the velocity limitations of wind tunnels and launchers are clearly apparent. Insofar as the aerodynamic testing using the range technique is concerned, a substantial increase in the relative velocity is immediately possible by combining a launcher with a wind tunnel in a counterflow configuration. This technique has been pioneered by the NASA Ames Research Center and it is also being developed in the VKF for future application to the hypervelocity shock tunnel already mentioned. With the VKF pilot counterflow facility, which began operating early this year, relative velocities of 40 kft/sec will be possible with the existing launchers (30 kft/sec), whereas speeds of 50 kft/sec would be eventually reached with the hypervelocity shock tunnel.

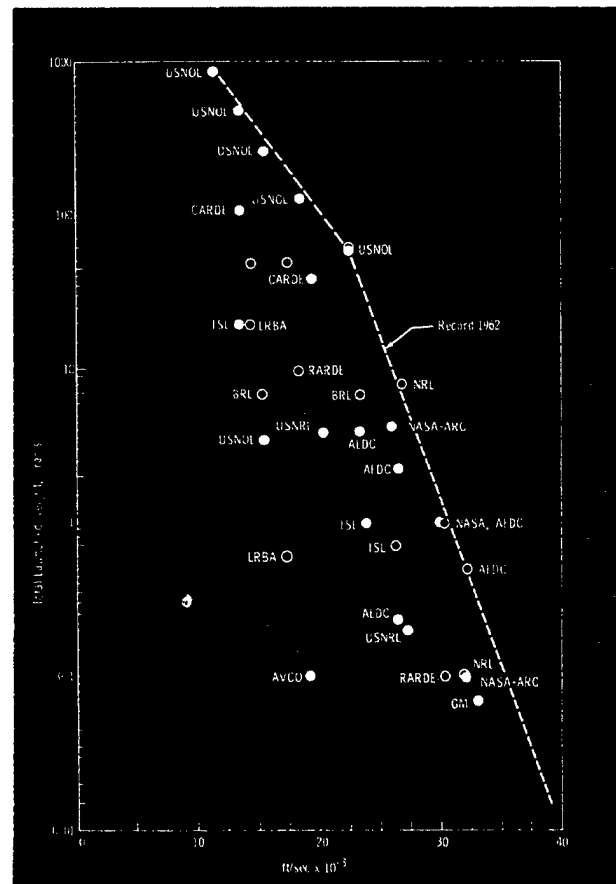


Fig. 3 Maximum Launch Velocities and Weights



Temperature sensitive paint was used to study heat transfer to a lifting configuration at Mach 10.

AERODYNAMICS

ANALYTICAL STUDIES

In order to provide a sound basis for analysis and correlation of experimental results, purely theoretical studies are being conducted in the VKF. They are directed toward the effective use of existing theories and developing new approaches. Both tasks often involve complex calculations and hence require development of special computational procedures. This is also true of the determination of the thermodynamic properties of the working gas media.

THE INVISCID FLOW FIELD OF BLUNT, AXISYMMETRIC BODIES

By

C. H. Lewis

It is well known that at hypersonic conditions there may exist a significant coupling between the viscous and inviscid flow fields known as "viscous interaction" (see page 20). Nevertheless, there are many cases in which this coupling is weak, and one is justified in neglecting its influence. In such cases knowledge of the inviscid flow field is required for determination of the wall boundary-layer edge conditions.

Of primary interest here is the calculation of the flow field about a blunted, axisymmetric body. Specifically, results for the flow of perfect gas ($\gamma = 1.4$) over a 9-deg half-angle, spherically blunted cone and a hemisphere-cylinder at $M_\infty = 18$ will be presented. The calculations are based upon the method of Gravalos (Ref. 1) of the General Electric Company.

In Gravalos' method the flow field over a blunt body is divided into three regions: (1) transonic, (2) supersonic, and (3) subsonic. In most instances, it is only necessary to calculate (1) and (2) since the extent of (3) is small and does not significantly affect the downstream regions. The transonic solution is assumed to be a unique solution for a given set of free-stream conditions and body geometry (usually taken to be a sphere in the transonic region). For a given body shape, a pressure distribution (initially taken to be Newtonian) and a shock shape are assumed. Since it is necessary to iterate for a solution in the transonic region, the more accurate the data are assumed, the faster a solution will be obtained. Experience has shown that when a spherically concentric shock wave and Newtonian pressure distribution are assumed, about eight iterations are necessary for convergence to the final solution.

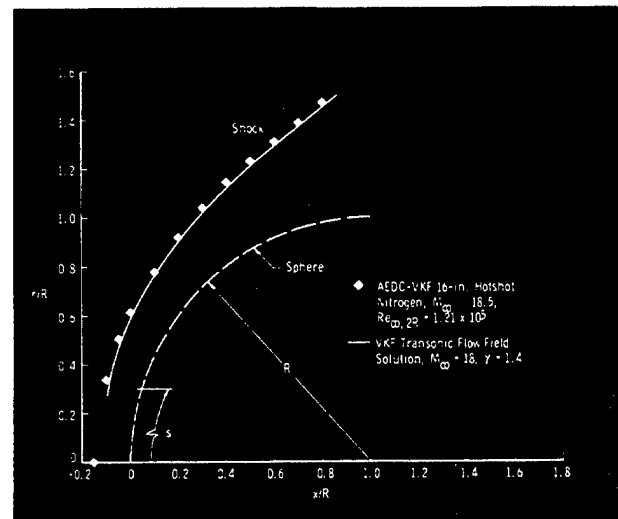


Fig. 1 The Shock Shape over a Sphere

The shock shape determined from a perfect gas ($\gamma = 1.4$) transonic solution at $M_\infty = 18$ is shown in Fig. 1, where experimental data from AEDC-VKF 16-in. Hotshot tunnel are also shown. The agreement between theory and experiment is excellent. The theoretical and experimental pressure distributions on a hemisphere-cylinder are compared in Fig. 2.

The primary purpose of the transonic solution is to provide initial data for the supersonic region. To obtain these initial data a non-characteristic line (usually a normal to the surface) is drawn from the body to the shock wave in the transonic region where the Mach number at the wall is about 1.1. Data are interpolated at 18 points evenly spaced along the initial line. These data are plotted and smoothed such

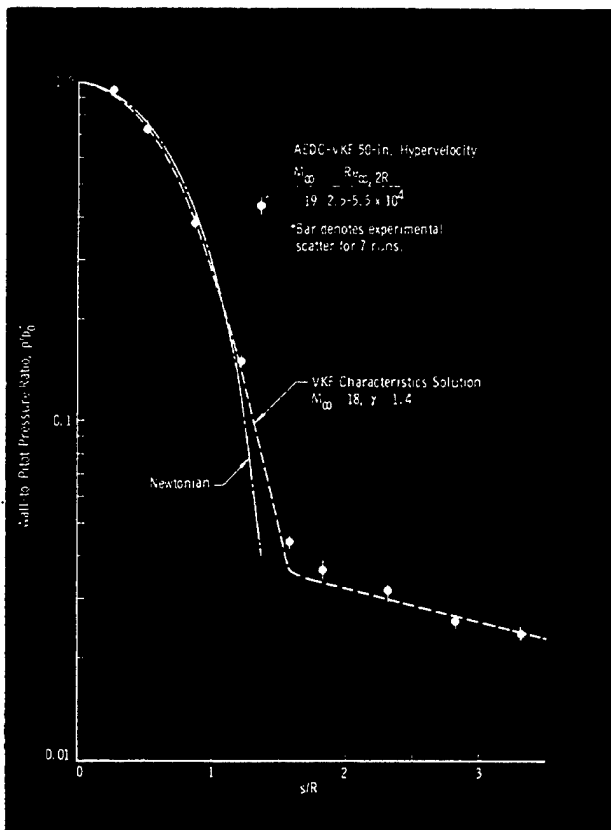


Fig. 2 Pressure Distribution over a Hemisphere Cylinder

that the shock crossing conditions are satisfied at the shock wave.

The initial value problem is now well posed. The characteristic equations are solved subject to the inviscid wall and shock crossing boundary conditions and the given initial data. The flow field solutions are then obtained by iteration along the characteristic directions. The results of such calculations, in terms of pressure distributions, for flow over 9-deg half-angle, spherically blunted cones are shown in Figs. 3 and 4. These calculated data are identical to those previously obtained by FitzGibbon (Ref. 2) for a 0.05 nose bluntness ratio, 9-deg half-angle cone. The difference between theory and experiment must be attributed to viscous rather than to the real gas effects; thus, the agreement between the $M_\infty = 15$ real gas solution (Fig. 3) and experiment should be considered fortuitous. The viscous parameter (see page 20) shown in Fig. 3 is

$$\bar{v}_\infty \equiv M_\infty \sqrt{C_\infty} / \sqrt{Re_{\infty,L}}$$

where $C_\infty = (\mu_w/\mu_\infty)(T_\infty/T_w)$ and $Re_{\infty,L}$ is the free-stream Reynolds number based on model length.

The calculated results for the supersonic flow field over a hemisphere-cylinder are shown in Figs. 5 and 6. Experimental data are also shown from the AEDC-VKF-50-in.

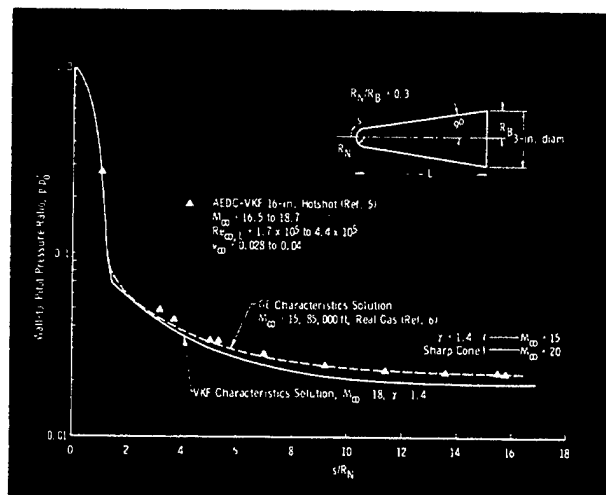


Fig. 3 Pressure Distribution over a 9-deg Sphere-Cone, 0.3 Bluntness Ratio

Hypervelocity (hotshot type) tunnel. The real gas numerical results of Feldman (Ref. 3) for $M_\infty \approx 18$ at 60,000-ft altitude are also shown for comparison. The mean of the experimental pressure data is within ± 10 percent of the perfect gas characteristic solution.

The shock shape of a 9-deg half-angle, spherically blunted cone is shown in Fig. 7. The results of the $\gamma = 1.4$ and real gas characteristic solutions are compared with the experimental results of Lewis (Ref. 5) in the AEDC-VKF-16-in. Hotshot at $M_\infty = 18.9$ and Inouye and Lomax (Ref. 8) in the Ames Free Flight Range at $M_\infty = 17.8$. One should note, however, that the free-flight Reynolds number is two orders of magnitude larger than in the VKF experiment. Hence, the relationship between inviscid, perfect gas theory and the experiments is, as expected, qualitatively correct.

Similar computational methods are available for flow fields of sharp, pointed bodies. Computational methods have been developed for (1) application of the characteristics solution to the flow inside an axisymmetric nozzle, (2) inclusion of

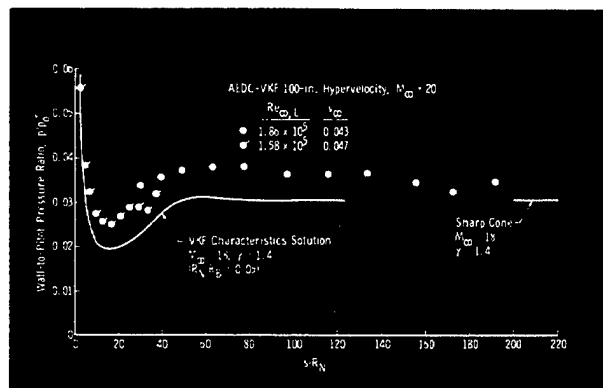


Fig. 4 Pressure Distribution over a 9-deg Sphere-Cone

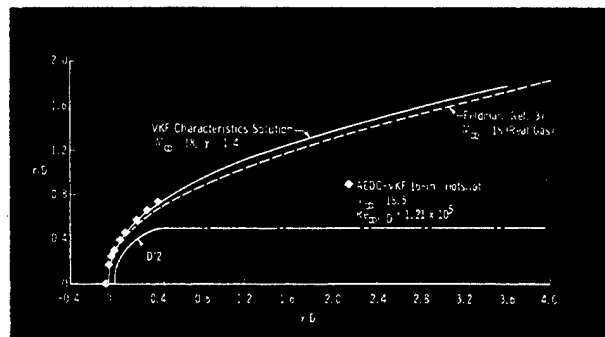


Fig. 5 The Shock Shape over a Hemisphere-Cylinder

Prandtl-Meyer expansions in flow fields, and (3) inclusion of secondary shocks in flow fields (see, e.g., Ref. 4).

REFERENCES

1. Gravalos, F. G., Edelfelt, I. H., and Emmons, H. W. "The Supersonic Flow about a Blunt Body of Revolution for Gases at Chemical Equilibrium." General Electric Company R58SD245, June 1958.
2. FitzGibbon, S. A. "Flow Field Characteristics of Low Drag Bodies of Revolution at Mach 18." General Electric Company Aerodynamics Data Memo No. 1:70, January 1962.
3. Feldman, S. "A Numerical Comparison between Exact and Approximate Theories of Hypersonic Inviscid Flow Past Slender Blunt-Nosed Bodies." AVCO Research Report 71, June 1959; also *ARS Journal*, May 1960, pp. 463-468.
4. Gravalos, F. G., Brong, E., and Edelfelt, I. H. "The Calculation of Flow Fields with Secondary Shocks for Real Gases at Chemical Equilibrium." General Electric Company R59SD419, May 1960.
5. Lewis, C. H. "Pressure Distribution and Shock Shape over Blunted Slender Cones at Mach Numbers from 16 to 19." AEDC-TN-61-81, August 1961.
6. General Electric Company. Private Communication with H. Ridyard.
7. Boisson, J. C. "Experimental Investigation of the Hemisphere-Cylinder at Hypervelocities in Air." AEDC-TR-58-20, November 1958.
8. Inouye, M. and Lomax, H. "Comparison of Experimental and Numerical Results for the Flow of a Perfect Gas about Blunt-Nosed Bodies." NASA TN D-1426, September 1962.

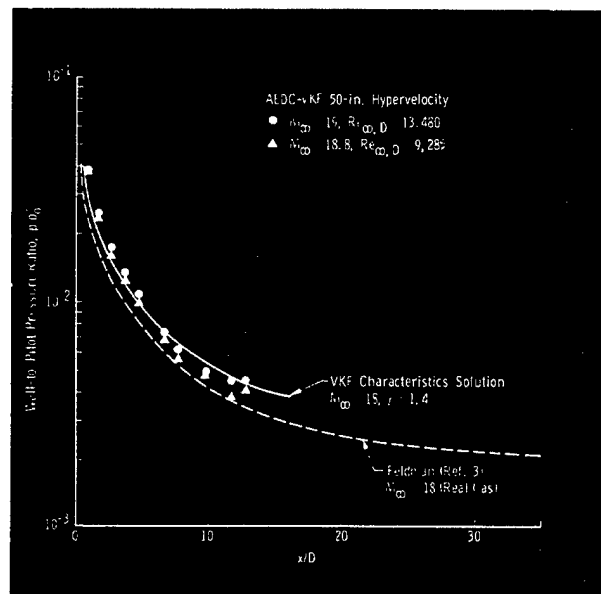


Fig. 6 Pressure Distribution over a Hemisphere-Cylinder

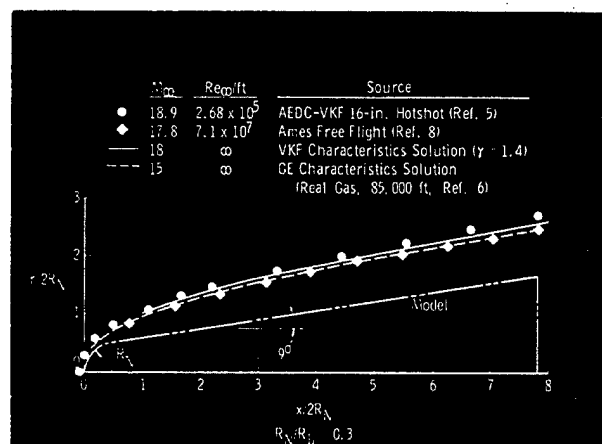


Fig. 7 Shock Shape over a Spherically Blunted Cone

THE BLAST-HYPERSONIC FLOW ANALOGY

By

J. Lukasiewicz and C. H. Lewis

It was Hayes (Ref. 1) who pointed out that the hypersonic, small disturbance theory is given by the unsteady solution in one less space coordinate, so that flow in the plane normal to the direction of motion can be treated independent of x . The hypersonic, small disturbance theory (Ref. 2) is applicable to slender bodies such that the body thickness parameter $\tau \ll 1$ and at large Mach numbers such that $M_\infty \tau \geq 1$. Thus, the small disturbance theory will not apply in the nose region where $\tau \ll 1$ is violated. Also, it will not apply far downstream where $M_\infty \tau \geq 1$ does not hold.

The original Taylor's (Ref. 3) solution (first approximation) of a spherical blast wave was extended by Lin (Ref. 4) to the case of a cylindrical blast wave where he also obtained the steady-flow, axisymmetric solution analogous to the cylindrical shock. Sakurai (Refs. 5 and 6) published first and second approximation solutions for plane, cylindrical, and spherical blasts. Cheng and Pallone (Ref. 7) applied the plane wave, first approximation solution to the case of steady flow past a blunt plate. Lees and Kubota (Ref. 8) applied Sakurai's results to obtain a simplified second approximation, axisymmetric solution in the specific case of a hemisphere-cylinder at $M_\infty = 7.7$, $\gamma = 1.4$.

Thus, several years ago it became apparent that, although several specific cases had been treated, a consistent set of blast analogy solutions was not available. These solutions were derived by Lukasiewicz (Ref. 9), who applied Sakurai's

first and second approximation solutions to two-dimensional and axisymmetric flow problems. He derived expressions for the shock shape and pressure distribution over blunt-nosed flat plates and cylinders, and also presented (Ref. 9a) the variation of pressure and density in the flow field over a cylinder. Comparisons of experimental results (for ideal air conditions, $\gamma = 1.4$) and theoretical, characteristics calculations for ideal and real air indicated that excellent agreement with the blast analogy solutions was obtained over a wide range of Mach numbers and drag coefficients, provided a simple shift of the origin of the body coordinates was made (streamwise coordinate for the pressure distribution and radial coordinate for the shock shape). Typical examples of such correlations for axisymmetric flow are

First Approximation

$$p/p_m = 0.067 M_m^2 C_D^{1/2} / (x/d) \quad (1)$$

$$R/d = 0.795 C_p^{1/4} (x/d)^{1/2} \quad (2)$$

Second Approximation

$$p/p_m = 0.067 M_{\infty}^2 C_D^{1/2} / (x/d) + 0.44 \quad (3)$$

$$\begin{aligned} (R/d)/(M_{\infty}^2 C_D^{1/2}) &= 0.795[(x/d)/(M_{\infty}^2 C_D^{1/2})]^{1/2} \\ &\quad [1 + 3.15(x/d)/(M_{\infty}^2 C_D^{1/2})]^{1/2} \end{aligned} \quad (4)$$

These results are shown in Figs. 1 and 2.

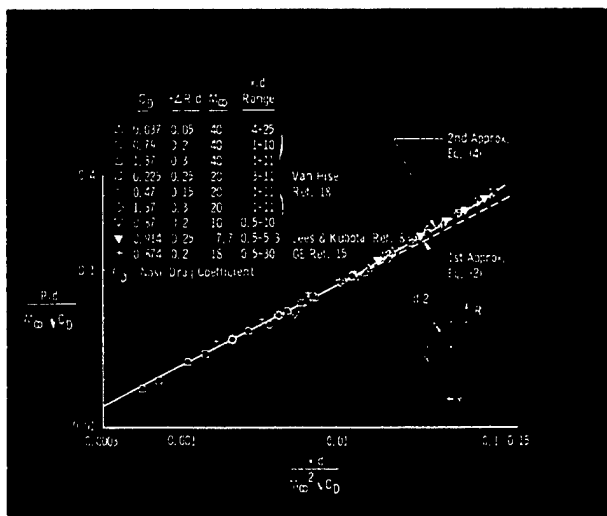


Fig. 1 Correlation of Theoretical (Method of Characteristics) and Experimental Shock Shapes in Axisymmetric Flow of Ideal Air ($\gamma = 1.4$)

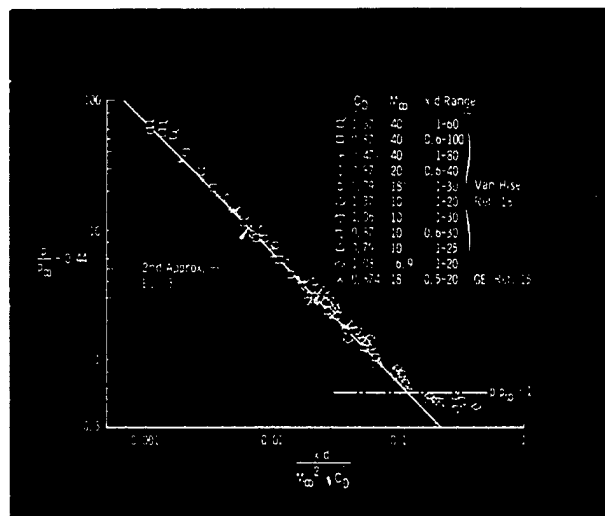


Fig. 2 Correlation of Theoretical Pressures in Axisymmetric Flow ($\gamma = 1.4$, $\Delta x/d = 1$)

A new approach to the unsteady blast problem was developed by Ōshima (Ref. 10), who assumed the flow within a cylindrical blast shock to be similar near the shock wave. Lewis (Ref. 11) extended Ōshima's solutions to include spherical and plane blasts, and he also obtained improved accuracy in the numerical solutions for the cylindrical blasts. In application to un-

steady, hypersonic flow, Lewis (Ref. 12) used Ōshima's quasi-similarity model to compute the shock shape and pressure distribution in two-dimensional and axisymmetric flow. The results are shown in Figs. 3 through 6, where theoretical (characteristics solutions), experimental, and Lukasiewicz's blast analogy results are also shown.

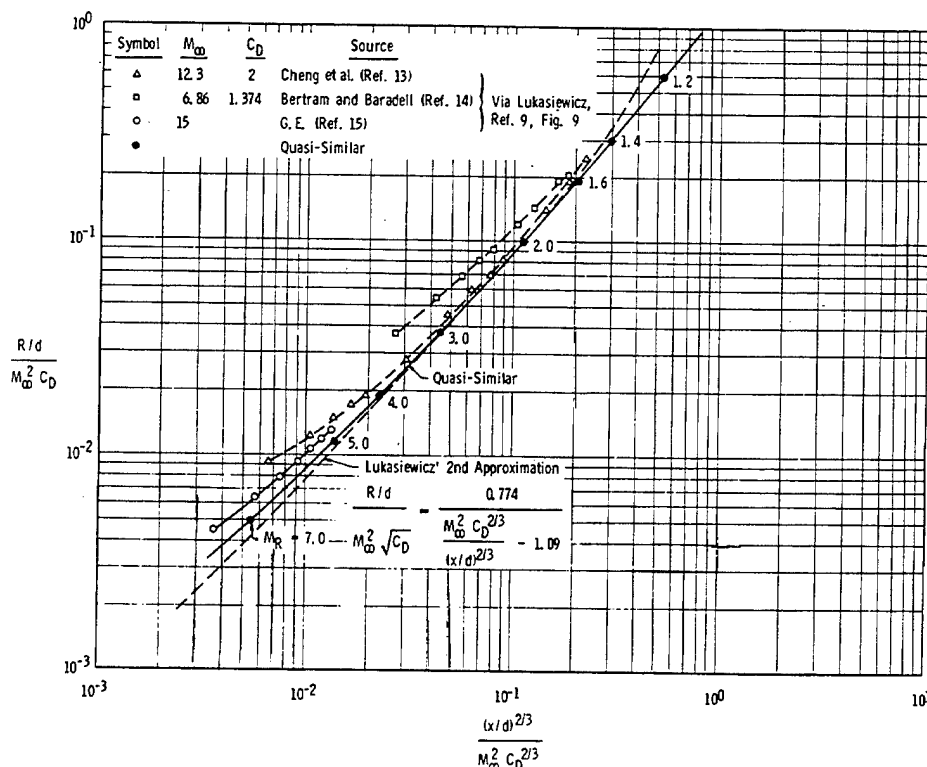
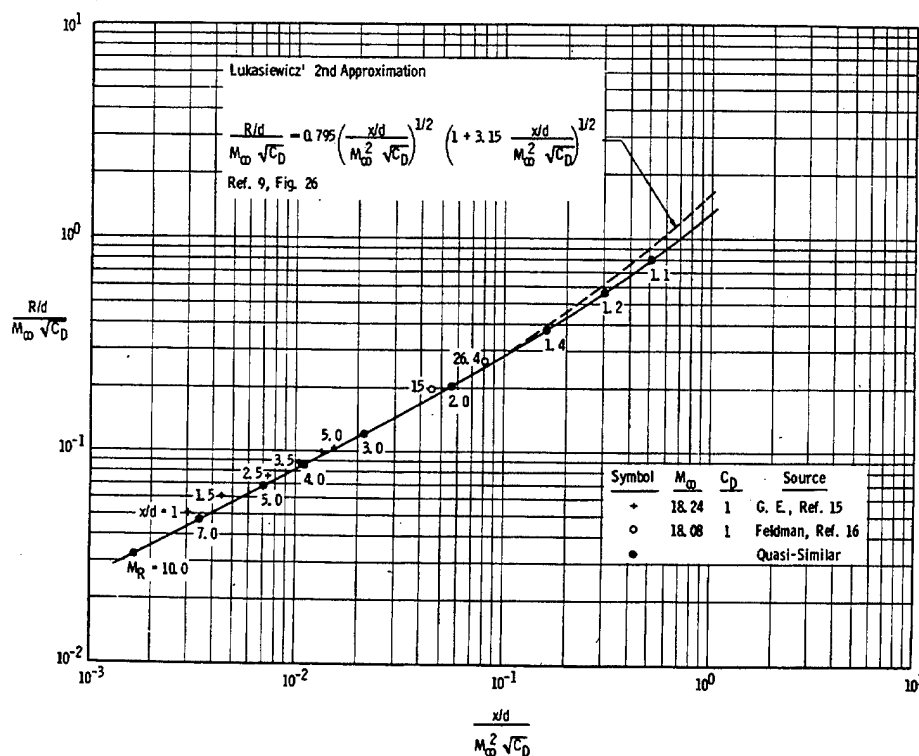


Fig. 3 Shock Shapes for Plane Flow in Air ($\gamma = 1.4$)

Fig. 4 Shock Shapes for Axisymmetric Flow in Air ($\gamma = 1.4$)



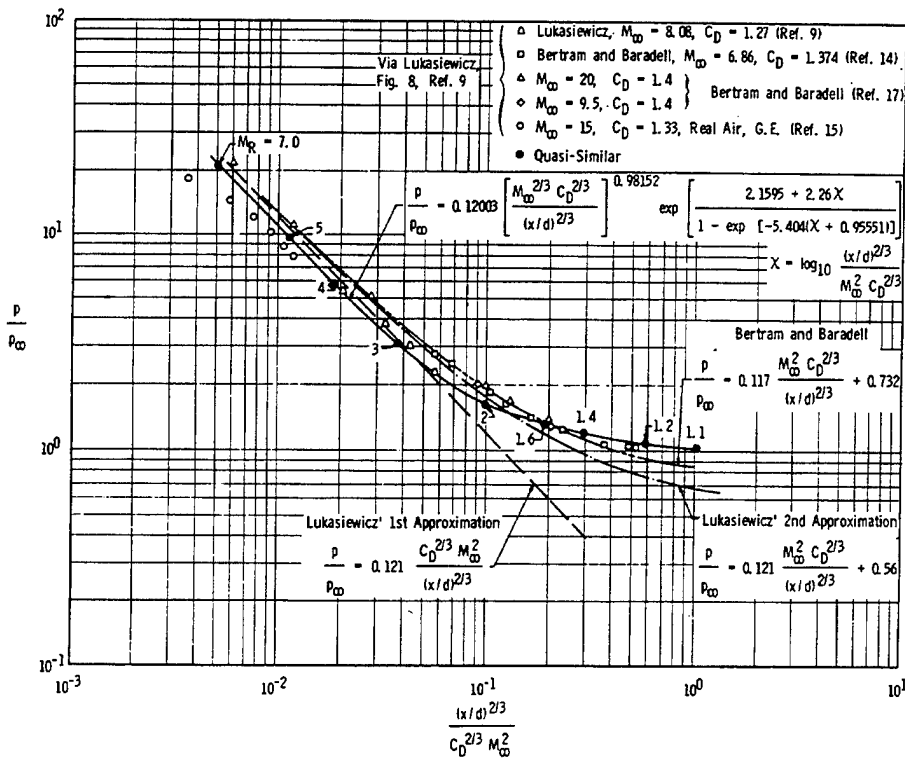
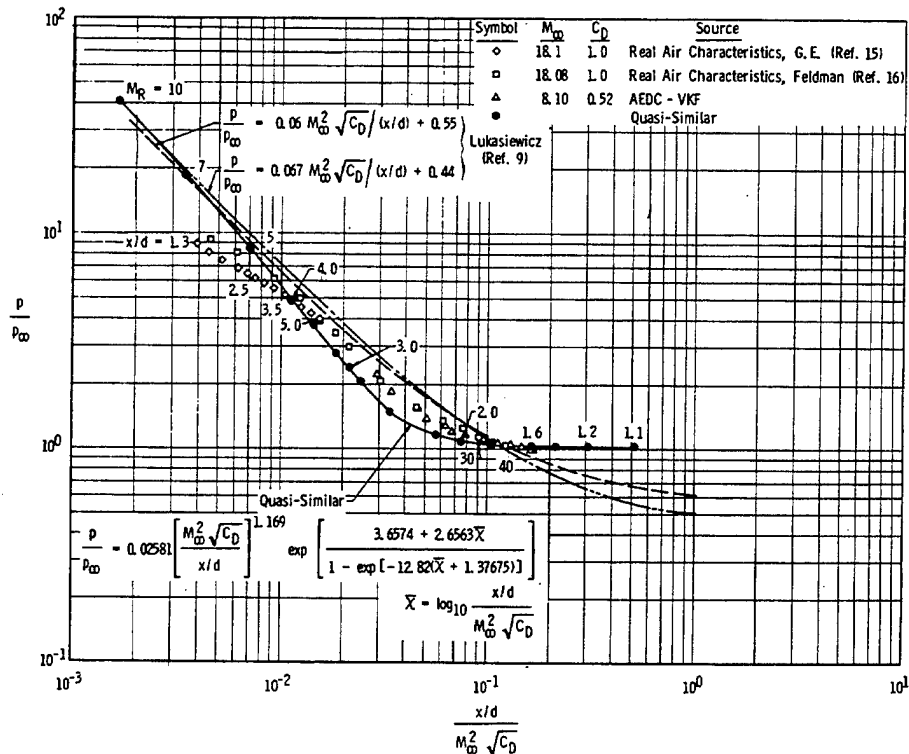


Fig. 5 Pressure Distributions for Plane Flow in Air ($\gamma = 1.4$)

Fig. 6 Pressure Distributions for Axisymmetric Flow in Air ($\gamma = 1.4$)



REFERENCES

- Hayes, W. D. "On Hypersonic Similitude." Quart. Appl. Math., Vol. 5, April 1947, pp. 105-106.
- van Dyke, M. "Applications of Hypersonic Small Disturbance Theory." Journal of the Aeronautical Sciences, Vol. 21, 1954, pp. 179-186.

3. Taylor, G. I. "The Formation of a Blast Wave by a Very Intense Explosion." Proc. Royal Soc. (London), Vol. 201, March 22, 1960, pp. 159-186.
4. Lin, S. C. "Cylindrical Shock Waves Produced by Instantaneous Energy Release." Journal of Applied Physics, Vol. 25, 1954, pp. 54-57.
5. Sakurai, A. "On the Propagation and Structure of the Blast Wave, I." Journal of the Phys. Soc. of Japan, Vol. 8, Sept.-Oct. 1953, p. 662.
6. Sakurai, A. "On the Propagation and Structure of the Blast Wave, II." Journal of the Phys. Soc. of Japan, Vol. 9, March-April 1954, p. 256.
7. Cheng, H. K. and Pallone, A. J. "Inviscid Leading-Edge Effect in Hypersonic Flow." Journal of the Aeronautical Sciences, Vol. 23, July 1956, pp. 700-702.
8. Lees, L. and Kubota, T. "Inviscid Hypersonic Flow over Blunt-Nosed Slender Bodies." Journal of the Aeronautical Sciences, Vol. 24, March 1957, pp. 195-202.
9. Lukasiewicz, J. "Hypersonic Flow-Blast Analogy." (a) AEDC-TR-61-4, June 1961; (b) ARS Preprint 2169-61, October 1961; (c) ARS Journal, Vol. 32, September 1962, pp. 1341-1346.
10. Ōshima, K. "Blast Waves Produced by Exploding Wire." Aero. Research Institute, University of Tokyo, Report No. 358, July 1960, pp. 137-193.
11. Lewis, C. H. "Plane, Cylindrical, and Spherical Blast Waves Based upon Ōshima's Quasi-Similarity Model." AEDC-TN-61-157, December 1961.
12. Lewis, C. H. "The Blast-Hypersonic Flow Analogy Based Upon Ōshima's Quasi-Similarity Model." AEDC-TN-61-158, December 1961.
13. Cheng, H. K., et. al. "Boundary-Layer Displacement and Leading-Edge Bluntness Effects in High-Temperature Hypersonic Flow." Institute of the Aerospace Sciences Paper No. 60-38, January 1960; also Journal of the Aero/Space Sciences, Vol. 28, May 1961, pp. 353-381.
14. Bertram, M. and Baradell, D. L. "A Note on the Sonic-Wedge Leading-Edge Approximation in Hypersonic Flow." Journal of the Aero/Space Sciences, Vol. 24, August 1957, pp. 627-629.
15. General Electric Company. Private communications with H. Ridyard.
16. Feldman, S. "A Numerical Comparison between Exact and Approximate Theories of Hypersonic Inviscid Flow Past Slender Blunt-Nosed Bodies." AVCO Research Report 71, June 1959; also ARS Journal, Vol. 30, May 1960, pp. 463-468.
17. Baradell, D. L. and Bertram, M. H. "The Blunt Plate in Hypersonic Flow." NASA TN D-408, October 1960.
18. vanHise, V. "Analytic Study of Induced Pressure on Long Bodies of Revolution with Varying Nose Bluntness at Hypersonic Speeds." NASA TR R-78, 1960.

SKIN FRICTION AND HEAT TRANSFER FOR LAMINAR BOUNDARY-LAYER FLOWS

By

C. H. Lewis

SKIN FRICTION AND BOUNDARY-LAYER CHARACTERISTICS

The calculation of boundary-layer characteristics (e.g., boundary-layer thickness, δ , momentum thickness, θ , displacement thickness, δ^* , and wall shear stress, τ_w) is of great interest in fluid mechanics. Of particular interest in experimental wind tunnel studies is the calculation of the skin friction contribution to the total drag. At high Mach numbers ($M_\infty \sim 20$) and moderate Reynolds numbers based on free-stream conditions and model length ($Re_{\infty, L} \sim 33,000$), Whitfield and Griffith (Ref. 1) have shown that the total drag of a 9-deg, spherically blunted cone is approximately twice the inviscid pressure drag.

Two examples will be discussed which indicate studies made in VKF. Each example is chosen to display different phenomena. In one case there were large separated regions, and the theory was in doubt. In the other case, with the inclusion of the second-order effects, the calculated results agree well with the experimental ones.

A CONE-CYLINDER-FLARE MODEL AT $M_\infty = 1.48$

A modification of Cohen and Reshotko's integral method (Ref. 2) is currently used in the VKF for computing skin friction and boundary-layer characteristics over blunt and sharp axisymmetric and two-dimensional bodies at zero angle of attack. In order

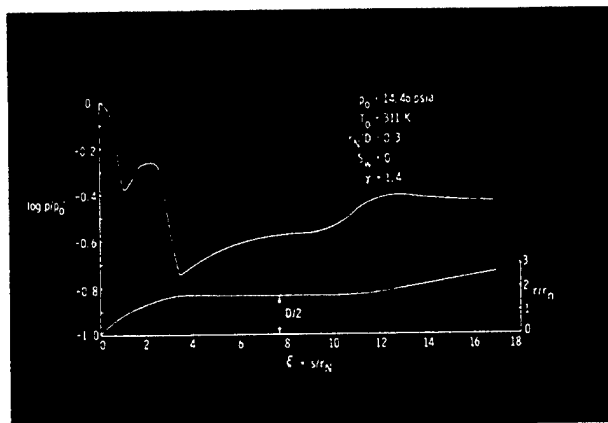


Fig. 1 Body Geometry and Pressure Distribution over HB-2 at $M_\infty = 1.48$

to present the method, a recent calculation will be discussed which displays a modification of the basic integral method of Ref. 2 and provides results for comparison with experiment.

The example chosen is the hypersonic test body HB-2 at $M_\infty = 1.48$. The body geometry and pressure distribution are shown in Fig. 1. The pressure distribution shown in that figure is the result of a single empirical equation for the experimental data. The method of empirically fitting data was devised by Grabau (Ref. 3) for fitting thermodynamic data. The empirical pressure distribution formula is within a percent or so of the faired experimental data.

A typical result of the boundary-layer characteristics is shown in Fig. 2, where the momentum thickness distribution $\theta(\xi)$ is shown. The regions where $\theta = 0$ result from a predicted separation of the laminar boundary layer. Because of the three distinctly separated regions, a modification to the integral method proposed by Cohen and Reshotko (Ref. 2) was found necessary. This modified procedure, for the case presented here at least, is more accurate than

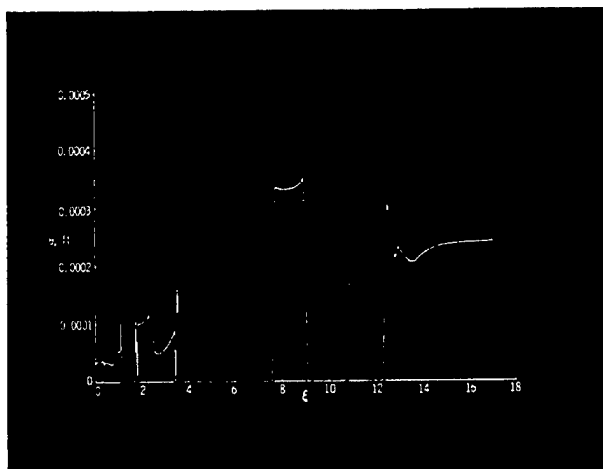


Fig. 2 $\theta(\xi)$ for HB-2 at $M_\infty = 1.48$

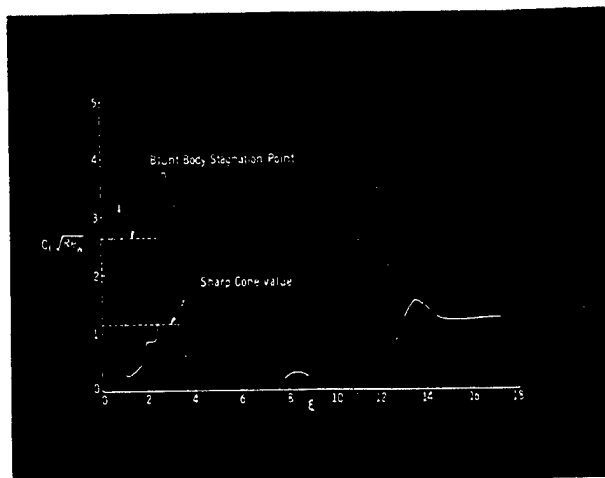


Fig. 3 Skin Friction Parameter for HB-2 at $M_\infty = 1.48$

the one given in Ref. 2. Basically the Falkner-Skan pressure gradient parameter m was computed from the transformed velocity distribution, $m = d \log U_e / d \log X$ (for details see Refs. 2 and 4). The formula $\beta = 2m/(m+1)$ was used to obtain β . From the similar solutions, a relation $n(\beta; S_w)$ was obtained. The remaining calculations followed the integral method of Ref. 2. This modification works well where the favorable pressure gradient is not too large and has the added feature that the solution is independent of the assumptions required to obtain the correlation parameter in the basic integral method. The modified procedure is also more stable where the boundary layer reattaches downstream of a separated region. Of course, the solution is no better than the theoretical model for which the similar solutions were obtained. It should also be stated that the effects of secondary shocks caused by the separated boundary layer and/or flare were neglected.

The skin friction parameter is

$$C_f \sqrt{Re_w} = \frac{2\tau_w}{\rho_w u_e^2} \sqrt{\frac{\rho_w u_e s}{\mu_w}}$$

where w denotes conditions at the wall (here assumed to be the adiabatic wall conditions), and e denotes conditions at the "edge" of the boundary layer. This parameter is shown in Fig. 3. In this example, the calculated friction drag coefficient, CD_f , was only about one percent of the total drag coefficient. However, as noted above, there were large separated regions, and the effects of secondary shocks were neglected. More research is needed to resolve these problems.

A SPHERICALLY BLUNTED CONE AT $M_\infty \approx 19$

In this case, the boundary layer was calculated for a 0.3 bluntness ratio, 9-deg half-angle, spherically blunted cone (see Fig. 4). This particular model has been

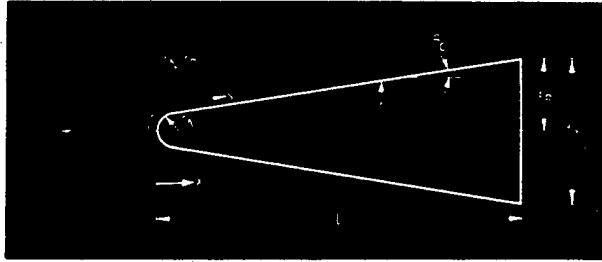


Fig. 4 Cone Nomenclature

studied extensively, both experimentally and analytically, in the VKF (see page 6). A free-stream Mach number of approximately 19 is representative of the conditions in the AEDC-VKF Hotshot tunnels (see, e.g., Refs. 1 and 5 and page 2).

The integral method of Cohen and Reshotko (Ref. 2) was used to compute the boundary-layer characteristics and skin friction. The calculation was based on equilibrium, dissociating nitrogen properties (Ref. 6), and the experimental pressure distribution obtained by the author (Ref. 7), shown on page 6. The computed friction drag based on Ref. 2 is shown in Fig. 5, denoted here as "similar friction drag". A similar figure was presented by Whitfield and Griffith in Ref. 1, where the transverse curvature and displacement-induced drag components were discussed. The viscous parameter \bar{v}_∞ shown in Fig. 5 is the axisymmetric viscous interaction parameter,

$$\bar{v}_\infty = \frac{M_\infty \sqrt{C_{\infty}}}{\sqrt{Re_{\infty, L}}}$$

where C_∞ is defined by $\mu_w/\mu_\infty = C_\infty(T_w/T_\infty)$.

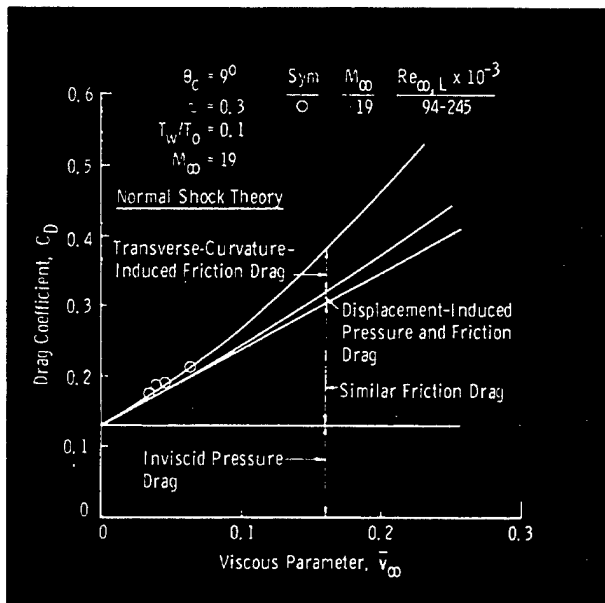


Fig. 5 A Comparison of Theoretical and Experimental Drag Coefficient for 9-deg Half-Vertex Angle Blunt Cone

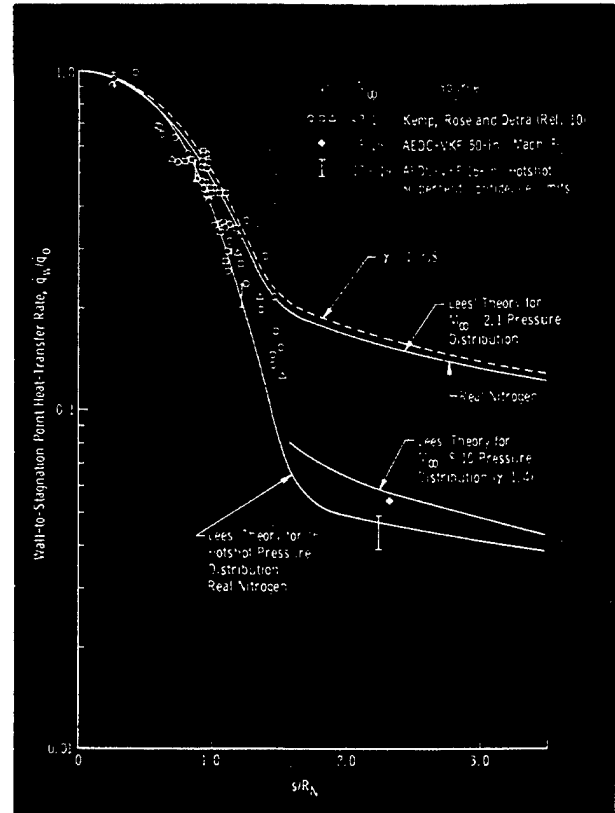


Fig. 6 Heat-Transfer Distribution over a Hemisphere-Cylinder

It should be noted from Fig. 5 that the similar friction drag component is linear with \bar{v}_∞ . Also, for the range of experimental conditions shown, the contribution of the second-order boundary-layer effects (displacement and transverse curvature) is small; however, the similar friction drag is about 40 percent of the inviscid pressure drag.

Unlike the first example, if one neglects second-order effects for a $\bar{v}_\infty < 0.1$, the combined pressure and friction drag is in reasonable agreement with experiment.

HEAT-TRANSFER DISTRIBUTION

An example of the straightforward application of Lees' theory (Ref. 8) to compute the heat-transfer distribution over a hemisphere cylinder in real nitrogen at $M_\infty \approx 18.5$ is shown in Fig. 6. These data were presented by Griffith and Lewis in Ref. 9, where a study was made of heat transfer to spherically blunted cones and hemisphere-cylinders at hypersonic conditions.

REFERENCES

1. Whitfield, J. D. and Griffith, B. J. "Viscous Effects on Zero-Lift Drag of Slender Blunt Cones." AEDC-TDR-63-35, March 1963.
2. Cohen, C. B. and Reshotko, E. "The Compressible Laminar Boundary Layer with

- Heat Transfer and Arbitrary Pressure Gradient." NACA Report 1294, 1956.
3. Grabau, M. "A Method of Forming Continuous Empirical Equations for the Thermodynamic Properties of Air from Ambient Temperatures to 15,000°K, with Applications." AEDC-TN-59-102, August 1959.
 4. Cohen, C. B. and Reshotko, E. "Similar Solutions for the Compressible Laminar Boundary Layer with Heat Transfer and Pressure Gradient." NACA Report 1293, 1956.
 5. Lukasiewicz, J., Jackson, R., and Whitfield, J. D. "Status of Development of Hotshot Tunnels at the AEDC." Paper presented at the AGARD Meeting at TCEA, Rhode-Saint-Genese, Belgium, April 1962.
 6. National Bureau of Standards. Private communication with Mr. J. Hilsenrath, May 1959.
 7. Lewis, C. H. "Pressure Distribution and Shock Shape over Blunted Slender Cones at Mach Numbers from 16 to 19." AEDC-TN-61-81, August 1961.
 8. Lees, L. "Laminar Heat Transfer over Blunt-Nosed Bodies at Hypersonic Flight Speeds." Jet Propulsion, Vol. 26, April 1956, p. 259.
 9. Griffith, B. J. and Lewis, C. H. "A Study of Laminar Heat Transfer to Spherically Blunted Cones and Hemisphere-Cylinders at Hypersonic Conditions." AEDC-TDR-63-102, May 1963.
 10. Kemp, N. H., Rose, P. H., and Detra, R. W. "Laminar Heat Transfer around Blunt Bodies in Dissociated Air." Journal of the Aero/Space Sciences, Vol. 26, 1959, pp. 421-430.

THERMODYNAMIC PROPERTIES OF HIGH TEMPERATURE AIR AND NITROGEN AND THEIR APPLICATIONS

By

C. H. Lewis and Martin Grabau

THERMODYNAMIC DATA

In numerical calculations performed on high-speed digital computing machines, one is faced with the problem of providing auxiliary data (e.g., thermodynamic data, transport properties, etc.). Because of the limited storage and time required by the computer in table-look-up routines, it is usually more economical to use empirical equations. However, generalized machine programs for determining these empirical expressions are not currently available.

Grabau (Ref. 1) set forth a method of forming empirical equations for large numbers of related data with two independent variables and then applied it to the thermodynamic properties of argon-free air (Ref. 2) up to 15,000°K. In particular, he dealt with the dimensionless parameters H_p/p , S/R , and $1/Z$ as functions of p and p . A given parameter is plotted with respect to $\log p$ at constant density. This curve is normally a succession of straight lines joined by transition functions which are asymptotic at both ends. However, the method is not limited to the use of straight lines.

As an example, Fig. 1a shows two straight lines, $f_1(x)$ and $f_2(x)$, which are joined by a curve having a point of inflection at x_0 . The transition from one line to the other is made by means of the Fermi-Dirac function, and the whole equation is in the form

$$y = f_1(x) + \frac{f_2(x) - f_1(x)}{1 + \exp [k(x - x_0)]}$$

in which k is a constant which depends on the rapidity with which the curve moves from one line to the other.

On the other hand, as is shown in Fig. 1b, if the transition from one line to the other does not involve a point of inflection, the transition is made by means of the Bose-Einstein function, and the corresponding equation is in the form

$$y = f_1(x) - \frac{f_2(x) - f_1(x)}{1 - \exp [k(x - x_0)]}$$

in which x_0 is the point at which $f_1(x)$ and $f_2(x)$ would intersect.

The constants in $f_1(x)$ and $f_2(x)$, as well as x_0 and k , are then plotted as functions of the second independent variable, and the curves are converted to empirical equations either by simple polynomials or by means of the transition-function technique described above. This general method of forming empirical equations has been applied in a number of data-reduction programs, e.g., Ref. 3. The choice of p and ρ as independent variables is convenient for some applications (e.g., normal shock calculations), but for other applications different independent variables are more suitable. For isentropic expansions, such as the inviscid flow in a nozzle and expansions around a body (e.g., the inviscid flow field and "edge" conditions for boundary-layer calculations), the choice of the entropy S is most convenient. Also, especially in boundary-layer calculations where the inviscid flow field is assumed to

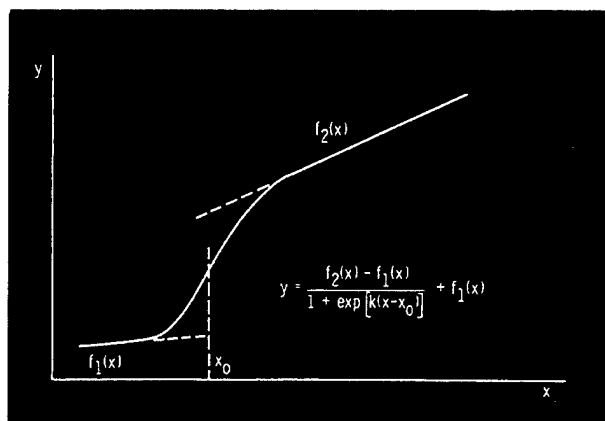


Fig. 1a A Fermi-Dirac Type Transition with a Point of Inflection

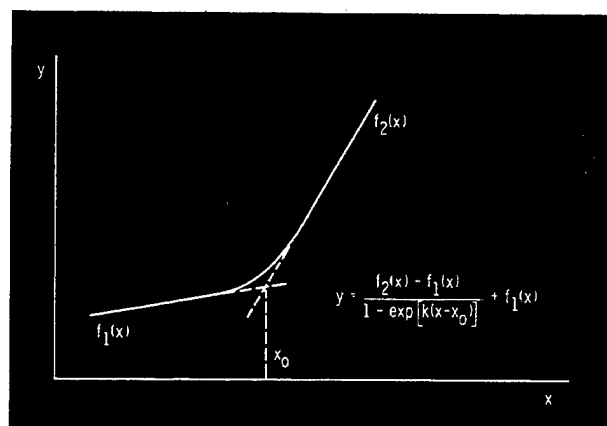


Fig. 1b A Bose-Einstein Type Transition without Inflection

be known, the other natural choice of independent thermodynamic variable is the pressure.

The data of Hilsenrath, Klein, and Woolley (Ref. 4) for equilibrium dissociating and ionizing air have been fitted with empirical surfaces* by Lewis and Burgess (Ref. 5). The enthalpy, $H(p, S)$, compressibility factor, $Z(p, S)$, density, $\rho(p, S)$, and speed of sound, $a(z, S)$ were fitted and are shown in Figs. 2 through 5, where the symbols denote the errors in the empirical surface fits when the data were compared with the interpolated data (at $\log(S/R) = \text{constant}$). The interpolation introduced negligible error when compared with the original data of Ref. 4. The data for nitrogen (Ref. 6) were similarly fitted by Lewis and Burgess; however, those results are not shown here. In general, the errors in the nitrogen surface fits are slightly larger than those for air.

*The method of fitting surfaces to data was developed by Messrs. C. H. Link and E. G. Burgess, Scientific Computing Services, ARO, Inc.

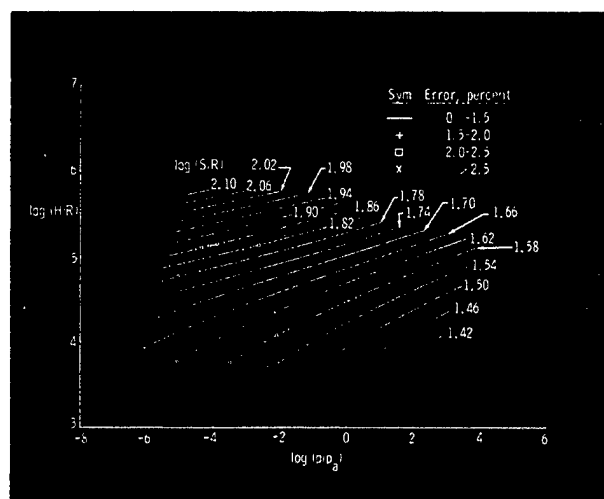


Fig. 2 Enthalpy of Air

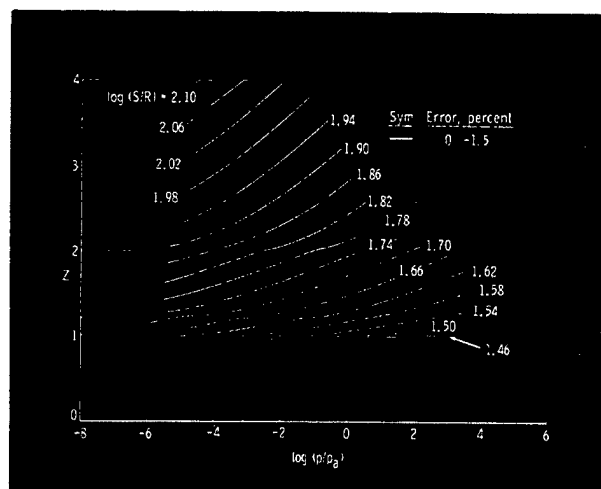


Fig. 3 Compressibility Factor for Air

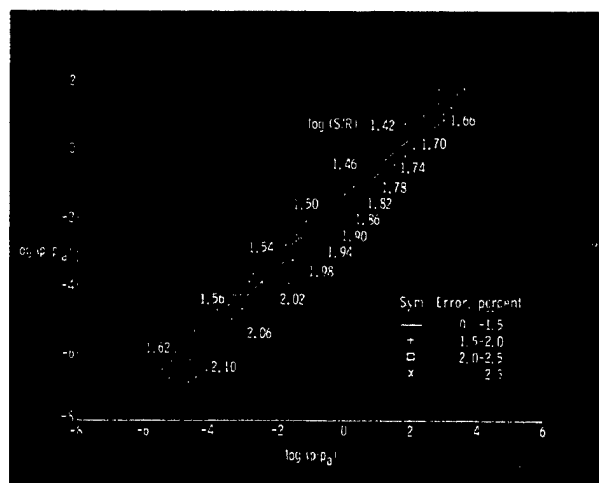


Fig. 4 Density of Air

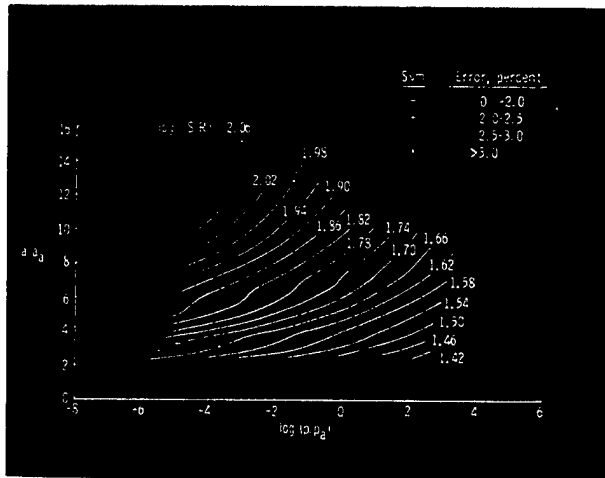


Fig. 5 The Dimensionless Speed of Sound Ratio in Air Where $a_a = 1086.98$ ft/sec at One Atmosphere Pressure and 273.15°K

AN APPLICATION: SPHERE STAGNATION POINT HEAT TRANSFER

The heat-transfer rate to the stagnation point of a sphere in equilibrium air (Ref. 4) has been computed with Fay-Riddell theory (Ref. 7) by Lewis and Burgess (Ref. 8) as follows:

$$\dot{q} \sqrt{r_n} = K \left(\frac{\rho_w}{\rho_a} \mu_w \right)^{0.1} \left(\frac{\rho_o}{\rho_a} \mu_o \right)^{0.4} (H_o - H_w) \left(\frac{p_o/p_a}{\rho_o/\rho_a} \right)^{0.25}$$

where

\dot{q} = heat-transfer rate in Btu/ft²-sec

r_n = nose radius in in.

$K = 7.55274 \times 10^{-3}$

ρ/ρ_a = density in amagats

p/p_a = pressure in atm

H = enthalpy in ft²/sec²

μ = coefficient of viscosity

w denotes conditions at the wall (here assumed $T_w = 300^\circ\text{K}$), o denotes stagnation conditions behind a normal shock, and the conditions at one atmosphere pressure and 273.15°K are a . The viscosity coefficient at high temperature was obtained from Hansen's data (Ref. 9). In the present example, the Lewis number was taken to be unity. The results of this calculation are shown in Fig. 6. For correlation, Z at 0.1 atm is also shown in the figure. The variation in heat-transfer rate is easily correlated with the effects of oxygen dissociation ($Z \lesssim 1.21$), dissociation of nitrogen ($1.21 \lesssim Z \lesssim 2$), and the first ionization of atomic oxygen and nitrogen ($2 < Z < 4$).

It is worth noting that the maximum errors in the thermodynamic surface fits for the range of conditions in this example ($0.1 \leq p_o/p_a \leq 10$, $2000 \lesssim T_o \lesssim 15,000^\circ\text{K}$) were

	T	ρ/ρ_a	H/R	Z
Error (percent)	2.24	2.42	1.96	0.751

Some of these results were published in Ref. 10 where a comparison of the Fay and Riddell theory using these data with the more recent theory of Fay and Kemp (Ref. 11) was given.

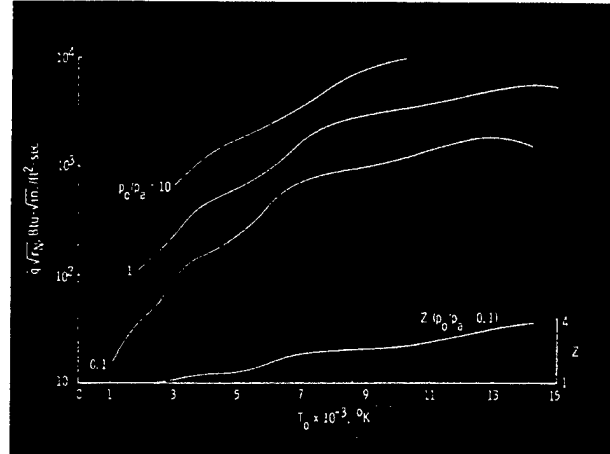


Fig. 6 Stagnation Heat-Transfer Rate in Air ($Le = 1$), $T_w = 300^\circ\text{K}$

REFERENCES

- Grabau, M. "A Method of Forming Continuous Empirical Equations for the Thermodynamic Properties of Air from Ambient Temperatures to $15,000^\circ\text{K}$, with Applications." AEDC-TN-59-102, August 1959.
- Hilsenrath, J. and Beckett, C. W. "Tables of Thermodynamic Properties of Argon-Free Air to $15,000^\circ\text{K}$." AEDC-TN-56-12, September 1956.
- Grabau, M., Humphrey, R. L., and Little, W. J. "Determination of Test-Section, After-Shock, and Stagnation Conditions in Hotshot Tunnels Using Real Nitrogen at Temperatures from 3000 - 4000°K ." AEDC-TN-61-82, July 1961.
- Hilsenrath, J., Klein, M., and Woolley, H. W. "Tables of Thermodynamic Properties of Air Including Dissociation and Ionization from 1500°K to $15,000^\circ\text{K}$." AEDC-TN-59-20, December 1959.
- Lewis, C. H. and Burgess, E. G. "Empirical Equations for the Thermodynamic Properties of Air and Nitrogen to $15,000^\circ\text{K}$." AEDC-TDR-63-138, July 1963.
- National Bureau of Standards. Private Communication with J. Hilsenrath, May 1959.

7. Fay, J. and Riddell, F. R. "Theory of Stagnation Point Heat Transfer in Dissociated Air." *Journal of the Aero/Space Sciences*, Vol. 25, February 1958, pp. 73-85.
8. Lewis, C. H. and Burgess, E. G. "Charts of Sphere Stagnation Heat-Transfer Rate in Air and Nitrogen at High Temperatures." AEDC-TDR-63-139, July 1963.
9. Hansen, C. F. and Heims, S. P. "A Review of the Thermodynamic, Transport, and Chemical Reaction Rate Properties of High-Temperature Air." NACA TN 4359, July 1958.
10. Lewis, Clark H. and Burgess, E. G. "Thermodynamic Properties of Air and Nitrogen to 15,000°K with Application." *AIAA Journal*, Vol. 1, August 1963, pp. 1928-1929.
11. Fay, J. and Kemp, N. "Theory of Stagnation Point Heat Transfer in a Partially Ionized Diatomic Gas." *Inst. Aerospace Science Paper* 63-60, 1963.

SUPERSONIC AND HYPERSONIC FLOWS: VISCOUS INTERACTION AND LOW DENSITY

The VKF wind tunnels, in view of their wide Mach-Reynolds number range, are particularly well suited to experimental investigations of hypersonic viscous interaction. In terms of the hypersonic viscous parameter $M_\infty \sqrt{C_\infty} / \sqrt{Re_{\infty, L}}$ (on which the viscous drag depends), the range covered in the experiments here mentioned was from 0.02 to 0.4 and drag levels as high as 13 times the inviscid drag were measured on slender cones. Simple flow models were developed to predict analytically viscous interaction effects. Generalized correlations of cone stability were also obtained and were found, to the first order, independent of the viscous effects.

At the lowest Reynolds numbers, these and other investigations were carried out in the low-density, Mach 10 tunnel. For example, extensive measurements of sphere drag were made over regimes extending from continuum to near-free-molecular, and a first-collision drag analysis was developed.

Of the other research, boundary-layer transition studies are here mentioned.

HYPERSONIC AERODYNAMICS OF BLUNT, SLENDER CONES

By

J. D. Whitfield

PRESSURE DISTRIBUTIONS

The aerodynamic of blunt, slender cones have been the subject of rather extensive theoretical and experimental research in the VKF during the past two years. Although this research was directed toward a more complete understanding of viscous effects on slender cones, the complexity of the problem demanded a rather detailed study of the inviscid and viscous effects as well as of the phenomena of interactions between inviscid and viscous flow fields.

The theoretical and experimental studies for slender cones included: (1) pressure distributions, (2) heat-transfer distributions, (3) static stability, and (4) zero-lift, viscous drag effects. The basic reference model selected for the experimental studies was a 9-deg half-vertex angle, spherically blunted cone with a nose to base radius ratio of 0.3. This model was selected because of the availability of characteristic solutions (see page 6). Other cone models were included to study the relative influences of cone angle and nose bluntness.

Zero-lift shock shapes and pressure distributions from the present studies were published by Lewis (Ref. 1) and were later corrected for source flow effects, for the sharper cone case, by Whitfield and Norfleet (Ref. 2). Lewis presented a correlation of the shock shape and pressure data in terms of parameters suggested by Cheng. Cheng's pressure parameter assumed $p_w \gg p_\infty$. A more general correlation could be obtained by using the pressure coefficient, C_p , and thus accounting for the free-stream static pressure level relative to the cone pressure level. Such a correlation was obtained by Griffith and Lewis (Ref. 3) and is shown in Fig. 1. It should be noted that this correlation covers a Mach number range from 10 to 20, with a variety of nose angles and nose bluntness ratios included. Experimentally, the limits of the correlation have not been established; however, it is apparent that the range of correlation is quite extensive.

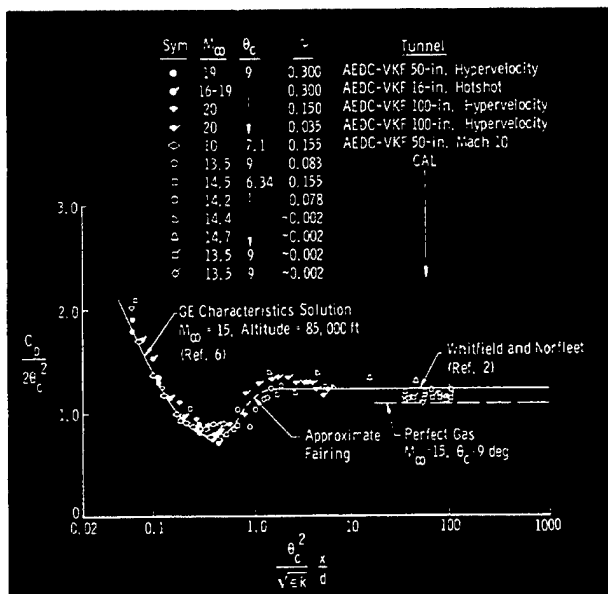


Fig. 1 Correlation of Zero-Lift Cone Pressures, $M_{\infty} = 10$ to 20

The pressure distribution data are essentially inviscid since a Reynolds number dependence was not found in the experiments. This conclusion is supported by theoretical considerations (Ref. 4) which indicate only second-order viscous effects on pressure distribution.

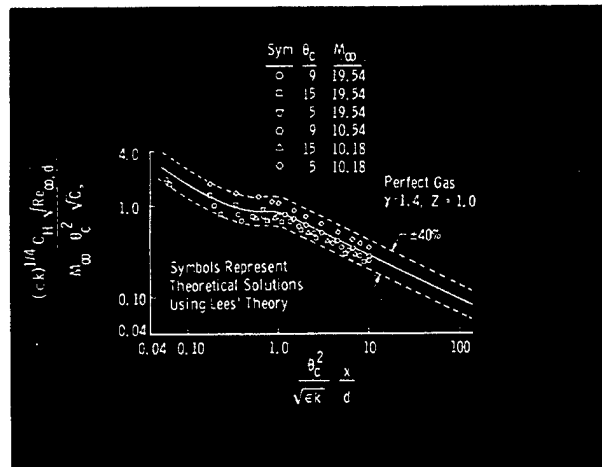
HEAT-TRANSFER DISTRIBUTIONS

Zero-lift heat-transfer data have also been correlated over a wide range of Mach numbers, cone angles, and nose bluntness ratios using a modification of parameters proposed by Cheng. The improvement obtained by the modifications employed by Griffith and Lewis (Ref. 3) is evident from a comparison of Figs. 2a and b, in which Lees' theoretical solutions are shown in terms of Cheng's original parameters (Fig. 2a) and the modified parameter (Fig. 2b). The marked improvement is apparent. Inspection of the ordinate parameter will reveal that θ_c^2 in Cheng's original parameter has been replaced by

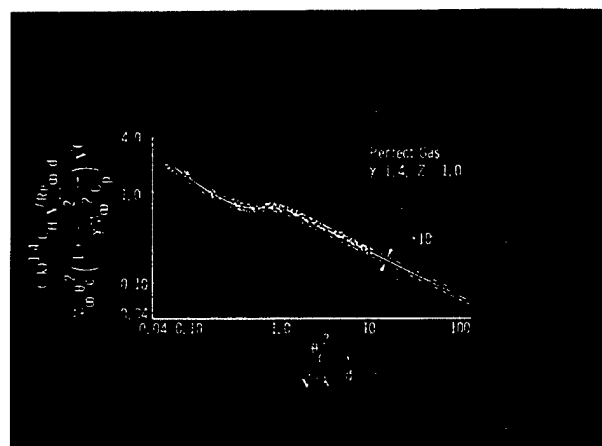
$$\theta_c^2 \left(1 + \frac{1}{\gamma M_{\infty}^2 C_p} \right)$$

Thus, the modified pressure distribution and heat-transfer parameters are directly analogous since they simply account for the fact that the free-stream static pressure is not always negligible with respect to the local cone pressure. It should be noted that Cheng's theory, from which his proposed parameters evolved, required $M_{\infty} \rightarrow \infty$, so that the condition that $p_w \gg p_{\infty}$ would have to be satisfied.

The VKF hotshot and Cornell Aeronautical Laboratory (CAL) shock tunnel heat-transfer data from blunt, slender cones are compared



a. Cheng's Correlation Parameter



b. A Modified Cheng Correlation Parameter

Fig. 2 Correlation of Theoretical Heat Transfer Rates to Blunted Cones Based on Lees' Heat Transfer Distribution (from Ref. 3)

to the theoretical estimates in terms of the modified Cheng heat-transfer parameter in Fig. 3 for spherical nose cones. Griffith and Lewis (Ref. 3) have also obtained a similar correlation for flat-nose cones. The theoretical estimates based on Lees' theory were obtained using a normal shock theoretical model, i.e., all conditions at the outer edge of the boundary layer were estimated assuming the fluid had passed through a normal shock wave and then expanded, isentropically, to local pressure conditions. The good agreement between Lees' theory and the sharper 6.34- and 9-deg cones must be considered, at present, fortuitous. Certainly, the normal shock approximation used in calculating the local flow properties over the cone should be invalid for the sharper cones. This "fortuitous" situation will also be seen to exist for the sharp cone drag data. The influence of flow field vorticity is the subject of continuing studies and is far from clear at present.

INVISCID STATIC STABILITY

The pressure distributions, as previously noted, were found, experimentally and theoretically, to be essentially inviscid; thus, it follows that the static stability would be affected also to only second-order by viscous effects. Measurements of the static stability (i.e., normal force and pitching moments) over a range of Reynolds numbers verified this expectation; hence, essentially inviscid results are included here.

Correlations of the measured normal-force and pitching-moment coefficients from a large number of blunt, slender cones were obtained by Whitfield and Wolny (Ref. 5) using simple Newtonian theory to illustrate the parametric relationships. The correlated data for normal-force and pitching-moment coefficients are shown in Figs. 4 and 5, respectively. Included here are measurements from ten blunt cones tested in the VKF (Mach 8 to 20) and from three sharp cones tested at NASA. The Mach number "independence" of these essentially inviscid, perfect gas, hypersonic, static stability data is clearly evident.

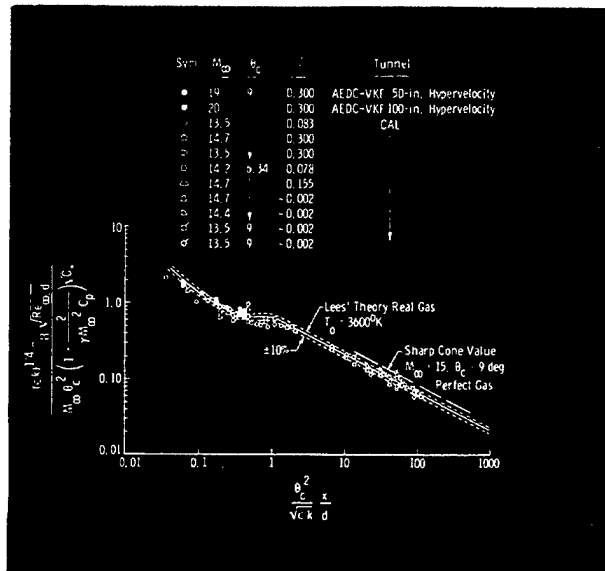


Fig. 3 Comparison of Theoretical and Experimental Heat Transfer Rates to Spherically Blunted Cones

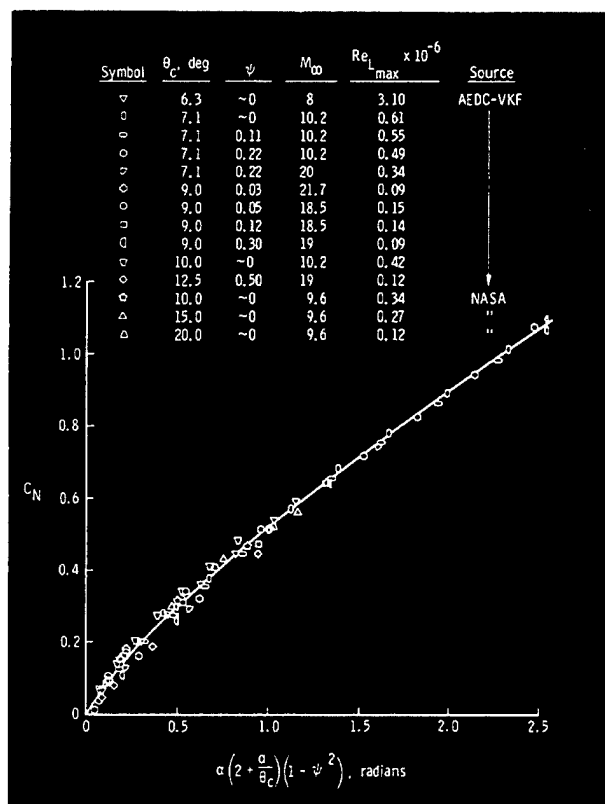


Fig. 4 Correlation of Normal-Force Coefficients for Blunt Slender Cones (from Ref. 5)

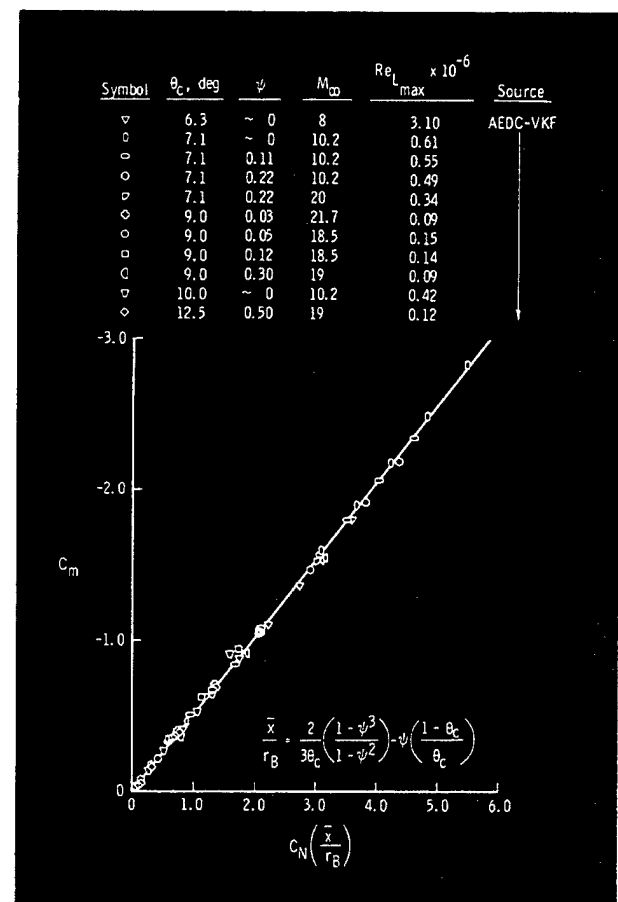


Fig. 5 Correlation of Pitching-Moment Coefficients from Blunt Slender Cones (from Ref. 5)

ZERO-LIFT VISCOUS DRAG EFFECTS

The often dominate role of viscous effects on the drag of slender bodies at hypersonic speeds is now widely recognized and has been the subject of many theoretical and experimental studies. The phenomena of interactions between inviscid and viscous flow fields complicate both theoretical and experimental studies of viscous effects at hypersonic speeds. The present research, conducted on simple, yet interesting, body shapes, was undertaken to aid in the clarification of these viscous interaction effects. Recent results of these viscous drag studies have been reported by Whitfield and Griffith (Ref. 4).

The similar solutions and integral method of Cohen and Reshotko were used to obtain theoretical estimates of the Blasius-type shear drag (see page 11), and the work of Probstein was used to obtain theoretical estimates of the displacement-induced pressure drag, displacement-induced friction drag, and the transverse-curvature-induced friction drag. All of the theoretical estimates were found, for a similar case (i.e., measurements for a given geometry in a given wind-tunnel), to be a function of the viscous parameter,

$$\bar{v}_{\infty} \equiv \frac{M_{\infty} \sqrt{C_{\infty}}}{\sqrt{Re_{\infty, L}}}$$

where $C_{\infty} \equiv \frac{\mu_w}{\mu_{\infty}} \frac{T_{\infty}}{T_w}$, the Chapman-Rubesin

viscosity coefficient. In general, it is found for the cold-wall case that the displacement-induced pressure and friction terms are small compared to the Blasius friction drag and the transverse-curvature-induced friction drag. For the hot-wall case, the displacement-induced friction and the transverse-curvature-induced friction terms become comparable. It should be noted here that the theoretical solutions were, in general, based on the normal shock theoretical model previously described under the heat-transfer section. This theoretical model, in spite of the obvious mismatch, was found to give a reasonable engineering approximation for all of the continuum cold-wall data.

Results from the theoretical solutions and the experimental cold-wall drag data are summarized in Fig. 6. The agreement between theory and experiment for $\bar{v}_{\infty} \leq 0.15$ is apparent. It is interesting to note from these data that the low-density, $\bar{v}_{\infty} > 0.2$, drag coefficients are essentially independent of the specific body shape. In fact, these data indicate in the low-density regime a stronger dependence on wall temperature than on body shape. This may be noted from comparison of the AEDC-VKF Low-Density Hypersonic Tunnel data ($T_w/T_0 \sim 0.25$) and the AEDC-VKF hotshot data ($T_w/T_0 \sim 0.1$).

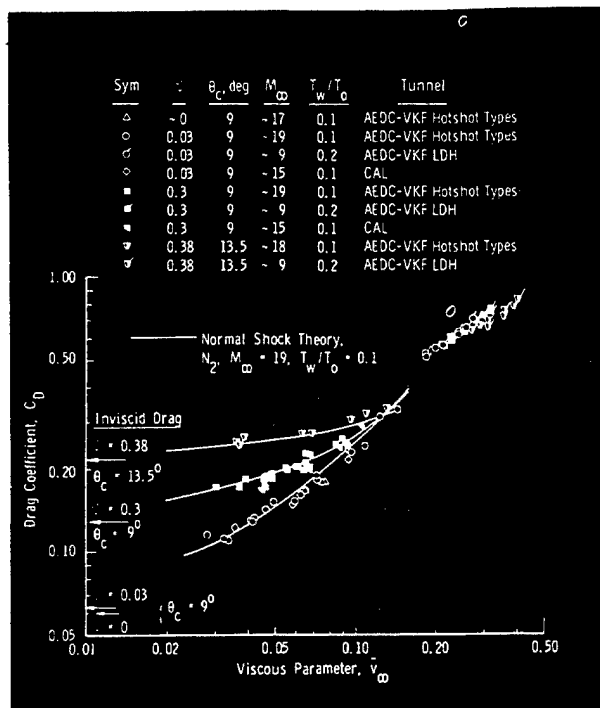


Fig. 6 Comparison of Hypersonic, Cold Wall Viscous Drag of Blunt, Slender Cones in Continuum and Rarefied Flow Regimes (from Ref. 4)

REFERENCES

1. Lewis, Clark H. "Pressure Distribution and Shock Shapes over Blunted Slender Cones between $M = 16$ and 19 ." AEDC-TN-61-81, August 1961.
2. Whitfield, Jack D. and Norfleet, Glenn D. "Source Flow Effects in Conical Hypervelocity Nozzles." AEDC-TDR-62-116, June 1962.
3. Griffith, B. J. and Lewis, Clark H. "A Study of Laminar Heat Transfer to Spherically Blunted Cones and Hemisphere-Cylinders at Hypersonic Conditions." AEDC-TDR-63-102, May 1963.
4. Whitfield, Jack D. and Griffith, B. J. "Viscous Effects on Zero-Lift Drag of Slender Blunt Cones." AEDC-TDR-63-35, February 1963.
5. Whitfield, Jack D. and Wolny, W. "Hypersonic Static Staility of Blunt Slender Cones." AEDC-TDR-62-166, August 1962.

RESEARCH ON LOW-DENSITY, HYPERSONIC FLOW

By

J. L. Potter

Since 1960, considerable effort has been devoted to experimental and theoretical studies of low-density, hypersonic flows in the VKF. Much of the experimental work is being carried out with the wind tunnel (Refs. 1 and 2) described on page 61; here, account is given of a number of aerodynamic studies.

THERMOMOLECULAR FLOW IN TUBES

This phenomenon has received relatively little attention in aeronautics. It may become important in such tasks as the measurement of very low pressures by means of a typical setup whereby the orifice at the point where knowledge of the pressure is desired is connected to the measuring instrument by a tube of small diameter. If Knudsen number is sufficiently large and there is an appreciable temperature gradient along the tube, the condition of zero mass flux along the tube does not correspond to equality of pressure along the tube. Thus, the measurement is in error. The most recent research on this subject has been reported by Arney and Bailey (Refs. 3 and 4). A typical example of the results of their investigation is given in Fig. 1.

Figure 1 represents a case where pressure at the cold end of a tube is three-fourths the pressure at the hot end when the Knudsen number is 10 and the temperatures differ by a factor of 1.955. In the course of these experiments, four weeks' time was allowed for outgassing the apparatus which was maintained under vacuum at elevated temperature during this period. Approximately ± 5 percent scatter is indicated by the data at higher Knudsen numbers, but it is noteworthy that this experimental scatter corresponds to only about ± 0.5 micron Hg. Based on data such as these, charts for use in estimating the thermomolecular flow correction have been prepared (Ref. 4).

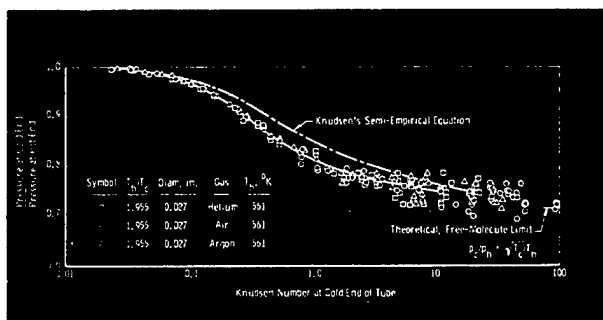


Fig. 1 Thermo-Molecular Flow Effect in Tubes (The symbols p and T represent pressure and temperature, respectively. Subscript c denotes cold end of the tube, and h denotes hot end.)

IMPACT-PRESSURE PROBES

The behavior of impact-pressure probes at low Reynolds numbers remains a subject for study, although much has been revealed by the research of earlier investigators. The high stagnation temperatures of Tunnel L in connection with the study of impact-pressure probes has led to the discovery of the variation in impact pressure illustrated by Fig. 2 (cf Ref. 5). It has been found that a correlation of the type shown in Fig. 3 is effective in establishing conditions under which a "small-orifice" effect is manifest.

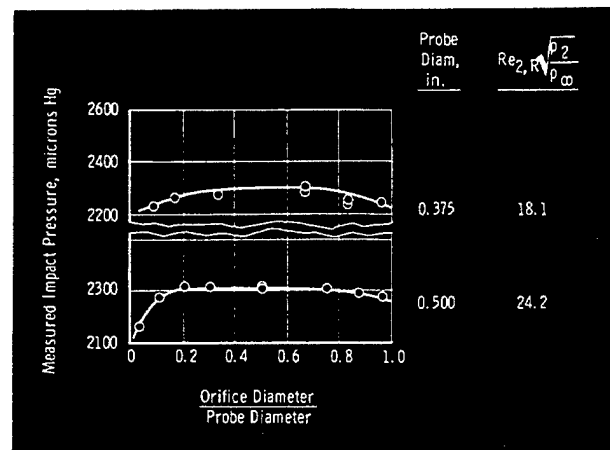


Fig. 2 Variation of Measured Impact Pressure with Orifice-to-Probe Diameter Ratio (Nitrogen Gas, Reservoir Temperature $T_0 = 5500^\circ\text{R}$, $M_\infty = 10.5$, $T_w/T_0 \approx 0.19$)

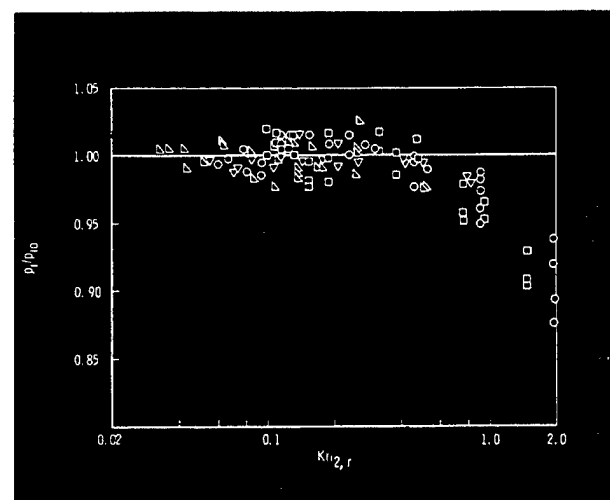


Fig. 3 Correlation of Data on Orifice Influence ($Kn_{2,r}$ is a Knudsen number based on conditions immediately downstream of a Hugoniot shock and probe orifice radius.)

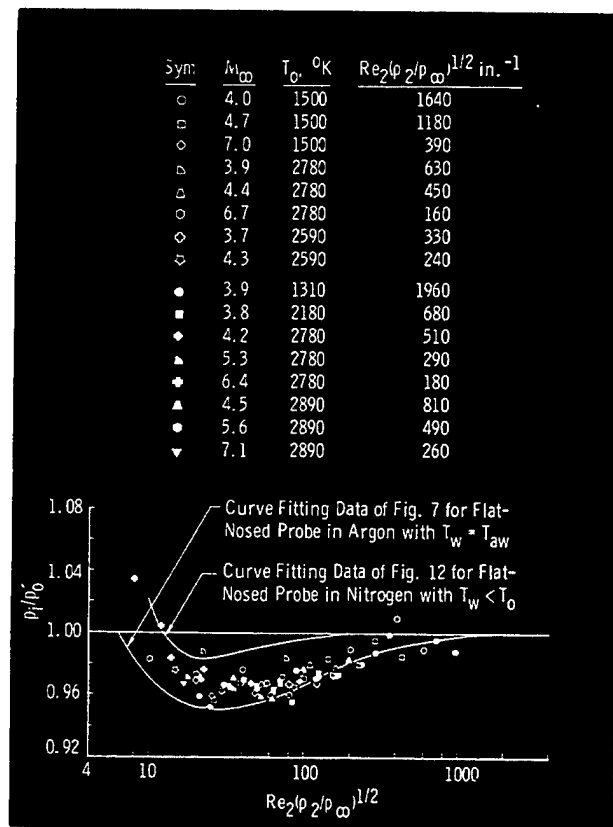


Fig. 4 AEDC-VKF Data for Flat-Nosed Probes in Argon with $T_w = 0.1$ to $0.3 T_0$ (Re_2 is a Reynolds number based on conditions immediately downstream of a Hugoniot shock and probe radius, ρ_2/ρ_∞ is the corresponding density ratio.)

The results of testing a flat-faced, cold-walled probe in argon (Ref. 6) are shown in Fig. 4. This particular example is presented because it demonstrates the often questioned decrease of impact pressure in the intermediate range of Reynolds numbers.

HEAT TRANSFER TO HEMISPHERICAL NOSES

Total heating rates of various blunt-nosed shapes have been measured in Tunnel L (Ref. 7). Total heat flux (Btu/sec) to the entire nose was measured and converted to average heat-transfer rate per unit area by dividing the total heat flux by the wetted area of the nose. Results for the hemispherical shape are shown in Fig. 5. The data in Fig. 5 are normalized by dividing the measured rates by those calculated from a theory for flows corresponding to higher Reynolds numbers. In the calculation, the theory of Fay and Riddell (Ref. 8) was used to obtain heating rate at the stagnation point, and the theory of Lees (Ref. 9) was used to obtain the distribution of heating rates around the hemisphere. The data in Fig. 5 clearly show the effects of reduced Reynolds numbers.

The results of three theories (Refs. 10, 11, and 12) applicable for low Reynolds num-

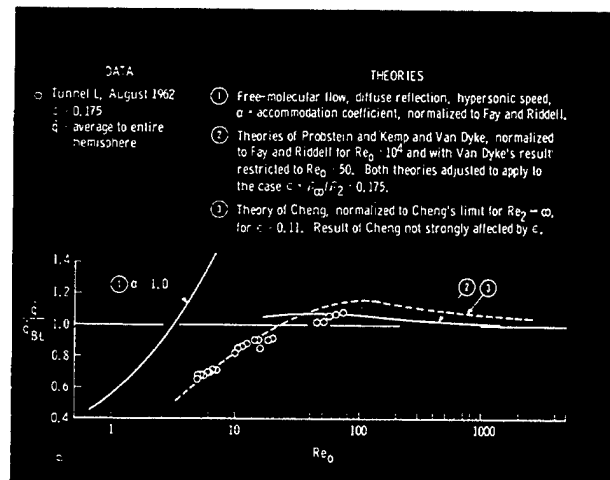


Fig. 5 Heat-Transfer Rates to Hemispherical Noses at Low Reynolds Numbers and Hypersonic Speeds ($q = \text{Btu/ft}^2\text{-sec}$, $Re_0 = U_\infty \rho_\infty R / \mu_0$ where U_∞ = free-stream velocity, ρ_∞ = free-stream density, R = hemisphere radius, and μ_0 = viscosity corresponding to total enthalpy; ϵ = density ratio across normal shock, subscript BL indicates value calculated by theory of Fay and Riddell.)

bers are shown in Fig. 5 for comparison. Qualitative agreement is evident, but some difference in actual values exists. It should be noted that the theories only yield the stagnation-point heating rate. Lees' distribution was assumed in converting these theoretical, stagnation-point values to average values. Thus, the comparison is possibly slightly qualitative for that reason. There are data for low Reynolds numbers showing Lees' distribution to be close to the experimental (Ref. 13).

DRAG OF CONICAL BODIES

Both sharp- and blunt-nosed cones have been tested to determine drag under low-density conditions. A water-cooled, sting-type balance capable of resolving drag forces on the order of 0.001 lb was used. The marked effects of combined low Reynolds number and high Mach number are illustrated by the data presented in Fig. 6. It may be seen there that the drag coefficient at $M_\infty/\sqrt{Re_\infty} \approx 0.3$ is roughly three times the value when $M_\infty/\sqrt{Re_\infty} \approx 0$ for the more bluff body and 12 times greater for the more slender body. For a 15-ft body at orbital velocity, this condition of $M_\infty/\sqrt{Re_\infty} \approx 0.3$ would exist at approximately a 300,000-ft altitude. More slender bodies, such as delta wings, tested in Tunnel L have yielded drag coefficients nearly twenty times greater than their essentially inviscid values. A photograph of a typical model being tested at a finite angle of attack in Tunnel L is shown in Fig. 7.

DRAG OF SPHERES

Through use of the low-density, hypersonic wind tunnel of the von Kármán Gas Dynamics

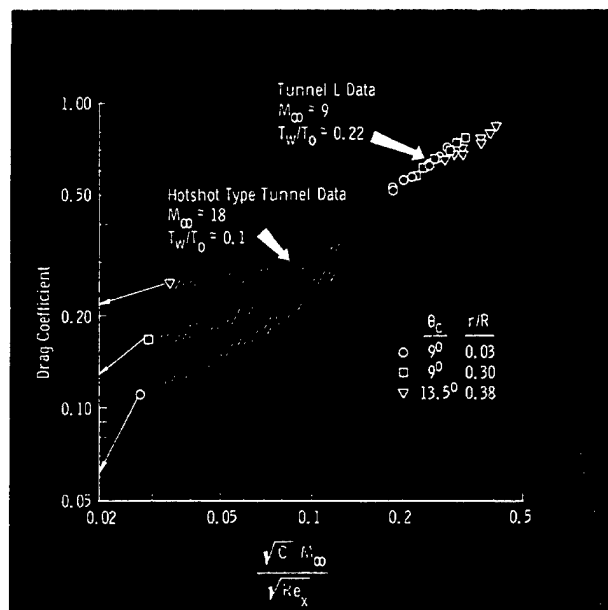


Fig. 6 Drag of Cones at Low Reynolds Number and Hypersonic Speed (Inviscid limits indicated by arrows to ordinate. The ratio of cone nose radius to base radius is denoted as r/R . θ_c = cone half-angle. C = coefficient in linear viscosity-temperature relation, M_∞ = free-stream Mach number, Re_x = Reynolds number based on free-stream conditions and axial length of body.)

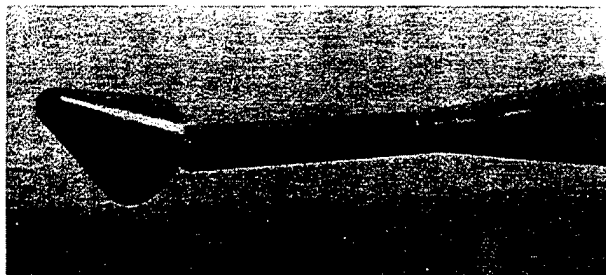


Fig. 7 Blunt Cone on Drag Balance in Tunnel L

Facility, drag of spheres has been measured under hypersonic, cold-wall support-free conditions in a nonreacting flow in which molecular vibration was frozen (Ref. 14). Data were obtained for a nominal free-stream Mach number of 11 and for Reynolds numbers from 1 to 10 based on conditions immediately downstream of the normal shock and sphere diameter. Figure 8 is a photograph of the track of a small sphere falling through the test section of Tunnel L and being deflected by the drag force, which was calculated by knowledge of the mass of the sphere, time interval, and distance between the bright images on the photo. These data were supplemented by measurements at a nominal Mach number of 10 where a conventional balance was used, and Reynolds numbers downstream of the shock as high as 10^4 were investigated in the cold-wall condition.

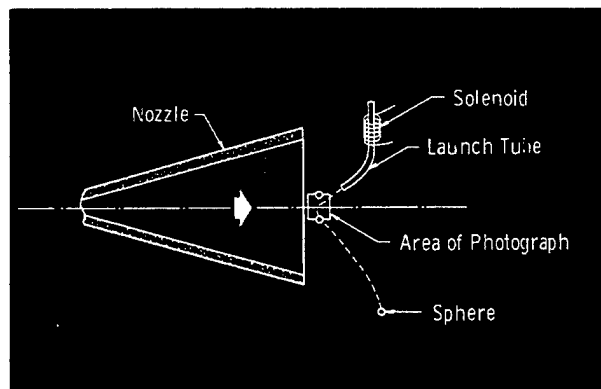


Fig. 8 Typical Trajectory of Sphere during Free Flight through Test Section

The experimental results have been analyzed both from the point of view of continuum flow with second-order viscous effects and from the standpoint of a noncontinuum concept, taking account of first collisions between re-emitted and free-stream molecules. In the former case, a drag coefficient representation of the form

$$C_D = C_{D_{\text{inviscid}}} + K_1/\sqrt{Re_2} + K_2/Re_2$$

was shown to fit the data very closely when K_1 and K_2 are allowed to be functions of free-stream Mach number and wall-to-total enthalpy ratio. In all cases, K_2 was found to be negative in sign.

The new first-collision analysis is numerically indeterminate because of the lack of a method for explicit calculation of mean free path in polyatomic gases with consideration of intermolecular forces. However, the form of the derived equation for drag coefficient appears to fit the experimental data over a considerable range of Knudsen numbers if a free constant is used in the expression for mean free path. It is considered that this constant is influenced by the type of intermolecular and gas-solid interactions occurring. A fully accommodated, diffusely reflected type of

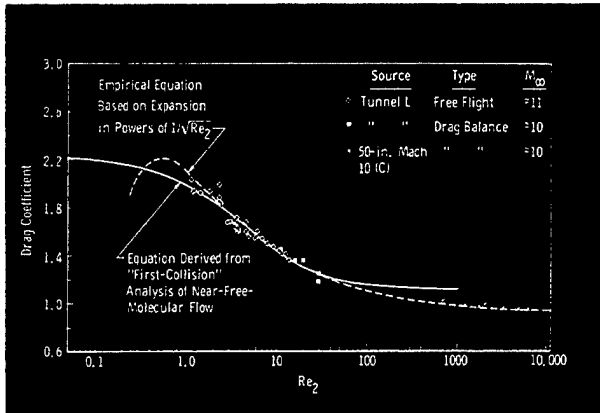


Fig. 9 Drag of Spheres at Low Reynolds Numbers and Hypersonic Speeds (Re_2 is Reynolds number based on conditions immediately downstream of normal shock and sphere diameter, assuming a Hugoniot shock.)

surface interaction was assumed in the analysis.

Figure 9 shows a part of the results of this research.

SHOCK WAVES IN ARGON

An experimental investigation has been made to determine the pressure distribution, shock shape, detachment distance, and wave thickness for spheres, and the latter three characteristics for flat-faced bodies in heated argon where Mach number was from 4 to 14, stagnation temperature was from 1900 to 4100°K, and Reynolds number downstream of the normal shock waves was 25 to 225 based on radius (Ref. 15). The purposes of this investigation were to determine the validity of the various theories available for predicting the above properties in the low-density flow regime and to extend available data to lower Reynolds numbers.

When argon is used as the working gas, at the nozzle exit and some distance downstream there is a clearly visible, light-blue jet surrounded in most cases by a pink glow. A survey of the nozzle flow with an impact-pressure probe showed that this light-blue region corresponded to the core of high-speed flow. This natural glow, thought to be caused by radiation from relaxing metastable argon atoms, enabled this study of the shock properties in front of spheres and flat-faced bodies to be made by simply photographing the flow field, wherein the brightness was proportional to the number density of radiating atoms.

Photographs of the shocks generated by the spheres and flat-faced bodies were analyzed with a photo-densitometer to determine the shock shape, detachment distance, and wave thickness. A study of the variation of film density upstream, downstream, and through the shock wave indicated that the assumption that the film density was proportional to the flow density was justified.

In Fig. 10 the results of the measurement of shock detachment distance for spheres at

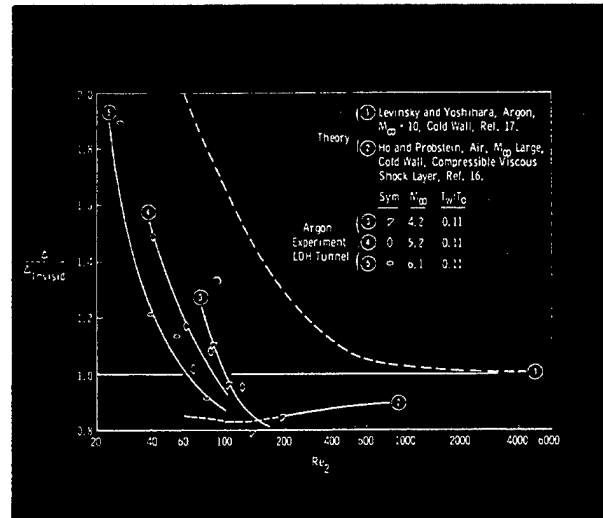


Fig. 10 A Comparison of Theoretical and Experimental Shock Detachment Distances for Hemispheres (Δ is the detachment distance or shock-layer thickness. Re_2 is a Reynolds number based on conditions immediately downstream of a normal shock wave and hemisphere diameter, assuming a Hugoniot shock.)

different wall-to-stagnation temperature ratios is shown. It will be noted that the shock detachment distance is a function of Mach number, Reynolds number, wall temperature, and body shape. A study of the magnitude of the shock-wave and boundary-layer thicknesses indicates that in the present tests these layers are incipiently or fully merged. As the Reynolds number decreases, the shock detachment distance increases to values more than double the "inviscid" values. Also, for the bodies where the wall-to-stagnation temperature ratio is 0.1, there is evidence to confirm the decrease in shock detachment distance to a value less than the inviscid value, as predicted by Ho and Probstein (Ref. 16), before the increase as mentioned above for the lowest Reynolds number.

REFERENCES

- Potter, J. L., Kinslow, M., Arney, G. D., Jr. and Bailey, A. B. "Initial Results from a Low-Density Hypervelocity Wind Tunnel." *Progress in Astronautics and Rocketry*, Ed. by F. R. Riddell, Academic Press, 1962, pp. 599-624.
- Potter, J. L. and Boylan, D. E. "Experience with an Overexpanded Nozzle in a Low-Density, Hypervelocity Wind Tunnel." *AEDC-TDR-62-85*, April 1962.
- Arney, G. D., Jr. and Bailey, A. B. "Effect of Temperature on Pressure Measurements." *AIAA Journal*, Vol. 1, No. 12, Dec. 1963, pp. 2863-2864.
- Arney, G. D., Jr. and Bailey, A. B. "Addendum to an Investigation of the Equi-

- librium Pressure Along Unequally Heated Tubes." AEDC-TDR-62-26, February 1962.
5. Bailey, A. B. and Boylan, D. E. "Some Experiments on Impact-Pressure Probes in a Low-Density, Hypervelocity Flow." Proceedings of the 1962 Heat Transfer and Fluid Mechanics Institute, Ed. by F. E. Ehlers, et. al. Stanford University Press, 1962, pp. 62-75.
 6. Potter, J. Leith and Bailey, Allan B. "Pressures in the Stagnation Regions of Blunt Bodies in the Viscous-Layer to Merged-Layer Regimes of Rarefied Flow." AEDC-TDR-63-168, September 1963; AIAA Conference on Physics of Entry into Planetary Atmospheres, Cambridge, Mass., 26-28 Aug. 1963.
 7. Potter, J. L. and Miller, J. T. "Total Heating Load on Blunt, Axisymmetric Bodies in Low-Density Flow." AIAA Journal, Vol. 1, No. 2, Feb. 1963, pp. 480-481.
 8. Fay, J. A. and Riddell, F. R. "Theory of Stagnation Point Heat Transfer in Dissociated Air." Jour. of the Aero/Space Sciences, Vol. 25, No. 2, Feb. 1958, pp. 73-85.
 9. Lees, L. "Laminar Heat Transfer over Blunt-Nosed Bodies at Hypersonic Flight Speeds." Jet Propulsion, Vol. 26, No. 4, April 1956, pp. 259-269.
 10. Cheng, H. K. "Hypersonic Shock-Layer Theory of the Stagnation Region at Low Reynolds Number." Cornell Aero. Lab. Rept. No. AF-1285-A-7, April 1961.
 11. Probstein, R. F. and Kemp, N. H. "Viscous Aerodynamic Characteristics in Hypersonic Rarefied Gas Flow." Jour. of the Aero/Space Sciences, Vol. 27, No. 3, March 1960.
 12. Van Dyke, M. "Second-Order Compressible Boundary-Layer Theory with Application to Blunt Bodies in Hypersonic Flow." AFOSR-TN-61-1270, July 1961.
 13. Wittliff, C. E. (Cornell Aero. Lab.) Personal communication, 3 August 1962.
 14. Kinslow, M. and Potter, J. L. "The Drag of Spheres in Rarefied, Hypervelocity Flow." AEDC-TDR-62-205, December 1962; AIAA Journal, Vol. 1, No. 11, p. 2467, November 1963.
 15. Bailey, A. B. and Sims, W. H. "The Shock Shape and Shock Detachment Distance for Spheres and Flat-Faced Bodies in Low-Density, Hypervelocity Argon Flow." AEDC-TDR-63-21, January 1963.
 16. Ho, Hung-Ta and Probstein, R. F. "The Compressible Viscous Layer in Rarefied Hypersonic Flow." Brown University, ARL-TN-60-132, August 1960.
 17. Levinsky, E. S. and Yoshihara, H. "Rarefied Hypersonic Flow Over a Sphere." Hypersonic Flow Research, Academic Press, New York, 1962, pp. 81-106.

RESEARCH ON BOUNDARY-LAYER TRANSITION

By

J. L. Potter and J. D. Whitfield

The study of transition from laminar to turbulent flow in boundary layers has been directed toward understanding the roles of several factors which affect the location of transition. Corresponding reactions of certain aerodynamic quantities which are sensitive to the location of transition also have been investigated, the most important one of these being base pressure (Refs. 1-4).

Recognizing that unit Reynolds number (Ref. 5) often plays a prominent role in fixing the location of transition, certainly in most wind tunnels and apparently in at least some free-flight cases, an effort was made to demonstrate the importance of considering that factor. The results obtained showed the effect of transition location and its response to varying unit Reynolds number in measurements of transition-sensitive quantities as well as in studies of transition alone. For an example of this, refer to Fig. 1, where it may be seen that a class of base pressures is correlated by simply considering the

relative location of transition. The class of base flows referred to is characterized by transition occurring in the wake between the base of the body and closure of the wake downstream. Following are brief summaries of studies of some major problems in the field of boundary-layer transition.

THE TRANSITION PROCESS

A hot-wire anemometer was used to survey laminar, transitional, and the initial part of fully turbulent boundary layers on hollow cylinders having their major axes parallel with the free-stream direction. Care was taken to ensure that the bow shock wave was swallowed. Thus, since cylinder radius was sufficiently greater than boundary layer thickness, the hollow cylinders were effectively equivalent to flat plates. Figure 2 shows the models and some of the boundary-layer probes.

Relatively early in the use of the hot-wire anemometer to detect transition, it became apparent that the transition region

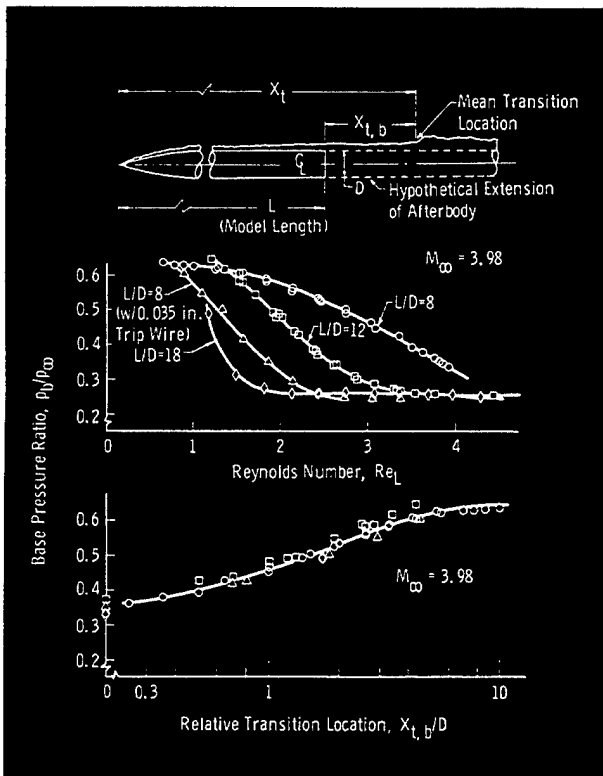


Fig. 1 Correlation of Base Pressure Data with the Relative Location of Transition

was not characterized by a sudden and violent onset of fluctuations but was rather an orderly, developing process which appeared to originate at or near the leading edge. The hot-wire was used to survey the entire boundary-layer flow field. Most of these surveys were taken with a wire operated at a constant current. These data are presented here in terms of isoline diagrams of constant hot-wire output, e^2 , which is the mean-square signal from the hot-wire equipment. An electronic squaring circuit developed by Kovasznay was used to obtain this mean signal. The "noise" noted in the figures refers to the electronic noise of the hot-wire equipment. The locations shown for the noise level correspond to the condition where the hot-wire signal and electronic noise were approximately equal.

Figure 3 shows an example survey. A salient feature is the relatively intense stratification of fluctuations observed in the laminar region and the early portion of the transition region. The existence of this critical layer, which is indicated by stability theory, is well known in regard to incompressible flow from the work of Schubauer and Skramstad and has been observed in supersonic flow by Laufer and Vrebalovich, and Demetriades. However, these earlier experiments were concerned with studies of laminar instability, so none of these data enabled comparison of the magnitude of fluctuations in the laminar

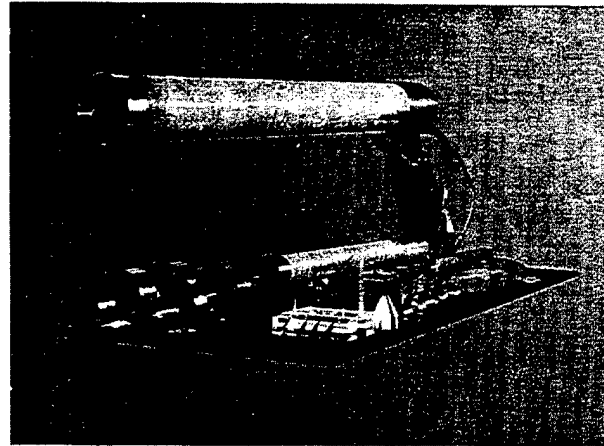


Fig. 2 Models and Boundary-Layer Probes, AEDC-VKF Studies

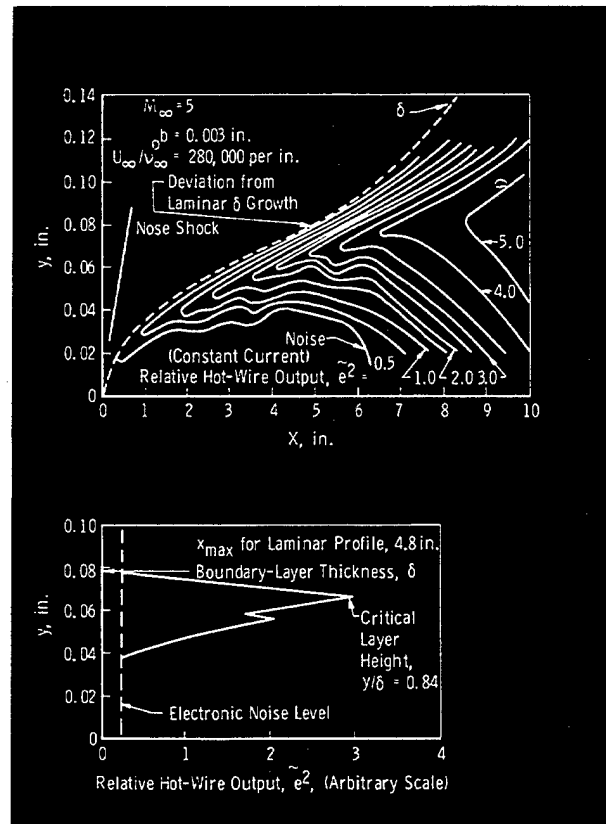


Fig. 3 Hot-Wire Output near Leading Edge for $b = 0.003$ in. and $M_{\infty} = 5$ ($b =$ thickness of leading edge, $y =$ height above surface, $x =$ distance from leading edge)

region and those in the transition region. The fact that these disturbances are of the same order creates a source of error in the determination of a transition "point" from hot-wire traverses at heights above the surface, since a different point might be indicated for each different height of the probe above the surface.

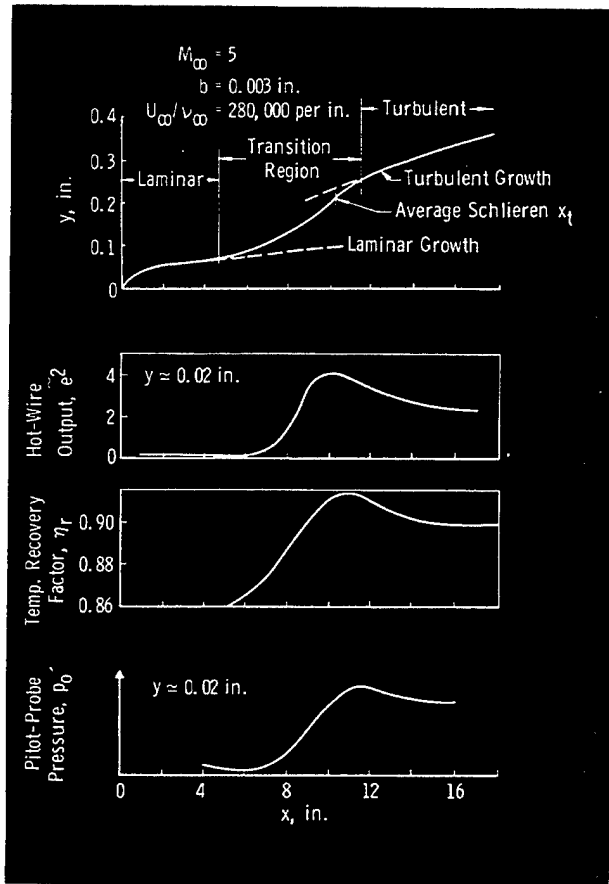


Fig. 4 Comparison of Methods of Transition Detection for $M_\infty = 5$

It was shown that a maximum hot-wire output for $y \rightarrow 0$ can be located with reasonable precision (Ref. 6). The measurement of surface temperature distributions on the same model revealed that this maximum hot-wire signal near the surface corresponded to the maximum surface temperature. Comparisons of various methods of detection are shown in Fig. 4. It may be observed that the similarity between the maximum hot-wire signal and the maximum surface temperature extends into the fully developed turbulent region where the hot-wire signal and the surface temperature become substantially constant. The same general relation exists between all the various methods of transition detection.

An interesting result of the study of the critical layer for various unit Reynolds numbers, leading-edge thicknesses, and Mach numbers is that the height of the critical layer can be represented reasonably well in terms of boundary-layer thicknesses and Mach number, i.e.,

$$y_c/\delta = f(M_\infty)$$

This relationship is shown in Fig. 5, where the present data are compared with subsonic

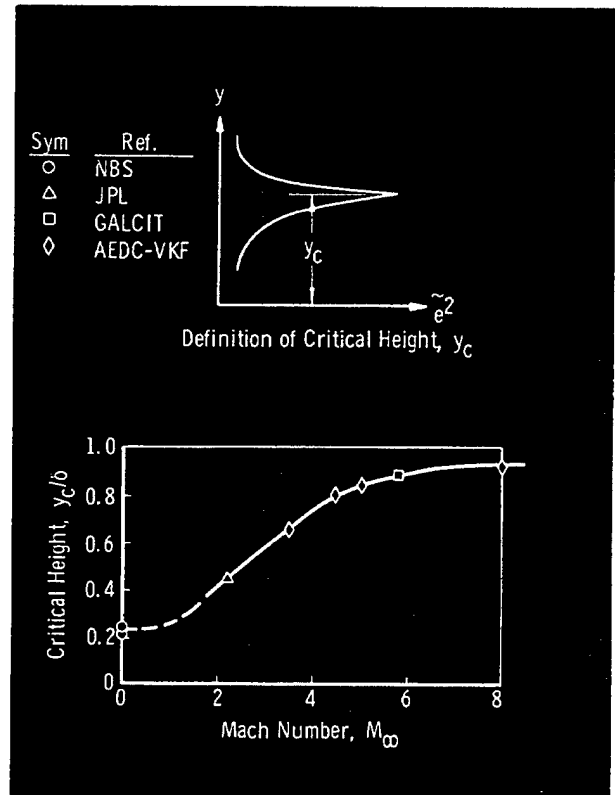


Fig. 5 Critical Layer Height as a Function of Mach Number

data from Klebanoff and Tidstrom and the data from Laufer and Vrebalovich, and Demetriades.

Laufer and Vrebalovich suggested that free-stream turbulence, acting as a forcing function, causes an interaction between the shock wave and the boundary layer, and this in turn produces disturbances in the boundary layer. Having determined that the disturbances and their distribution in the boundary layer are not peculiar to very sharp leading edges or caused by separation at the leading edge, the present study indirectly supports their hypothesis.

INFLUENCE OF SLIGHT LEADING-EDGE BLUNTNESS

In earlier papers (Refs. 6 and 7), the authors presented discussions of the influence of bluntiness, including extensive experimental data for a Mach number of approximately three. Perhaps it is desirable to attempt to define the term "slight bluntiness." For present purposes it is believed sufficient to stipulate that thickness of the leading edge, b , and the wetted length from the stagnation point to the beginning of transition, x_t , are related such that $x_t \gg b$ or $x_t/b > 100$. All the data considered in Refs. 6 and 7 correspond to $x_t/b = O(1000)$.

The importance of slight leading-edge bluntness in connection with transition location, which had been suggested earlier, was further verified in Refs. 6 and 7, where it was shown that changing the thickness of the leading edge from 0.0015 to 0.0030 in. could result in the Reynolds number of transition increasing by 355,000, or more than twenty percent in a typical case. Additional data on this subject have been obtained with a Mach number of eight and will soon be published. The models on which these effects were noted were either flat plates or hollow cylinders, both parallel to the flow direction.

INFLUENCE OF SURFACE ROUGHNESS

Investigation of the influence of surface roughness was initially undertaken with the study of published experimental data. One of the present authors (Ref. 8) derived a correlation of available data on the basis of the Pohlhausen boundary-layer profile parameter after the manner of Taylor's early analysis of the effect of stream turbulence on transition. Only single, two-dimensional elements on a flat plate in low-speed flow were considered.

Later, experimental studies of roughness influences at supersonic speeds were undertaken, and the effort to obtain a method for predicting the influence of roughness was extended to compressible flows. Two parameters, one representing effectiveness of roughness and the other representing relative movement of transition, have been proposed for flows with no pressure gradients (Refs. 6 and 7). It was shown that the former purpose is served by Re'_k , where

$$Re'_k = Re_k (T_k/T_w)^{0.5+\omega}$$

and

Re_k = Reynolds number based on height of roughness element and flow conditions at that point in the undisturbed boundary layer

T_k = static temperature at height and station of roughness in undisturbed flow

T_w = wall temperature of body (const.)

ω = exponent in viscosity-temperature relation, $\mu \sim T^\omega$

The position parameter was given in Ref. 7 as

$$\sqrt{x_t/x_{t0}} = (Re'_k/\epsilon) \sqrt{x_k/x_{t0}}$$

where

x_t = wetted distance along surface from stagnation point to transition

x_{t0} = as above, except with no roughness

ϵ = Re_k where $x_t = x_k$

x_k = length from stagnation point to location of roughness

These parameters are for cases where

$$x_k \leq x_t \leq x_{t0}$$

Figure 6 shows a large collection of data presented in the form of the parameters defined in Ref. 7. Considering the fact that variable factors of unknown significance, aside from roughness, were present in the different experiments represented in Fig. 6, the correlation is about as good as one might reasonably expect in dealing with transition data.

Data included in Fig. 6 all apply to bodies with walls at or near adiabatic recovery temperature. In view of the strong dependence of Re_k on wall temperature, it is particularly interesting to investigate situations where Re_k was varied by changing wall temperature alone. It has been shown that cases involving heat transfer are also correlated by the parameters derived from analysis of data for zero heat transfer (Ref. 7). Thus, it is possible to evaluate the effect of heat transfer on transition due to roughness, and that enables investigation of the transition reversal phenomenon. The experimentally demonstrated rise and subsequent fall of Re_t with decreasing T_w is well known. Some have argued that the increased effectiveness of roughness due to wall cooling was not sufficient to explain transition reversal on nominally smooth bodies. However, in Ref. 9 it is shown that roughness in conjunction with wall cooling can cause transition reversal.

Although the procedure devised for estimating the location of transition is applicable to subsonic and supersonic flows with and without heat transfer, it is not intended for or tested in situations where pressure gradients exist. Therefore, it is of interest to note that, when used in a few cases for estimation of roughness necessary to achieve transition on models such as blunt, conical shapes, it gave good results; however, further research is required to establish the range of its applicability.

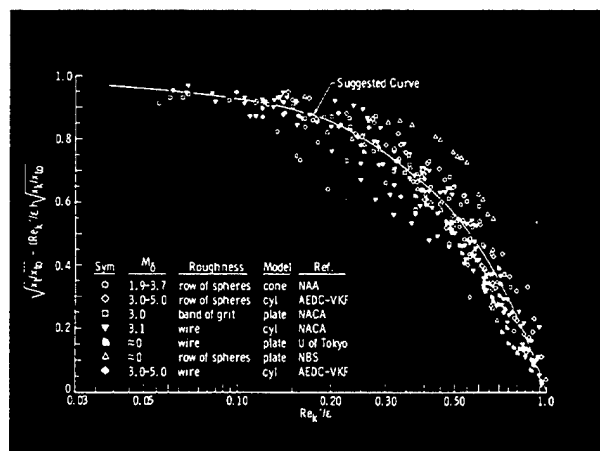


Fig. 6 Correlation of Typical Data ($M_0 \approx 0-5$, $T_w \approx T_{aw}$)

REFERENCES

1. Potter, J. Leith and Whitfield, Jack D. "Preliminary Study of the Effect of Unit Reynolds Number on Transition Sensitive Data." AEDC-TN-57-37, September 1957.
2. Potter, J. Leith, Whitfield, Jack D., and Strike, William T. "Transition Measurements and the Correlation of Transition Sensitive Data." AEDC-TR-60-4, February 1960.
3. Potter, J. Leith and Whitfield, Jack D. "Relation between Transition Location and Pressure in Separated Shear Flows." Journal of the Aero/Space Sciences, Vol. 27, No. 9, September 1960.
4. Whitfield, Jack D. and Potter, J. Leith. "On Base Pressures at High Reynolds Numbers and Hypersonic Mach Numbers." AEDC-TN-60-61, March 1960.
5. Whitfield, Jack D. and Potter, J. Leith. "The Unit Reynolds Number as a Parameter in Boundary Layer Stability." AEDC-TN-58-77, September 1958 (Also Journal of the Aero/Space Sciences, Vol. 29, No. 3, March 1959).
6. Potter, J. Leith and Whitfield, Jack D. "Effects of Unit Reynolds Number, Nose Bluntness, and Roughness on Boundary-Layer Transition." AEDC-TR-60-5, March 1960.
7. Potter, J. Leith and Whitfield, Jack D. "Effects of Slight Nose Bluntness and Roughness on Boundary-Layer Transition in Supersonic Flows." Journal of Fluid Mechanics, Vol. 12, Part 4, 1962, pp. 501-535.
8. Potter, J. Leith. "Subsonic Boundary-Layer Transition Caused by Single Roughness Elements." Journal of the Aeronautical Sciences, Vol. 24, February 1957, p. 158.
9. Potter, J. Leith and Whitfield, Jack D. "The Relation between Wall Temperature and the Effect of Roughness on Boundary-Layer Transition." Journal of the Aero/Space Sciences, No. 8, August 1961.

AERODYNAMIC CONTROLS

The two basic types of aerodynamic controls which are employed with high-speed vehicles are the so-called conventional aerodynamic controls and the reaction jet controls.

The former, usually in the form of deflectable surfaces, may have to operate in complex flow fields. This is due to the presence of blunt leading edges which are required to alleviate the aerodynamic heating and which introduce large entropy gradients, and to the existence of relatively thick boundary layers. Special methods are therefore required to predict the effectiveness of control surfaces in these environments.

In the present age of suborbital and re-entry glide vehicles, a reaction jet system for controlling the vehicle attitude and trajectory is being used because aerodynamic controls of the conventional type, such as fins, ailerons, rudders, etc., are ineffective at the low dynamic pressures encountered. The reaction jet system can also be used at the lower altitudes where conventional controls are used, and in this environment additional gains are possible because of the favorable interaction with the inviscid and boundary-layer flow field of the vehicle.

Some aspects of these problems of aerodynamic control, have been studied at the VKF, as outlined in the next two contributions.

ON CONTROL SURFACES SUBMERGED IN THICK BOUNDARY LAYERS

By

J. D. Gray

A number of experimental test programs which have been conducted in the VKF were concerned with the change in forces on aerodynamic surfaces completely submerged in a turbulent boundary layer. The objective of these tests was to simulate the effects of spanwise entropy variations over control fins for re-entry guidance. In order to contribute to an improved awareness of the governing factors which account

for the loss in control surface effectiveness, a strip-type analysis of the problem was made (Ref. 1). For simplicity, it was assumed that the boundary-layer Mach number profile varies in an exponential manner, and that the local normal-force curve slope, $C_{n\alpha}$, is a linear function of Mach number, M , at subsonic speeds varying between a_0 at $M = 0$ and a_1 at $M = 1$. In the supersonic range, $C_{n\alpha}$ was assumed to be a function of

M^{-K} and to have a value of a_1 at $M = 1$. Based upon these assumptions a general integral expression for the total normal-force curve slope (C_{N_α}) is given by

$$C_{N_\alpha} = \frac{a_0}{AM_\infty^2} \int_0^{\delta^*} M^2 x dy + \frac{a_1 - a_0}{AM_\infty^2} \int_0^{\delta^*} M^3 x dy + \frac{a_1}{AM_\infty^2} \int_{\delta^*}^{\delta} M^{2-K} x dy + \frac{a_1}{M_\infty^K A} \int_{\delta}^h x dy$$

where:

A = reference area

a_0 = local normal-force curve slope at $M = 0$

a_1 = local normal-force curve slope at $M = 1$

h = span of surface

K = exponent describing variation of local normal-force curve slope with Mach number

M = local Mach number

M_∞ = Mach number at $y = \delta$

x = local chord

y = height

δ = height where $M = M_\infty$

δ^* = height where $M = 1$

to that for the fin in uniform flow. The analysis is shown to effectively account for both planform variations and relative submersion of the planform in turbulent boundary layers at $M_\infty \approx 2.5$. Tests at Mach numbers from 1.5 through 3.5 have confirmed the applicability of the analysis, but it is necessary to determine the influence of Mach number on the section characteristics (C_{N_α}) in uniform flow to properly choose the value of parameter, K .

REFERENCE

1. Gray, J. Don. "An Analysis of the Normal-Force Characteristics of Aerodynamic Surfaces Submerged in Supersonic Boundary Layers." AEDC-TN-61-113, September 1961.

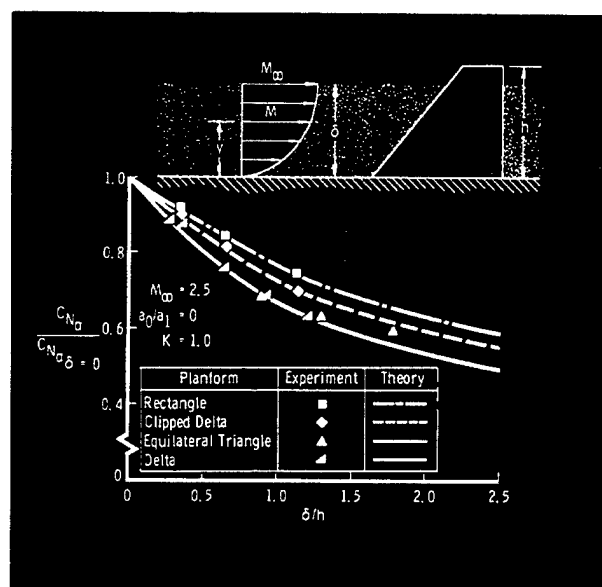


Fig. 1 Comparison of Theory and Experiment for Control Surfaces Submerged in a Turbulent Boundary at Mach 2.5

INTERACTIONS PRODUCED BY SONIC LATERAL JETS LOCATED ON SURFACES IN A SUPERSONIC STREAM

By

W. T. Strike and C. J. Schueler

At this time, vehicles such as the X-15 and the more advanced X-20 Dyna-Soar are designed with movable, conventional, aerodynamic control surfaces (ailerons, rudders, etc.) and reaction control jets. When these vehicles are flown within the corridor of continuous flight and the reaction jets are used for control, an interaction of the jet flow with the free stream and boundary-layer flow is produced. This interaction

creates forces significantly larger than would be obtained from only the jet reaction. The VKF studies were directed toward the experimental determination and analytical prediction of the interaction loadings.

A graphical illustration of the flow field and the interaction loading produced by a lateral jet from a surface in a supersonic stream is presented in Fig. 1. This

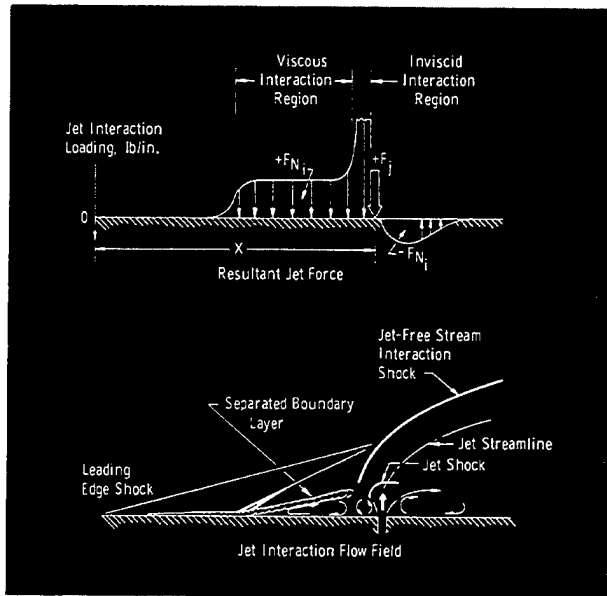


Fig. 1 Lateral Jet Interaction in Supersonic Stream

interpretation of the flow field is based in part on pictorial results similar to those in Fig. 2. The net interaction loading (FN_i) when added to the reaction force of the jet (F_j) constitutes the total force produced by a control jet operating within the flight corridor. In the theoretical analysis (Ref. 1), the interaction loading was assumed to be a linear combination of the loading produced by the interaction of (1) the free stream with the jet stream (inviscid interaction) and (2) the separated boundary layer upstream of the jet (viscous interaction). Theoretical and experimental results indicated that the ratio of the interaction loading to the jet reaction force (FN_i/F_j) increased with the free-stream Mach number and a decreasing ratio of jet stagnation to free-stream static pressure (p_j/p_∞). An example of the type of correlation obtained between the theoretical flat plate analysis and the experimental data of the interaction force produced by a lateral jet from a rectangular and circular nozzle into a Mach 5 free stream is given in Fig. 3. For a given jet momentum, the rectangular lateral jet produced a larger interaction loading than circular nozzles. In comparison to the theoretical procedures of Refs. 2 and 3, the present analytical method of estimating interaction force was in better agreement with the experimental results.

The studies showed that the relative location of a particular nozzle configuration (circular, multiple circular, or rectangular) had a strong effect on the optimum or maximum resultant force produced by a control jet. It was found that the two-dimensional nozzle (or slot) produced the maximum jet control force ($FN_i + F_j$) when located near the trailing edge of a body. In the case of a circular nozzle, a large

region of additive loading was produced downstream of the jet. Therefore, on a two-dimensional surface the nozzle should be positioned ahead of the trailing edge.

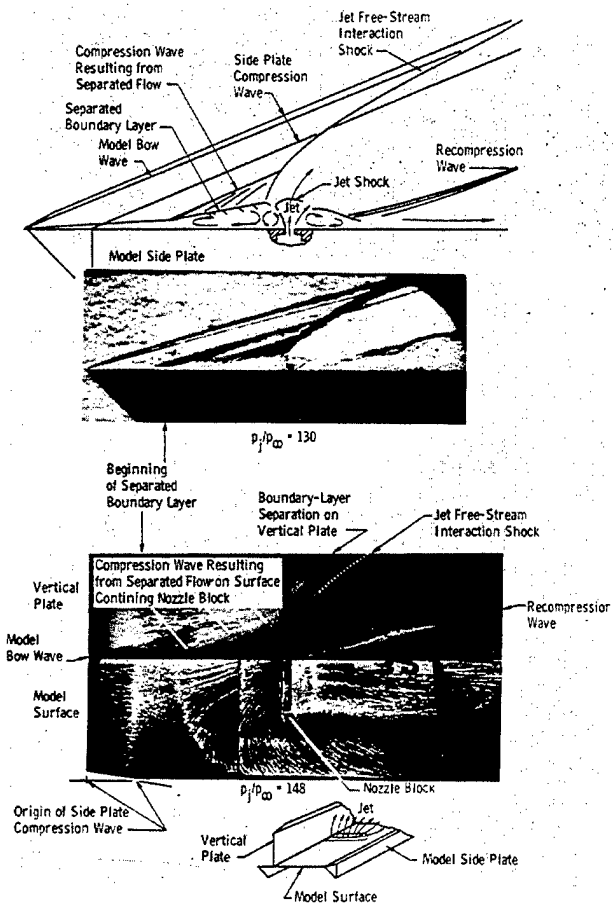


Fig. 2 Flow Visualization of Lateral Jet Interaction

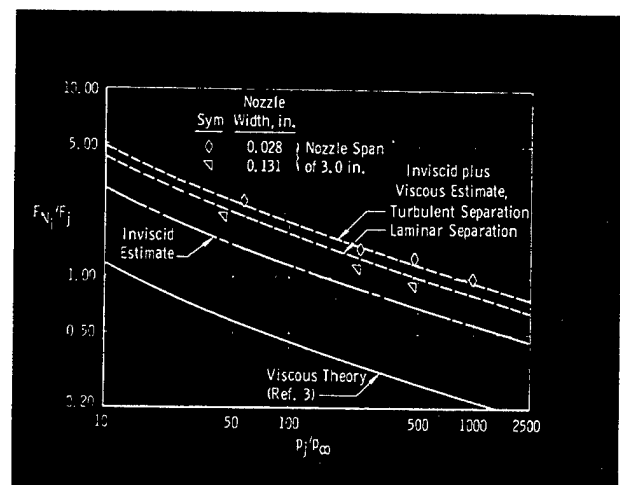


Fig. 3 Lateral Jet Effectiveness, (Rectangular Nozzle) $M_\infty = 5.0$, $Re_X = 2.2 \times 10^6$

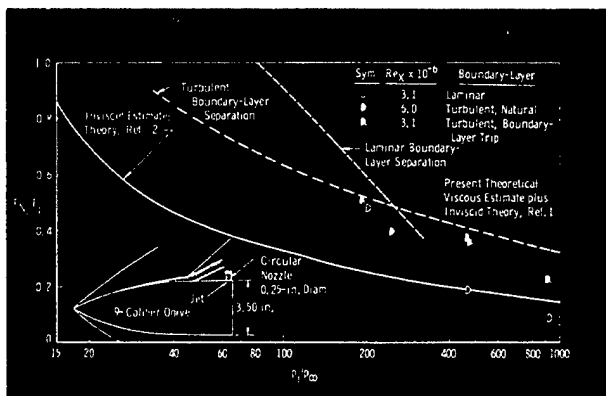


Fig. 4 Circular Jet Effectiveness on a Body of Revolution, $M_\infty = 4.0$

For optimum performance, a single circular nozzle on a body of revolution should be located near the model base, because the loading tends to propagate to the lee side of the body and reduces the resultant jet control force. The effect of body curvature and the character of the boundary layer approaching the jet on the loading produced by a single circular jet located at the model base was theoretically estimated and found to be in agreement with the experimental data, as indicated in Fig. 4. Theoretically, on a planar surface at all jet pressure ratios, the interaction force resulting from laminar boundary-layer separation is larger, but because of the transverse curvature of a body of revolution at the higher jet pressure ratios, the interaction force produced from turbulent separation becomes larger, as shown in Fig. 4.

In the application of lateral jets to produce control forces not only above but within the flight corridor, a jet operating at a fixed jet stagnation pressure on a vehicle flying at the same Mach number at various altitudes should produce control

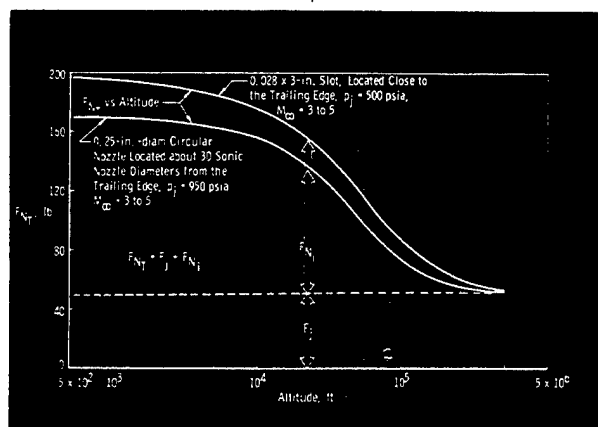


Fig. 5 Comparison of Resultant Force Produced by a Lateral Jet from a Circular Sonic Nozzle and a Slot at Various Altitudes

forces which increase as the altitude decreases in the manner shown in Fig. 5. As may be noted, significant interaction forces can be obtained at altitudes below about 100,000 ft for the configurations selected.

REFERENCES

1. Strike, W. T., Schueler, C. J., and Deitering, S. "Interactions Produced by Sonic Lateral Jets Located on Surfaces in a Supersonic Stream." AEDC-TDR-63-22, April 1963.
2. Ferrari, Carlo. "Interference between a Jet Issuing Laterally from a Body and the Enveloping Supersonic Stream." Johns Hopkins University, Bumblebee Series Rpt No. 286, AD-226-477, April 1959.
3. Vinson, P.W., Amick, J. L., and Liepman, H. P. "Interaction Effects Produced by a Jet Exhausting Laterally near Base of Ogive-Cylinder Model in Supersonic Main Stream." NASA Memo 12-5-58W, February 1959.

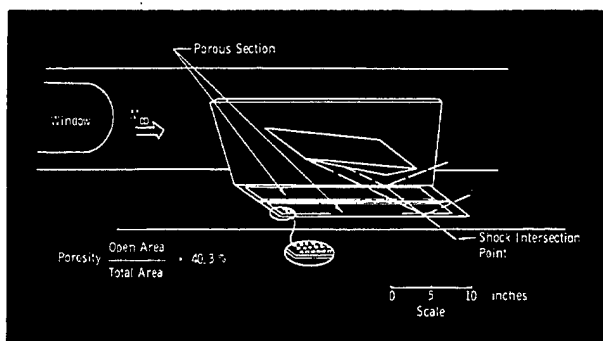


Fig. 1 Model Configuration

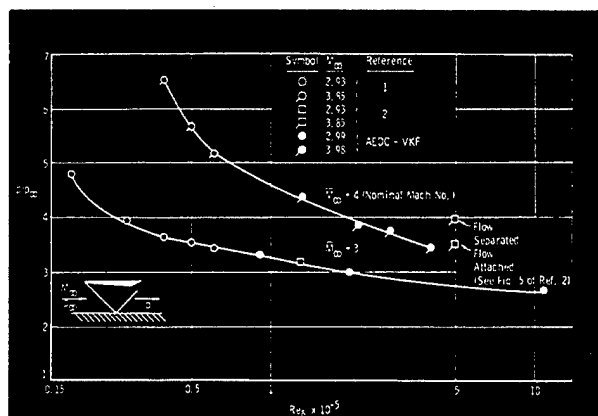


Fig. 2 Variation of the Incipient Separation Pressure Ratio with Free-Stream Reynolds Number

BOUNDARY-LAYER CONTROL AT SUPERSONIC SPEEDS

Boundary-layer suction has been extensively investigated as a method of boundary-layer control. The effect of suction is to stabilize the laminar boundary layer and thus delay the onset of transition. This results in less laminar friction and hence a reduction in overall drag.

Moreover, removal of fluid from the boundary layer produces new boundary layers which are capable of supporting larger adverse pressure gradients. In this way, boundary-layer separations which would have otherwise occurred may be reduced.

The VKF studies of laminar flow control and flow separation control by means of suction are described in the two following notes.

INFLUENCE OF SUCTION ON TURBULENT BOUNDARY-LAYER SEPARATION*

By

W. T. Strike, Jr.

This summary pertains to some experimental results relating to turbulent boundary-layer separation produced by an abrupt adverse pressure gradient ($dp/dx > 0$) generated by an oblique shock. A movable sharp wedge mounted above the tunnel floor (Fig. 1, page 32) was used to generate incident shocks of various strengths on the tunnel floor plate. In the second phase of the program, a porous floor plate was used so that suction could be applied to the boundary layer in the region of the hypothetical tunnel floor shock impingement point (Fig. 1).

These results were obtained over a Reynolds number range based on the boundary-layer thickness, Re_δ , of from 0.85×10^5 to 11.0×10^5 and are summarized in Fig. 2 (page 32) along with similar results published in Refs. 1 and 2. The region of separated boundary layer which extends upstream of the hypothetical shock impingement point will usually produce an additional inflection in the surface pressure distribution generated by the oblique compression wave. In this analysis, as was the case in Ref. 2, it was assumed that the absence of this inflection was an indication that the boundary layer was attached or that the region of separation was insignificantly small. Thus, the results in Fig. 2 represent the maximum Reynolds number and the corresponding peak plateau pressure ratio achieved in the absence of the aforementioned inflection in the pressure distribution. Although the boundary layer thickness varied from 0.1 to 2 inches, the data correlated reasonably well.

*This research was initiated and directed by P. Kutschenreuter, Flight Dynamics Laboratory, ASD, AFSC, which also supplied the test model equipment.

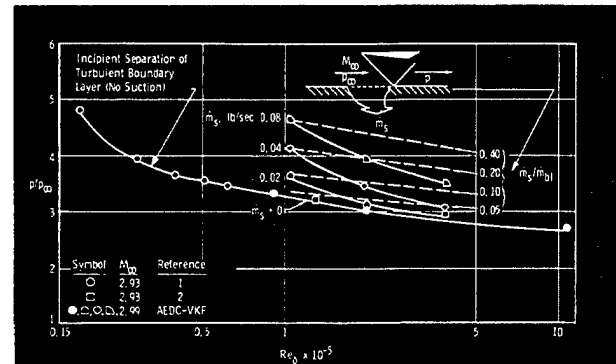


Fig. 3 Effect of Suction on the Maximum Reynolds Number and Pressure Ratio for Attached Flow

The effectiveness of boundary-layer suction in delaying separation at Mach number 3 is presented in Fig. 3 along with the previously experimentally defined limiting values for attached (or nearly attached) turbulent boundary-layer flow without suction. These suction results consisted of a set of experimentally determined lines of constant percentage of boundary-layer suction (m_s/m_{b0}) which vary in a manner similar to lines of constant suction rates. The values m_s/m_{b0} represent the ratio of bleed rates (m_s) to the boundary-layer mass flow (m_{b0}) in the model test area without suction.

It may be noted that suction ahead of the intersection of the oblique shock with a turbulent boundary layer delayed separation. For example, with a pressure rise to a level of $p/p_\infty = 4$ without suction, boundary-layer separation occurred at $Re_\delta \approx 0.27 \times 10^5$, but with suction this same pressure ratio of 4 was achieved in the absence of any significant boundary-layer separation at Re_δ up to about 4×10^5 with about 40 percent of the boundary layer removed.

Although not shown, larger amounts of suction nearly equal to the boundary-layer mass flow (m_{bl}) were required to reach the theoretical inviscid pressure rise when the suction was applied downstream and/or in the area of an oblique shock boundary-layer interaction region.

A more detailed discussion of these results and the method of analysis and assumptions used to obtain them are presented in Ref. 3. Included in Ref. 4 are experimental and theoretical results and a discussion of their limitations.

REFERENCES

1. Kuehn, Donald M. "Experimental Investigation of the Pressure Rise Required for the Incipient Separation of Turbulent Boundary Layers in Two Dimensional Supersonic Flow." NACA Memo 1-21-59A, February 1959.
2. Bogdonoff, Seymour M. "Some Experimental Studies of the Separation of Supersonic Turbulent Boundary Layers." Papers presented at the Heat Transfer and Fluid Mechanics Institute, Univ. of California at Los Angeles, June 23, 25, 1955, Sec. V, pp. 1-23.
3. Strike, W. T. and Rippey, J. "Influence of Suction on the Interaction of an Oblique Shock with a Turbulent Boundary Layer at Mach Number 3." AEDC-TN-61-129, October 1961.
4. Kutschenreuter, P. H., Zurschmeide, R. L., and Surber, L. E. "An Investigation of Shock Wave-Boundary Layer Interaction with Suction (Interim Report)." ASRMDF TM-61-30, January 1962.
5. boundary-layer transition measurements on a series of wings at various spanwise stations; sweep angles, $\Lambda = 24$ to 50 deg; $M_\infty = 2.5, 3, 4$, and 5; $\alpha = 0$ and ~ -4 deg
6. 72.5-deg swept wing with a subsonic leading edge; $M_\infty = 2$ and 2.25, $\alpha = 0.15, 0.45$, and 0.75 deg

LAMINAR FLOW CONTROL*

By

C. J. Schueler and S. R. Pate

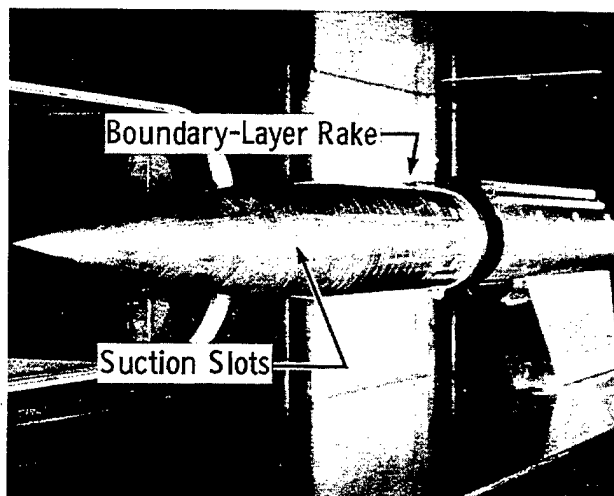
Following the achievement at high subsonic speeds of laminar flow at high length Reynolds numbers by the use of distributed suction, an experimental program at supersonic speeds was begun by NORAIR in 1957. Since these early tests, in 1957-1959, all of the NORAIR test programs on laminar flow control at supersonic speeds have been conducted in the VKF. These test programs have been in progress from early 1959 to the present date and have included the following tests:

1. 20-caliber ogive cylinder body of revolution, $M_\infty = 2.5, 3, 3.5$, and 4
2. flat plate, $M_\infty = 2.5, 3, 3.5$, and 4
3. flat plate with impinging shocks, $M_\infty = 2.5, 3$, and 3.5; shock generator at 0 to 4 deg
4. 36-deg swept wing with a supersonic leading edge, $M_\infty = 2.5, 3, 3.5$, and 4; angle of attack, $\alpha = 0$ and -3.25 deg

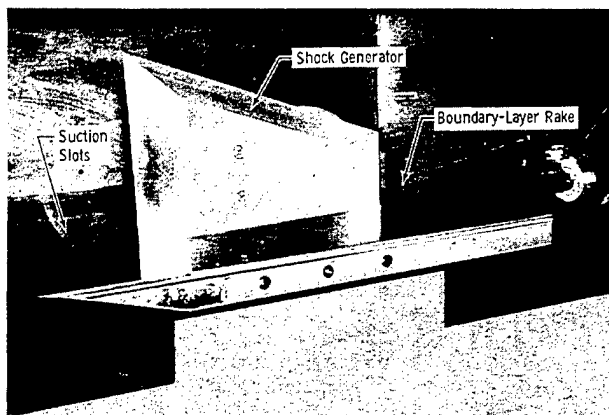
The models were designed and constructed by NORAIR and had a series of slots, ranging in size from approximately 0.003 to 0.014 in. in width, through which a portion of the boundary layer was removed. In general, the mass of air removed by the slots corresponded to a layer adjacent to the surface having a height equal to slightly less than the slot width. Air removed from the boundary layer passed into segmented model compartments and to flow-metering valves and flowmeters. Examples of the typical models that have been tested are shown in Fig. 1.

The effectiveness of laminar flow control was evaluated by measurements of the boundary-layer characteristics and air removal flow rates, which may be expressed together in terms of a total drag coefficient, C_{DT} . For the results presented, the total drag coefficient is represented by the wake drag coefficient and the equivalent suction drag coefficient required to accelerate the air removed to flight speeds. Since the wake drag decreases and the suction drag increases with increased suction rate, an optimum total drag value exists which is used to evaluate the net effectiveness of laminar flow control.

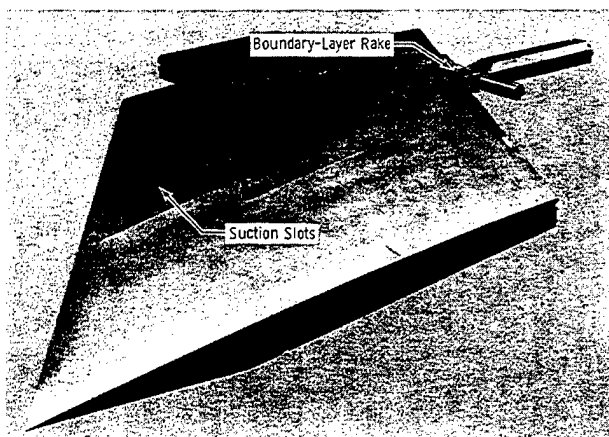
*The research described in part in this note is the experimental phase that was performed primarily under the direction of Dr. E. Groth, Northrop Corporation, NORAIR Division for the Flight Dynamics Laboratory, Aeronautical Systems Division. The work was conceived by the NORAIR Boundary Layer Research Group under the direction of Dr. W. Pfenninger, U.S. Air Force Contract AF 33(616)-3168.



a. Ogive Cylinder, AEDC-VKF 12-in. Supersonic Tunnel (D)



b. Flat Plate, AEDC-VKF 40-in. Supersonic Tunnel (A)



c. 36-deg Swept Wing

Fig. 1 Typical Models

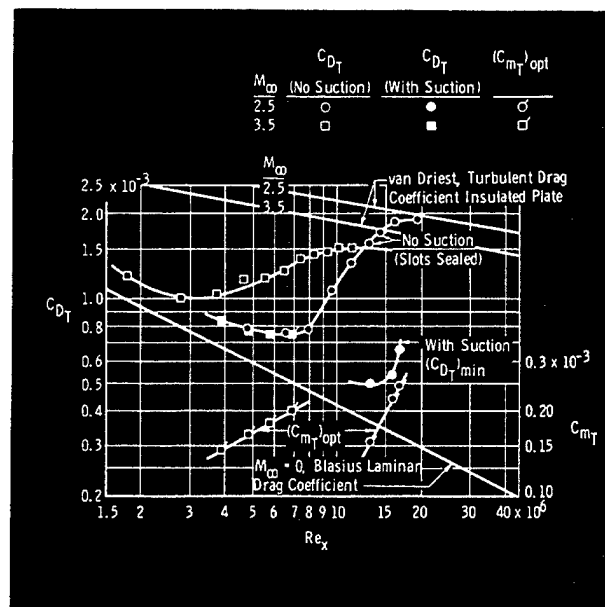


Fig. 2 Drag Coefficients at Station 18.8 in., with and without Suction, Ogive Cylinder, 3.25-in. Diameter

Typical results of suction and drag measurements on a 20-caliber ogive cylinder are presented in Fig. 2 for Mach numbers 2.5 and 3.5. The effectiveness of suction may be noted by the comparison of the Reynolds numbers where transition began moving forward. For example, at Mach number 3.5, transition occurred at a length Reynolds number, Re_x , of $\approx 3 \times 10^6$ with no suction, and with suction laminar flow was maintained at Reynolds numbers up to about 7×10^6 . The reductions in drag that are possible may be noted by a comparison of the total drag coefficients, C_{DT} , for no suction and the minimum total drag coefficients, $(C_{DT})_{min}$, with optimum suction at the various Reynolds numbers. The optimum total suction coefficients, C_{MT} , and the manner in which they must vary to maintain laminar flow with increasing Reynolds number are also shown.

Typical total drag coefficients, C_{DT} , and the corresponding optimum total suction coefficients for a flat plate are presented in Fig. 3 for Mach numbers 3 and 4. Reductions in drag amounting to about 75 percent at $M_\infty = 3$ and to 30 percent at $M_\infty = 4$ may be noted. Of interest is the low reduction in drag obtained at $M_\infty = 4$, which may be attributed to operation of the suction system at an off design condition.

In actual application of laminar flow control to a supersonic vehicle, shock waves will be present in the region of the suction slots because of adjacent vehicle components. The influence of shock impingement was investigated with a flat plate model which had a shock generator that would produce a compression wave across the suction slots (Fig. 1b). As is evident in the results shown in Fig. 4, laminar

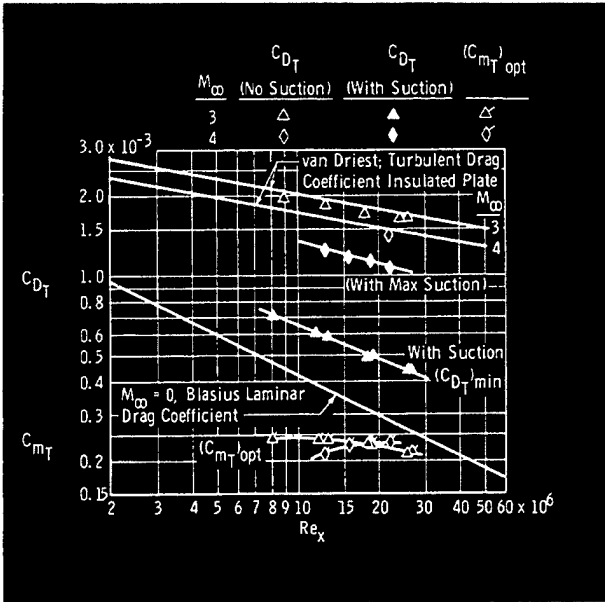


Fig. 3 Drag Coefficients at Station 40.2 in., with and without Suction, Flat Plate

flow was maintained behind the shock for generator angles up to 1 deg at $M_\infty = 2.5$ to 3.5 without an appreciable increase in the wake drag coefficient, C_{D_W} . Laminar flow could be maintained at $M_\infty = 2.5$ at shock generator angles up to 2 deg, and increases in Mach number reduced the shock strength at which an increase in wake drag began to occur.

Location of the initial suction slots is critical with regard to the location of natural transition. The forward suction slots must be located ahead of natural boundary-layer transition where disturbances in the laminar boundary layer have not amplified to a point where suction can no longer control their continued growth, which ultimately will produce transition to turbulent flow. This is indicated by the results of tests of a 36-deg swept wing at $M_\infty = 3$, with the first suction slot

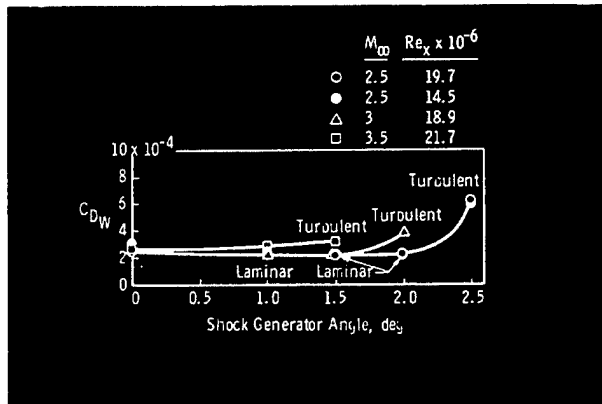


Fig. 4 Change in Wake Drag Coefficient with Shock Generator Angle

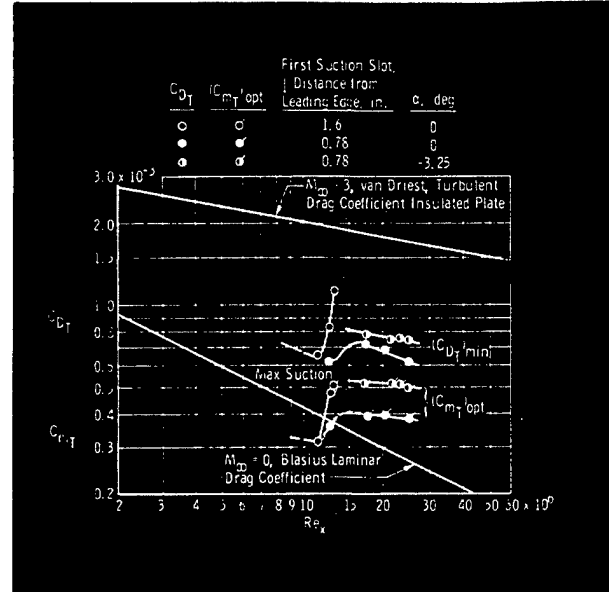


Fig. 5 Minimum Total Drag Coefficients and Optimum Suction Coefficients on Swept Wing at $M_\infty = 3$, Rake at Station 37.9 in.

1.6 in. from the leading edge. The results (Fig. 5) show that laminar flow could only be maintained up to a Reynolds number of about 11×10^6 . Additional slots were added so that the first slot was 0.78 in. from the leading edge, and the width was increased in order to promote early stability of the boundary layer. With this modification, low drag was achieved at Reynolds numbers up to 25×10^6 . Pitching the wing to a -3.25 -deg angle of attack (α) increased the total drag because of the increased suction required to maintain laminar flow.

To obtain basic data on the manner in which transition varies with sweep angle, Λ , tests were conducted on a series of swept wings where beginning of transition locations were measured at Mach numbers 2.5, 3, 4, and 5. These results are shown in Fig. 6 at $M_\infty = 3$ with a theoretical estimate of the variation with sweep angle.

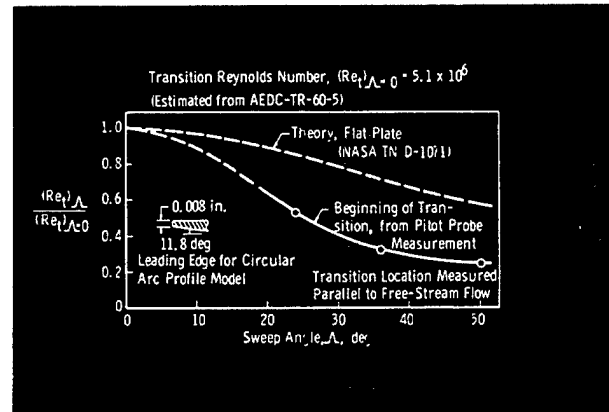


Fig. 6 Variation of Transition with Sweep at $M_\infty = 3$, $Re/in. = 0.80 \times 10^6$, $\alpha = 0$

The studies here mentioned have been reported in detail in the following publications:

W. T. Strike and J. C. Donaldson. "Investigation of Suction Controlled Boundary Layer on a Northrop Model at Mach Numbers of 2.5, 3.0, and 3.5." AEDC-TN-59-80, July 1959.

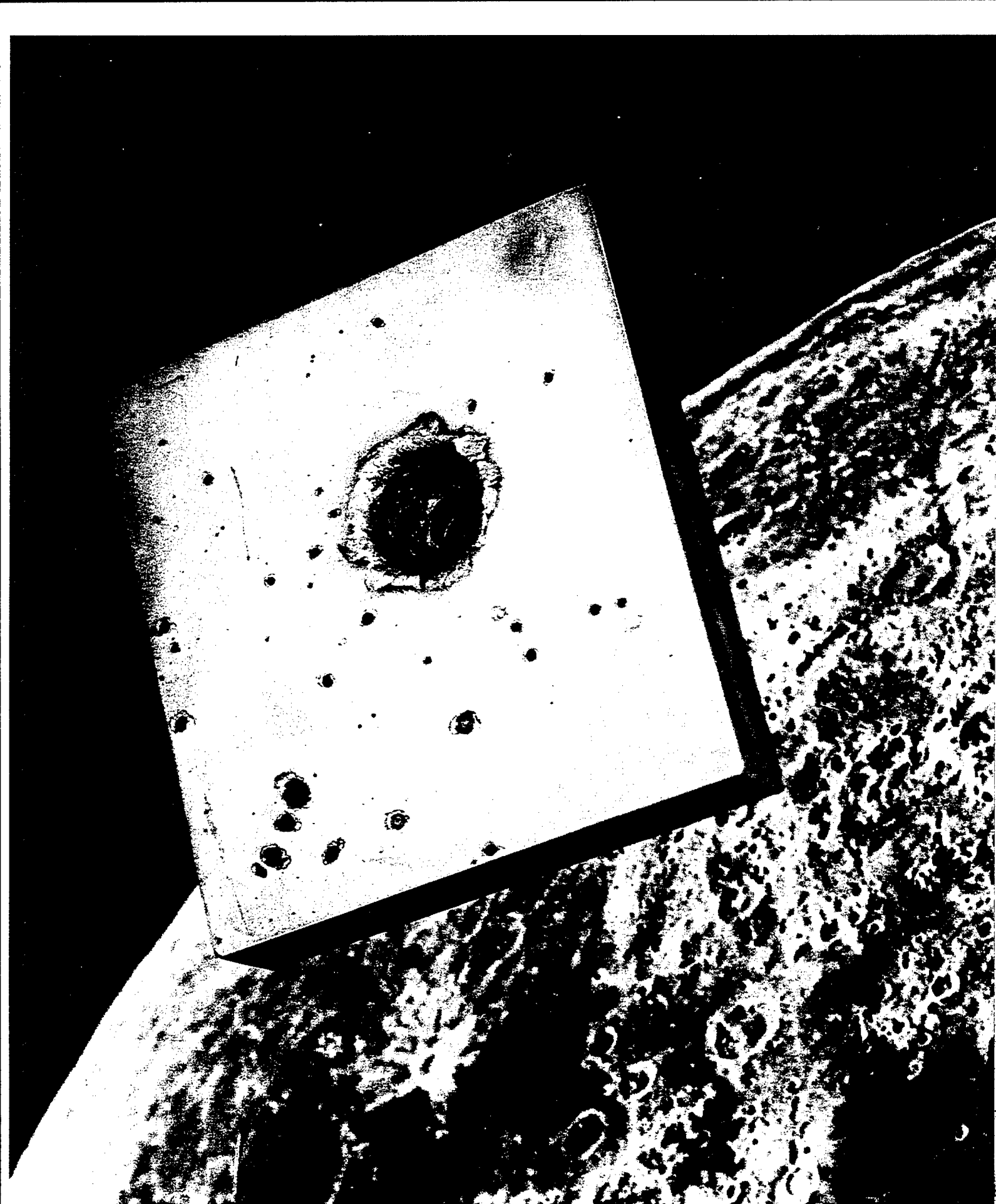
W. T. Strike and S. R. Pate. "Investigation of Boundary-Layer Suction on a 20-Caliber Ogive Cylinder at Mach Numbers 2.5, 3.0, 3.5, and 4.0." AEDC-TN-61-66, June 1961.

J. H. Jones and S. R. Pate. "Investigation of Boundary-Layer Suction on a Flat Plate at Mach Number 3." AEDC-TN-61-128, September 1961.

S. R. Pate and J. S. Deitering. "Investigation of Drag Reduction by Boundary-Layer Suction on a Flat Plate and a 36-deg Swept Wing at Supersonic Speeds." AEDC-TDR-62-144, August 1962.

S. R. Pate and J. S. Deitering. "Investigation of Drag Reduction by Boundary-Layer Suction on a 36-deg Swept Wing at $M_\infty = 2.5$ to 4." AEDC-TDR-63-23, January 1963.

S. R. Pate and R. E. Brillhart. "Investigation of Boundary-Layer Transition on Swept Wings at Mach Numbers 2.5 to 5." AEDC-TDR-63-109, July 1963.



There is striking similarity in the appearance of lunar and man-made craters: the crater seen here resulted from impacting an aluminum target with a copper projectile at 18500 ft/sec.

HYPERVELOCITY IMPACT

During the past two years, two aspects of hypervelocity impact phenomena have received particular attention in the VKF: the formation of craters in semi-infinite targets and the mechanism of wave propagation and spall formation. Experimental data have been obtained at velocities up to 8.82 km/sec (29 kft/sec).

FORMATION OF CRATERS

By

E. H. Goodman

EXPERIMENTAL TECHNIQUE

The hypervelocity impact range in which the tests have been conducted, shown in Fig. 1, consists of: (1) a two-stage launcher (2) an expansion tank to absorb muzzle blast and to provide space for separation of the projectile from the sabot (3) a connecting tube which had provision for measuring projectile velocity, and (4) a test chamber. A description of the range and launcher is given in Ref. 1.

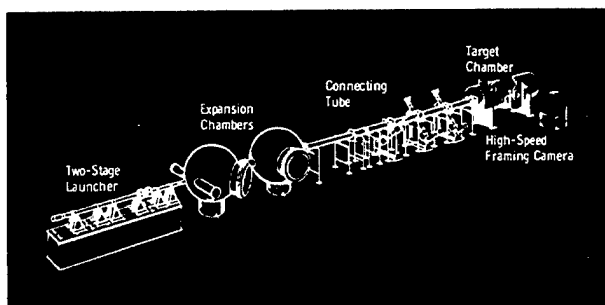


Fig. 1 Typical Hypervelocity Impact Range

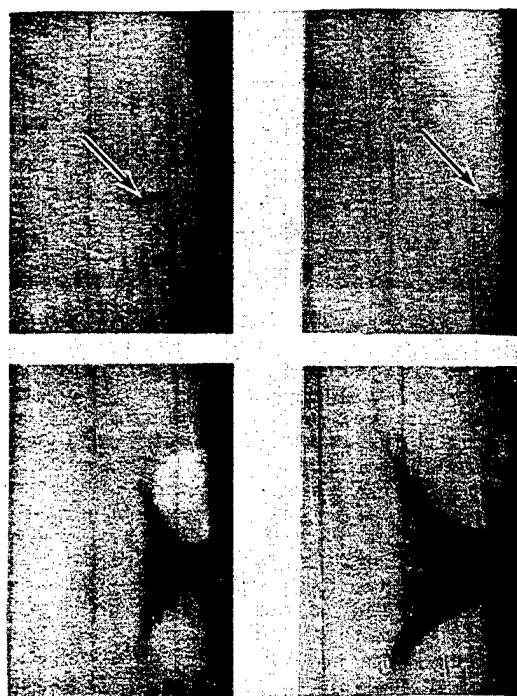
Spherical aluminum, copper, and stainless steel projectiles, ranging in diameters from 1.59 to 6.35 mm, have been impacted on thick aluminum and copper targets (Ref. 2). The spherical projectiles had to be launched with plastic sabots, and in order to obtain clean impacts, a mechanical sabot stripper was developed. The reliability of the stripper was on the order of 70 percent.

The velocity and structural integrity of the projectile just before its arrival at the target were recorded by a high-speed framing camera (1.4×10^6 frames per second maximum rate). Fiducial lines accurately spaced on a translucent screen, against which the projectile was silhouetted, allowed the projectile's position to be computed and the velocity at impact determined by computer programming for a least squares fit. Figure 2 is typical of a series of frames showing the projectile and target.

Crater volume, which is defined as the volume below the original target surface, was determined by accurately metering a solution into the crater. The crater diameter was measured by traversing the vernier table from a point on the crater wall at

solution level (as observed with a cathetometer) to a point where the cross-hair of the cathetometer was tangent to the opposite side of the crater at the solution level. Hence, the distance through which the vernier table traveled was equal to the crater diameter at the solution level. The target was then rotated approximately 90 deg, and the measurement was made again. The average of several readings was taken as the crater diameter. Crater depth was determined using an optical depth micrometer.

A detailed description of these procedures is given in Ref. 1.



Flight and Impact of a 3.18-mm-diam Aluminum Sphere into an Aluminum Target at a Velocity of 6.5 km/sec

Fig. 2 Four Frames from a Typical Framing Camera Sequence Showing Projectile, Target, and Spall Formation

HYPERVELOCITY IMPACT

PENETRATION

Typical penetration data are presented in dimensionless form in Fig. 3, in terms of P/d vs u_p/c , where P = crater depth (from the original target surface), d = projectile diameter, u_p = impact velocity, and c = velocity of sound in the target material (u_p/c = impact Mach number). The experimental results are compared with the Ames penetration formula (Ref. 3):

$$P/d = K_1(\rho_p/\rho_t)^n (u_p/c)^m$$

where ρ_p = projectile density, ρ_t = target density, and K_1 , n , and m are empirical constants. For the data presented the constants were found to be $K_1 = 2.35$, $n = 0.7$, and $m = 0.667$.

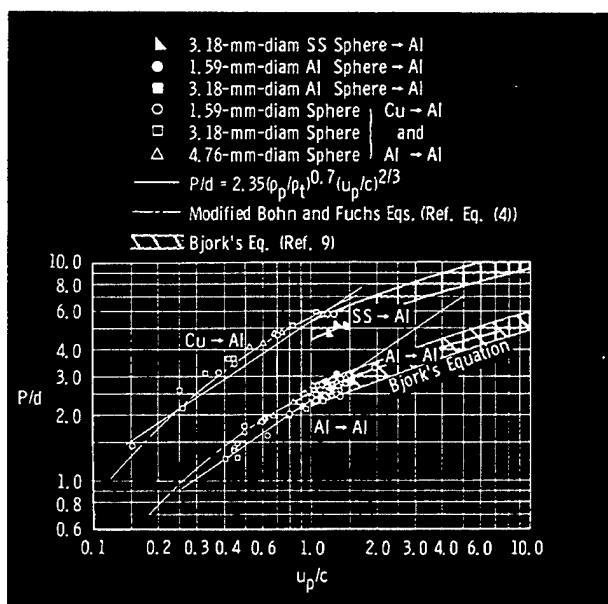


Fig. 3 Correlation of Penetration Results

Correlation with other empirical expressions involving projectile momentum, target hardness, and velocity of sound of the projectile material were also attempted but were found to be inadequate. These expressions are derived and discussed in Ref. 5.

Several theoretical analyses are presently available. In general, they may be divided into four groups: (1) rigid projectile, (2) hydrodynamic model, (3) thermal penetration, and (4) explosive analogy. The experimental data and pertinent theories of each group were compared, but adequate correlations could not be obtained in most cases. A theoretical formula was derived by Bohn and Fuchs (Ref. 6) based on low velocity penetration considerations but was considered by them to be applicable to meteoroid impact. For spherical projectiles, the formula is as follows:

$$P/d = (2\rho_p/\rho_t)^n \left\{ \ln[1 + (B/3)^{1/2}] - [(B/3)^{1/2}]/[1 + (B/3)^{1/2}] \right\}$$

where

$$B = \rho_t u_p^2 / H \text{ (Best number, Ref. 4)}$$

H = Brinell hardness

and

$$n = 1$$

It was found that if n is taken as $2/3$, a reasonably good fit for all of the aluminum and copper target-projectile combinations is obtained (Fig. 3). Correlation with Bjork's theoretical model (Ref. 7) is also shown in Fig. 3.

CRATER SHAPE

Several of the empirical expressions and theoretical analyses (Ref. 5) use the simplifying assumption that the crater is hemispherical ($P/D_c = 0.5$). Figure 4 shows the parameter P/D_c versus projectile velocity. The craters from all of the projectile-target combinations approach a hemispherical shape as the velocity increases. Within the range of velocities obtained, craters in aluminum which were made by copper projectiles and craters in aluminum which were made by stainless steel projectiles were deeper than hemispherical. Craters resulting from aluminum into aluminum and copper into copper impacts were essentially hemispherical at the higher velocities. Aluminum into copper craters approached a hemispherical shape as the velocity increased, but more data will be needed in the higher velocity range to confirm their shape.

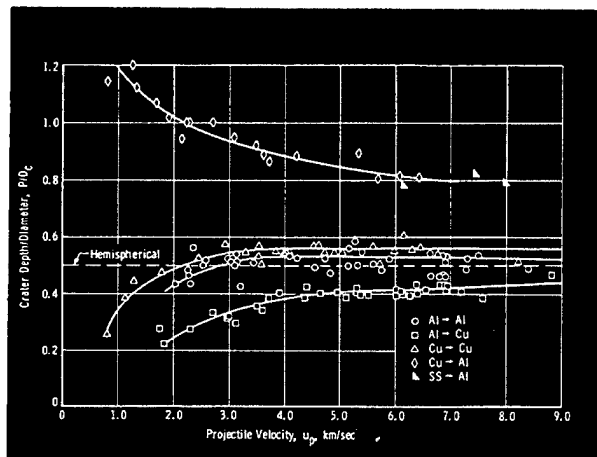


Fig. 4 Crater Depth to Diameter Ratio for Copper and Aluminum Spheres into Copper and Aluminum Targets

CRATER VOLUME

Crater volume data are shown in Fig. 5 in the dimensionless form, V_c/V_p versus u_p/c , where V_c = crater volume and V_p = projectile volume. Correlation of the data with the equation

$$V_c/V_p = K_2(\rho_p/\rho_t)^{3/2} (u_p/c)^2$$

is also shown, with $K_2 = 44.1$ empirically derived.

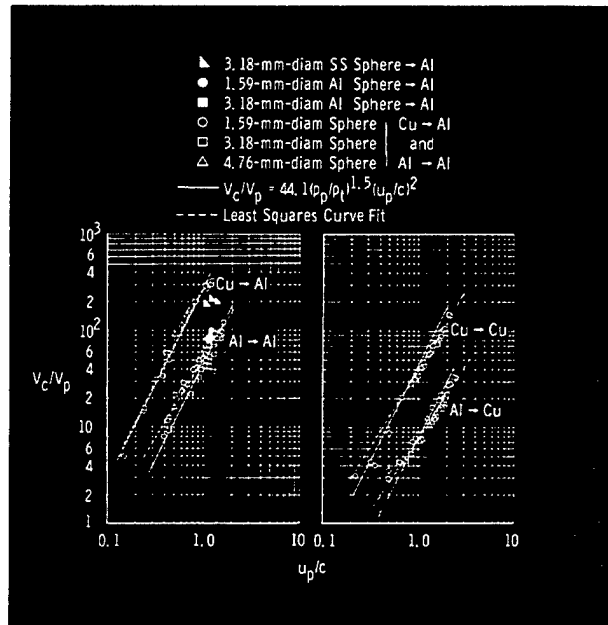


Fig. 5 Correlation of Crater Volume Data with Empirical Volume Prediction Equations

REFERENCES

1. Goodman, E. H. "Description of Terminal Ballistics Ranges." AEDC-TDR-62-104, May 1962.
2. Liles, C. D. and Goodman, E. H. "Particle-Solid Impact Phenomena." AEDC-TDR-62-202, November 1962.
3. Charters, A. C. and Locke, G. S., Jr. "A Preliminary Investigation of High Speed Impact: The Penetration of Small Spheres into Thick Copper Targets." NACA-RM-A58B26, May 1958.
4. Summers, J. L. "Investigation of High Speed Impact: Regions of Impact and Impact at Oblique Angles." NASA-TN-D-94, October 1959.
5. Herrman, Walter and Jones, A. H. "Survey of Hypervelocity Impact Information." ASRL Report No. R-99-1 (AD-267-290), October 1961.
6. Bohn, J. L. and Fuchs, O. P. "High Velocity Impact Studies Directed Toward the Determination of Spatial Density, Mass, and Velocity of Micrometeorites at High Altitudes." Temple University Scientific Report No. 1, January 1958.
7. Olshaker, A. E. and Bjork, R. L. "Hydrodynamics Applied to Hypervelocity Impact II. The Role of Melting and Vaporization in Hypervelocity." Proceedings of the Fifth Symposium on Hypervelocity Impact, Vol. 1, Part 1, April 1962.

TARGET REAR SURFACE FRACTURE RESULTING FROM HIGH-SPEED IMPACT

By

R. Kinslow*

What happens when two bodies collide at extremely high speed? In the past, the incentive to study the effects of high-speed impact arose from the military need of armor plate to withstand projectiles at speeds up to about 4,000 ft/sec (2,700 mph). The incentive now has changed. Meteoroids and man-made fragments pose a potential hazard to missiles and space vehicles, and methods of protection against catastrophic damage on impact have to be developed. The speeds of the interplanetary debris are estimated to average about 50,000 ft/sec and to go as high as 200,000 ft/sec (140,000 mph). More must be learned of the physical laws that apply at these extremely high velocities. For example, when a steel ball strikes a copper target at 30,000 ft/sec, the pressure is greater than 40 million psi. Little is known about the properties of metals under these conditions.

* Consultant to VKF, ARO, Inc., Chairman, Department of Engineering Science, Tennessee Polytechnic Institute.

Although the velocities obtained in the ranges of the von Kármán Gas Dynamics Facility are among the highest attainable at the present time, they are far below the average meteoroid velocity. As it is not possible to determine the effects of meteoroid impacts by experimental methods except at low velocities, an understanding of the mechanism involved in this phenomenon is necessary. Both empirical and theoretical studies are being made in the VKF (Ref. 1), and it is believed that they are adding to an understanding of the physical nature of hypervelocity impact. This knowledge will be of utmost value to the designer of missiles and space vehicles.

When a solid body is impacted by a hypervelocity projectile, the kinetic energy of the projectile is partitioned among several physical effects, such as permanent deformations; heat, light, and vaporization; ejection of most of the projectile and some of the target material; and shock waves. A simplified description of the effect may be divided into several stages:

(1) the projectile is imbedded in the target material; (2) the crater expands very rapidly, the motion resembling an explosion; (3) the velocity of the crater surface decreases, thereby permitting a shock to become detached from its surface. Material flowing along the wall of the crater is ejected at velocities up to several times the impacting velocity of the projectile. (4) Permanent deformation ceases and the shock decays into a spherical elastic stress wave which continues to dissipate energy throughout the target. (5) The wave reflects from the back or other free surfaces of the target as a tensile wave that produces secondary fractures and deformations if the tensile stress exceeds the fracture stress of the target material. This fracture stress is much greater than the static ultimate stress.

The principal source of danger from a meteoroid which does not actually pierce the wall of a spacecraft results from the damage produced by the stress waves reflected from free surfaces. A tensile wave reflected from the rear surface of a target may produce damage at or near the rear face as a granular fracture at the surface, as internal cracks and bulging of the surface, or as a detachment of the target material as shown in Figure 1. Although no actual deformation of the rear surface of the target occurs, other damage might result in some instances. For example, if this portion of the spacecraft contained a liquid, the stress wave could be transmitted through the liquid and perhaps focused at some distant point so as to produce disastrous results. Studies relating to shock propagation are now underway at the VKF.

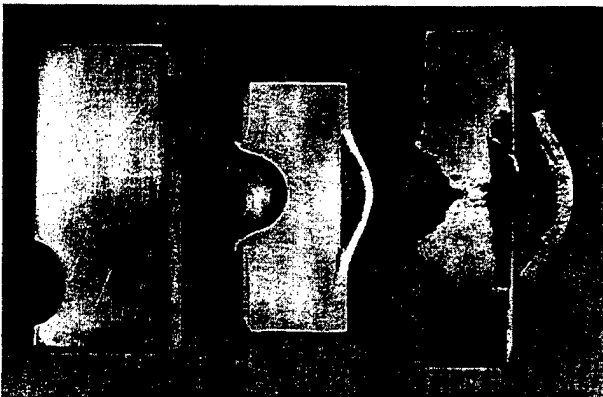


Fig. 1 Fractures Produced by Reflected Shock Waves

Much information concerning the nature of fracture and stress waves is being gained by the use of transparent targets. Figure 2 shows a series of photographs of a Lucite target being impacted by a hypervelocity projectile. (The camera used is capable of taking pictures at a rate up to 1.4 million frames per second.)

Studies indicate that the shock front just following impact has a velocity about

equal to the velocity of the impacting projectile. As the crater is being formed, the shock separates from its surface. Its strength rapidly attenuates, and its velocity decreases in a very short time to the velocity of an elastic wave.

In the past, the propagation of spherical elastic waves in solid media has been the object of much study among seismologists. The approach has been to consider an infinite homogeneous medium in which there exists a hollow spherical cavity within which there is an explosion producing a time-varying pressure. The problem has been to determine the wave motion and pressures in the surrounding solid medium. The problem of hypervelocity impact of a projectile into a semi-infinite solid is a similar one. When a charge is fired within a hollow cavity, or when a high-speed projectile impacts a solid, a wave is generated in which the pressure is much greater than the material strength. This wave diverges from the point of impact, or site of the explosion, crushing the material. The wave rapidly attenuates because of loss of energy. At some distance within the solid the pressure will equal the strength of the material, and at greater distances the material will be elastic if viscosity and internal friction are neglected. This critical distance is called the "radius of the equivalent cavity." There is evidence, both theoretical and experimental, that this radius is about equal to the final crater depth caused by the impact. This is not to say that an elastic wave detaches itself from the crater, but rather that the shock decays into an elastic stress wave at about this location before the cavity is completely formed.

Spherical, longitudinal wave propagation in a homogeneous, isotropic material can be specified by the wave equation

$$\frac{\partial^2 \phi}{\partial t^2} = c^2 \nabla^2 \phi$$

where ϕ is a scalar displacement potential, c is the wave velocity, and t is time. The particle displacement and velocity are specified by the relations

$$u = \frac{\partial \phi}{\partial r} \quad \text{and} \quad v = \frac{\partial u}{\partial t}$$

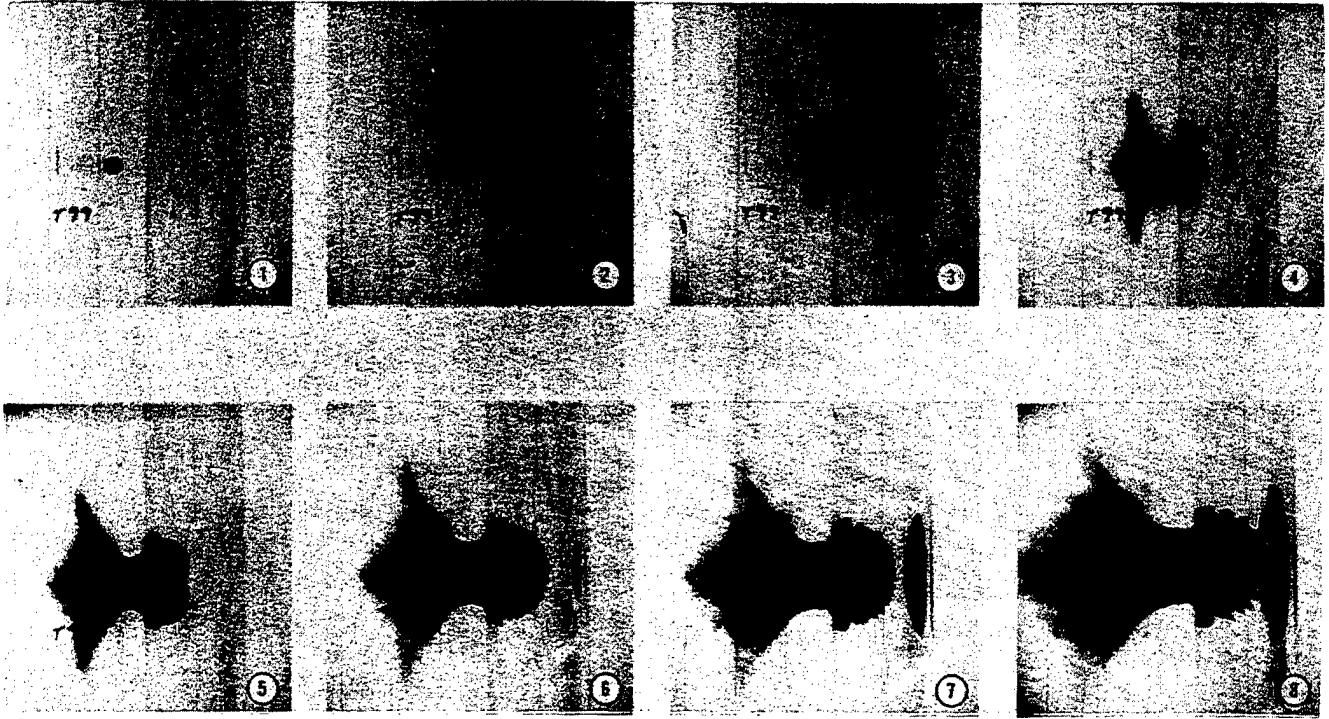
If r denotes the radius vector from the point of projectile impact, the principal stresses are given by the relations

$$\sigma_r = (\lambda + 2\mu) \frac{\partial u}{\partial r} + 2\lambda \left(\frac{u}{r} \right)$$

$$\sigma_\theta = \lambda \left(\frac{\partial u}{\partial r} \right) + 2(\lambda + \mu) \left(\frac{u}{r} \right)$$

where λ and μ are the Lamé constants. The maximum shear stress is found to be

$$\sigma_s = \mu \left(\frac{\partial u}{\partial r} - \frac{u}{r} \right)$$



A test technique which enables the detailed observation of impact phenomena produced by a hypervelocity projectile has been developed in the von Kármán Gas Dynamics Facility. The above pictures show various stages of the projectile and back spall craters as follows: (1) plastic projectile approaching Plexiglas target at 21,800 fps, (2) impact of projectile, (3, 4, and 5) development of projectile's crater and transit of shock wave through the target, (6) reflection of shock wave and formation of back spall crater, and (7 and 8) latter stages of crater formations.

Fig. 2 Observations of Hypervelocity Impact in Plexiglas Target

and the mean pressure acting at a point is

$$\sigma_m = \left(\lambda + \frac{2}{3} \mu \right) \left(\frac{\partial u}{\partial r} + \frac{2u}{r} \right)$$

If the pressure applied within the spherical cavity having a radius r_1 is assumed to be an impulse described by the relation

$$p = p_1 \sum_{i=1}^n K_i e^{-i\alpha t}$$

a solution of the wave equation is

$$\phi = \sum_{i=1}^n \frac{K_i p_1 r_1}{\rho r [\omega_0^2 + (\alpha_0 - i\alpha)^2]} \left\{ -e^{-i\alpha \tau} + e^{-\alpha_0 \tau} \left[1 + \left(\frac{\alpha_0 - i\alpha}{\omega_0} \right)^2 \right]^{1/2} \cos \left[\omega_0 \tau - \tan^{-1} \left(\frac{\alpha_0 - i\alpha}{\omega_0} \right) \right] \right\}$$

where

$$\tau = t - \left(\frac{r - r_1}{c} \right)$$

$$\alpha_0 = \frac{c}{r_1} \left(\frac{1 - 2\nu}{1 - \nu} \right)$$

$$\omega_0 = \frac{c}{r_1} \left[\frac{(1 - 2\nu)^{1/2}}{1 - \nu} \right]^{1/2}$$

and

ν = Poisson's ratio

The value of p_1 is dependent upon the impact pressure between projectile and target, the size of the projectile, and the depth of the crater produced. The area under the pressure-time curve is a function of the projectile momentum and crater depth. Figure 3 shows the pressure-time relations for various values of n .

It may be seen in Fig. 2 that fractures near the rear target surface are formed by the reflection of tensile stress waves. Once a fracture has been produced, the tail of the pulse is reflected from the new surface so that a series of parallel cracks

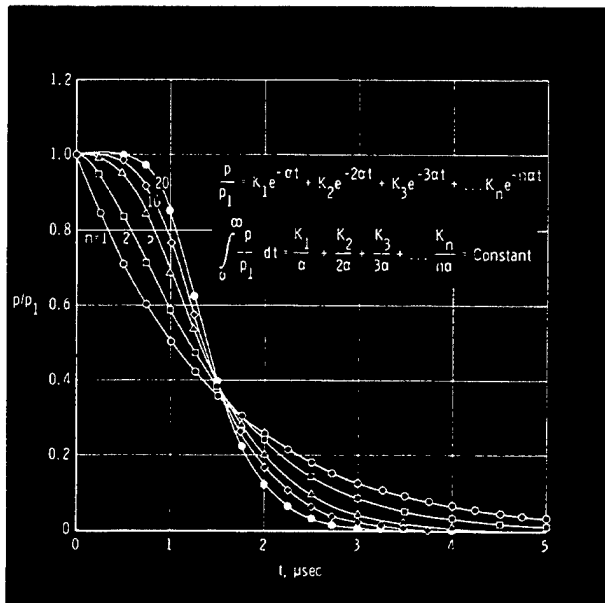


Fig. 3 Various Forcing Functions Having Same Momentum

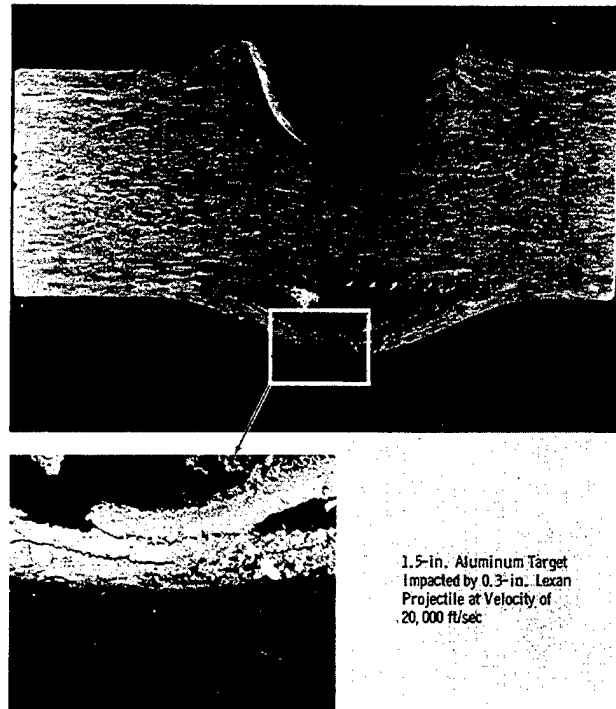


Fig. 4 Multiple Fractures near Rear Surface of Aluminum Target

may be formed as shown in Fig. 4. It was found that fractures would be produced in an aluminum target and would be located as those which are shown, if $n = 5$ and $\alpha = 3$ were taken for the forcing function. By observing the motion of the rear surface of the target during impact, the particle velocity was determined.

Figures 5 and 6 show the stresses produced by the pressure pulse as it moves through the aluminum target after impact by a plastic projectile having a velocity of 20,000 ft/sec. The numbers on each curve give the time, in microseconds, since the wave became elastic.

On the basis of this investigation, the following observations became apparent for aluminum targets:

1. Aluminum targets (99.99 percent pure) have a tensile strength of 100,000 psi under hypervelocity impact.
2. The forward component of the shock momentum is about equal to the momentum of the impacting projectile. By the use of a ballistic pendulum, it has been found that the total momentum imparted to aluminum targets by plastic projectiles approaches a value of two for higher velocities. This means that approximately 50 percent of the total momentum imparted to the target is in the pressure pulse.

3. The attenuation rate of the shock before it becomes an elastic wave is about twice that of an elastic wave.
4. The spall thickness (distance between first fracture and rear target surface) may either increase, decrease, or remain constant with an increase in target thickness for equal projectile masses and velocities, depending upon the target strength.
5. Spall thickness decreases with an increase in projectile velocity for targets of equal thickness.
6. Fractures are independent of projectile shape.

Work is now being conducted with solid targets of other materials and with laminated targets. Studies are being made concerning the effects of internal friction, viscosity, relaxation, and other properties of material; the effects of plastic waves, waves of distortion, and Rayleigh surface waves; and the validity of the various assumptions which have been made.

REFERENCE

1. Kinslow, Ray. "Properties of Spherical Stress Waves Produced by Hypervelocity Impact." AEDC-TDR-63-197, October 1963.

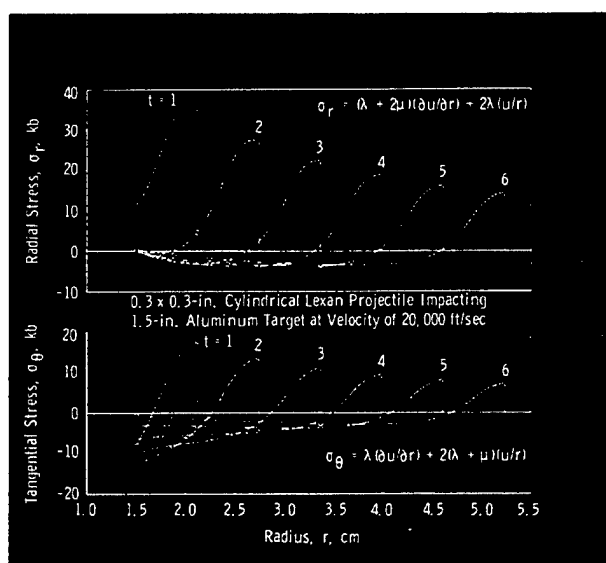


Fig. 5 Principal Stresses in Target as Functions of Radius and Time

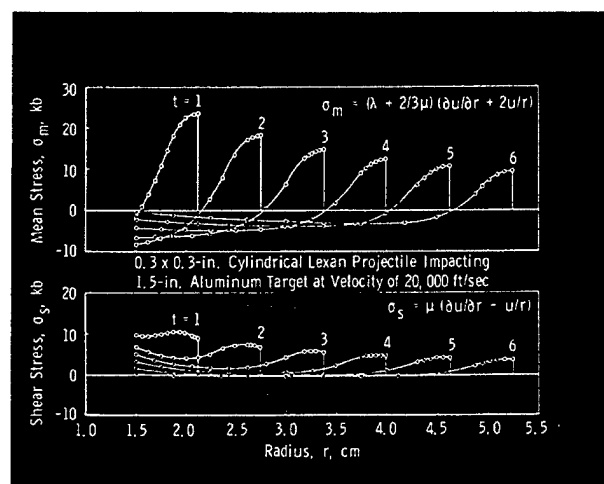


Fig. 6 Mean and Shear Stresses in Target as Functions of Radius and Time



A model is seen suspended in the VKF prototype, five-component, magnetic suspension system being developed for use with supersonic and low density tunnels.

EXPERIMENTAL TECHNIQUES

SUPERSONIC AND HYPERSONIC TUNNELS

Development of the 50-inch Mach 8 and 10 tunnels involved a number of significant and new departures in the wind tunnel technology. Simply machined, segmented, axisymmetric, contoured nozzles were found to produce good quality flow in the test section. With the activation of the 50-inch Mach 10 tunnel in 1961, we find the philosophy of wind tunnel design completely opposed to the one with which the development of relatively large supersonic wind tunnels started in Germany in the late nineteen twenties. In those days, for reasons of economy, the intermittent tunnel concept was introduced, tunnel runs of the order of a minute being obtained using vacuum storage. This basic technique, which was highly developed during the next 25 years, involved an intermittent test section flow and a model continuously present in the test section. In the VKF Mach 10, 50-inch tunnel, the opposite is true: the tunnel flow is continuously maintained while the model is intermittently injected for test.

Since, with the modern instrumentation, the data taking takes only a relatively short time, this mode of operation, by providing maximum model accessibility, insures highest tunnel utilization. Moreover, it eliminates the problem of model starting loads and allows convenient conduct of heat transfer tests.

In the contributions which follow these and other significant problems which were encountered in the design and operation of VKF large, continuous, supersonic and hypersonic wind tunnels are discussed.

DEVELOPMENT OF AIR HEATERS FOR CONTINUOUS, HYPERSONIC TUNNELS

By

R. M. James

1500°F AIR HEATER

The continuous hypersonic wind tunnels in VKF require elevated stagnation temperatures to prevent air liquefaction. Included in the initial facility equipment was a 12,000-kw electric resistance heater intended to supply heated air for a continuous hypersonic wind tunnel at stagnation temperatures up to 1500°F and stagnation pressures up to 2000 psi.

The heater consisted primarily of thirty sets of two concentric Nichrome tube elements mounted in tube sheets with insulators. This tube bundle was surrounded by a cylindrical steel shroud covered with insulation. The tube bundle-shroud assembly was contained in a cylindrical pressure vessel. The tubes were heated by passing electrical current through them, and the air was heated as it passed through the heated tubes.

Early operation of the heater proved that it would not give the required performance in the original condition. Many minor difficulties were identified and overcome; however, three major problem areas existed. These were air bypassing the heater elements, thermal distortion of the cylindrical shroud around the tube element bundle, and failure of electrical straps connecting the heating elements at the downstream end.

In the early runs, the maximum exit air temperature obtained was 900°F, using a maximum allowable tube temperature of 1900°F. Investigation showed that this resulted primarily from inlet air bypassing the heating elements. The air was leaking around the outside of the tubes and the outside of the shroud. The cooler bypass air mixed with the heated air leaving the tubes, resulting in a low temperature. The upstream end of the heater was redesigned to eliminate the bypass air, bringing the exit temperature up to the desired 1500°F. In this redesign, the seal around each tube element also acted as an anchor point to withstand the downstream thrust of the tube.

It was found that a positive temperature gradient from bottom to top of the heater was causing severe distortion of the shroud. The gradient produced a bow of several inches in the shroud with the high point at the center, crushing insulation and causing hot spots in the heater shell. The thermal gradient could not be eliminated easily; therefore, its effect was neutralized by cutting the shroud into four axial segments. The distortion of each segment was small enough to be tolerated.

The most difficult problem to solve was the failure of straps providing the electrical connection between the tubes. There

were three phases of tube elements, each consisting of ten sets of elements in series. The tubes were made of Nichrome V for high electrical resistance. This arrangement necessitated electrical connections between tubes at the discharge end. As shown in Fig. 1, the original connectors were in the form of single, heavy, nickel straps. There were several factors contributing to the strap problems. The straps had to have sufficient cross section to avoid excessive electrical heating from their own resistance, which would cause a high oxidation rate and loss of strength. To accommodate uneven thermal expansion and contraction of the tubes, the straps had to have high flexibility, a condition incompatible with high cross section for the original strap configuration. Added to this was a loss in strength of the straps at high temperature which permitted gravity and electromagnetic field forces to droop or deform the straps. Periodically, this deformation became great enough to cause contact between adjacent straps, resulting in electrical short circuits and failure.

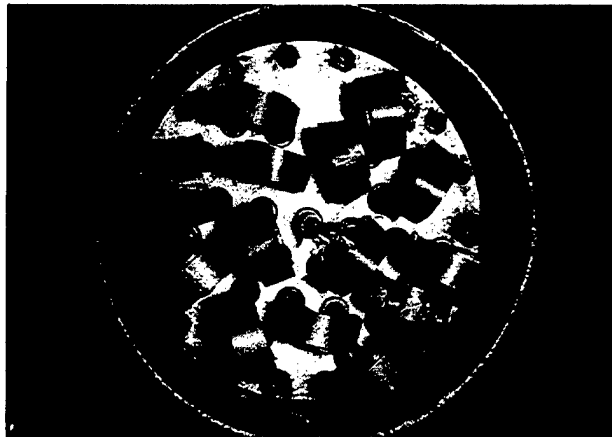


Fig. 1 AEDC-VKF 1500°F Heater Original Connectors

Numerous strap configurations were conceived and tested, leading to the final design shown in a partially assembled bundle in Fig. 2. In Fig. 3, the modified connector configuration is shown at 1650°F as it was



Fig. 2 AEDC-VKF 1500°F Heater Modified Connectors

tested in a special rig which was developed to permit viewing the connectors under operating temperature and anticipated motion. As a result of this and other modifications, good operational reliability of the heater has been achieved.

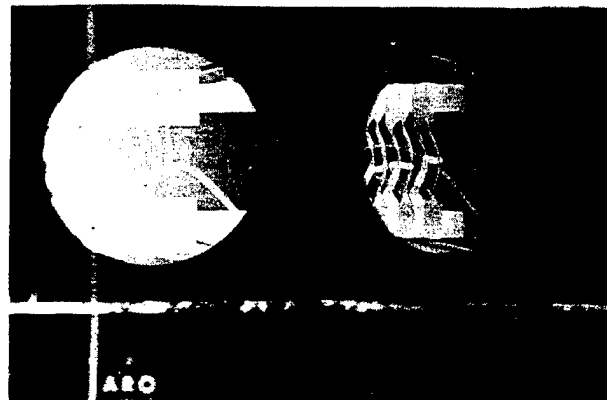


Fig. 3 AEDC-VKF 1500°F Heater Testing of Modified Connectors at 1650°F

2000°F AIR HEATER

It is envisaged that in the future Tunnel C (see page 50) will be equipped with a Mach 12 nozzle and a new heater to provide the required air temperature of 2000°F. A pilot heater, developed in the VKF (Ref. 1), consists of 15-ft-long resistance elements made of helical coils of Kanthal A-1 resistance wire held in the center of cylindrical alumina insulators of larger ID than the coil (Fig. 4). The air passes longitudinally through the annuli. The continuous coil and insulation are enclosed in a close-fitting stainless steel tube to force the air over the heated wire.

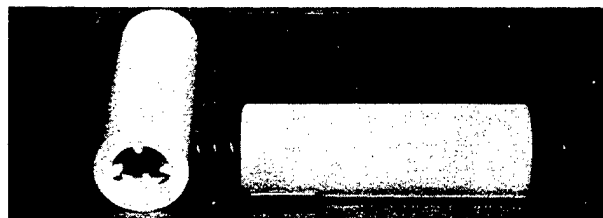


Fig. 4 AEDC-VKF 2000°F Air Heater Insulators and Coil

Tests were made at mass flows from 0.2 to 0.7 lb/sec per tube, air outlet temperatures from 500 to 2000°F, and pressures from 600 to 1800 psia. A final endurance run of 100 hr at maximum pressure and temperature was made without incident or evidence of impending failure. Based on this development, a full-scale 12,000-kw heater for 2000°F was designed and is now under construction.

REFERENCE

1. Daniels, H. C. and Crawford, H. E. "Development and Preliminary Design of a 2000°F Air Heater." AEDC-TN-61-118, November 1961.

DEVELOPMENT OF CONTINUOUS, HYPERSONIC TUNNELS

By
J. C. Sivells

HISTORICAL BACKGROUND

The development of the AEDC-VKF 50-in.-diam continuous-flow hypersonic tunnels began in 1957 with the design and fabrication of a conical nozzle with interchangeable throat sections to produce Mach numbers of approximately 7 and 8. The original purpose of this nozzle was to check out the associated equipment - the VKF compressor plant, the propane-fired combustion heater, the 12,000-kw electric heater, and the after-cooler between the downstream end of the nozzle and the inlet of the first-stage compressors. All of the equipment functioned satisfactorily with the exception of the electric heater, which was subsequently redesigned for use with the AEDC-VKF Mach 10 Tunnel. The temperatures obtained from the combustion heater were sufficient to avoid liquefaction of the air at Mach numbers of 7 and 8.

Because the conical nozzle provided the largest hypersonic tunnel available, a few aerodynamic tests were attempted in spite of the poor quality of flow in the test region. Not only was there present the Mach number gradient associated with any conical nozzle but also large deviations from the mean Mach number because the nozzle was not truly conical as a result of the simple method used in its fabrication. The poor flow quality led to the decision to design and fabricate a contoured axisymmetric nozzle to produce a Mach number of 8. The high pressure housing for the throat, the model support section, the diffuser, and the calibrating equipment for the conical nozzle were incorporated in the design of the contoured nozzle.

AEDC-VKF MACH 8 TUNNEL

DESIGN

The aerodynamic design and calibration of the AEDC-VKF 50-in. hypersonic tunnels are given in Ref. 1. The inviscid contour for the Mach 8 nozzle was selected from those given in Ref. 2. The nozzle contours given therein were calculated by the method of axisymmetric characteristics, assuming that the flow at the inflection point was radial as if emanating from a point source. In order to provide continuous curvature of the contour, the centerline Mach number distribution between the end of the radial flow region and the beginning of the parallel flow region was described by a cubic equation. The constants in the cubic equation were selected to make the Mach number gradient continuous throughout and equal to zero at the beginning of the parallel flow region.

To the coordinates of the inviscid contour must be added a boundary-layer correction to obtain the physical coordinates of the nozzle. For the range of operating conditions of the AEDC-VKF 50-in. hypersonic tunnels,

the boundary layer is turbulent for the full length of the nozzle. Because of the meager amount of experimental data on boundary-layer growth at hypersonic speeds, many empirical methods have been developed which attempt to apply low-speed data to flow at supersonic and hypersonic speeds. For the Mach 8 contour, the method used to calculate the boundary-layer growth was one in which the reference temperature was the arithmetic mean between free-stream and wall temperatures. During the fabrication and early operation of the tunnel, an improved method was developed which correlated well with experimental measurements made in the earlier conical nozzle and in the contoured nozzle. This improved method, which is described in Ref. 3, used a modification of Stewartson's transformation to simplify the integration of the von Kármán momentum equation. The approximate effects of heat transfer between the air and the tunnel wall were taken into account by evaluating the air properties at Eckert's reference temperature and by using the adiabatic-wall temperature instead of the stagnation temperature in Crocco's quadratic for the temperature distribution in the boundary layer.

The throat contour for the Mach 8 contoured nozzle was defined by simple equations - a cubic equation upstream of the throat and a semi-cubic equation downstream until it was tangent to a conical section which, in turn, was tangent to the physical contour at the inflection point. The constants of the equations were selected to produce continuous curvature along the entire contour and to make the radius of curvature at the throat equal to five times the throat radius.

The Mach 8 contoured nozzle was constructed in 1958. The throat section was designed to fit the pressure shell used for the throat of the conical nozzle. Downstream of the throat section, the nozzle was fabricated in six sections to facilitate machining the contours. Each section had double walls for the water cooling system and was flanged to mate with the adjacent sections. Some of the details are shown in Figs. 1 and 2.

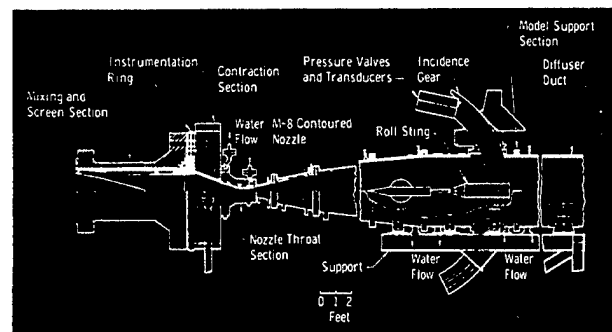


Fig. 1 General Arrangement of AEDC-VKF Mach 8 Tunnel

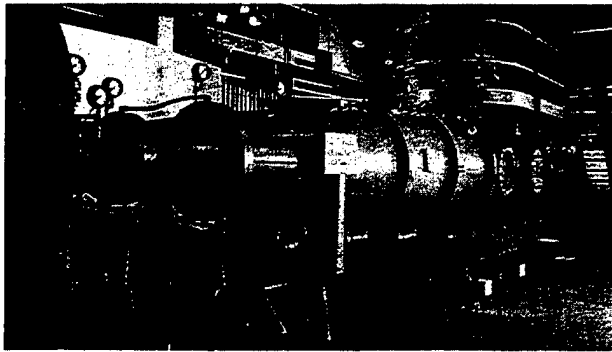


Fig. 2 View of AEDC-VKF Mach 8 Tunnel, Looking Downstream

CALIBRATION

The Mach number distribution in the test region was determined by means of pitot-tube surveys. A typical result of the calibration is shown in Fig. 3. The centerline Mach number distribution is uniform within about ± 1 percent, whereas off-center the flow is uniform to about ± 0.3 percent. Because of changes in boundary-layer thickness caused by changes in pressure level, the average Mach number is a function of pressure level and approximately follows the empirical relation, $M = 8.125 - 30/(p_0 + 120)$, where the stagnation pressure, p_0 , is measured in psia over the range of stagnation pressure levels from 100 to 900 psia. There is a slight mean axial gradient on the order of 0.01 Mach number per foot, although local gradients on the centerline exceed this value considerably. The AEDC-VKF Mach 8 Tunnel has been operational since October 1958.

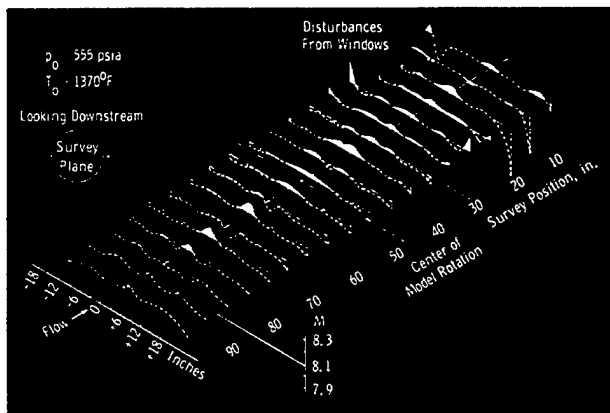


Fig. 3 Calibration of Mach 8 Tunnel

AEDC-VKF MACH 10 TUNNEL

DESIGN

The success of the Mach 8 contoured nozzle in producing reasonably uniform flow led to the development of a Mach 10 contoured nozzle operated from the same VKF compressor plant but as a completely separate wind tunnel. Its air is initially heated by the

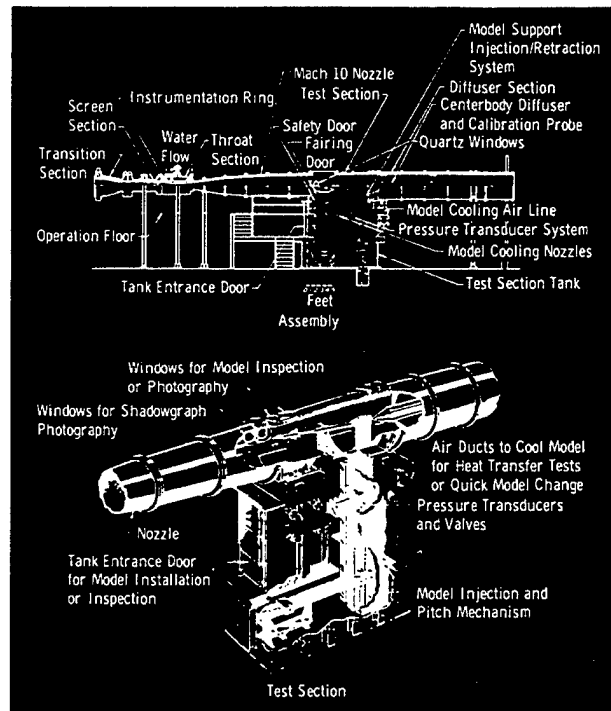


Fig. 4 General Arrangement of AEDC-VKF Mach 10 Tunnel

same combustion heater, but the stagnation temperature is further heated up to a maximum of 1450°F by the modified 12,000-kw electric heater.

The Mach 10 nozzle was designed so that it could be replaced later with a Mach 12 nozzle. Moreover, it was thought that the same downstream contour, corrected for the boundary-layer-displacement thickness, might be usable for both Mach numbers. If this idea proved to be practical, only the sections upstream of the inflection point would need to be interchanged. Since these sections are relatively short, a considerable saving would be effected, not only in initial cost but also in the time required each time the sections are changed. In order to match the downstream section, both upstream sections must have the same ordinate and slope at the inflection point after the boundary-layer correction is made. If it is found later in the calibration that separate downstream sections are required, at least nothing will have been lost by adopting this philosophy.

The inviscid contour for Mach 12 was also obtained from Ref. 2. The boundary-layer correction was then calculated by the method of Ref. 3 so that a physical contour for Mach 12 could be determined. It was then necessary to determine the parameters for a Mach 10 inviscid contour which, when corrected for its boundary-layer growth, would match the Mach 12 contour at the inflection point and at the test section. After many trials, such parameters were established and the characteristic solution for the inviscid contour was computed by the Digital Computation Branch of the Aeronautical Research

Laboratory at the Wright Air Development Center which also computed the contours of Ref. 2.

The throat contour for the Mach 10 nozzle was obtained by equations similar to those used for the Mach 8 nozzle. In this case, however, the throat radius of curvature was made equal to thirty times the throat radius since this parameter was believed to be a factor in the quality of flow obtainable in the test region.

The AEDC-VKF Mach 10 Tunnel was constructed in 1960. Details of the stress and thermal analysis used in the throat design are given in Ref. 4, and the mechanical design of the tunnel is given in Ref. 5. Some of the details of fabrication are shown in Figs. 4 and 5.

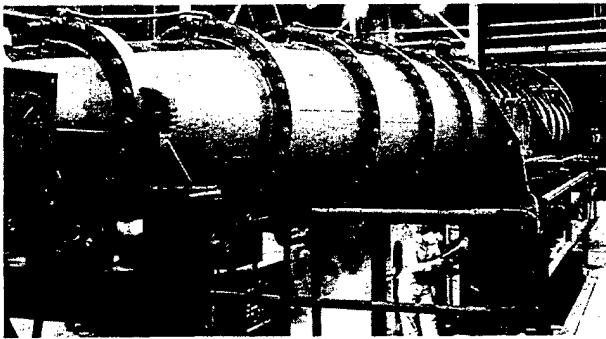


Fig. 5 View of AEDC-VKF Mach 10 Tunnel, Looking Downstream

CALIBRATION

The Mach number distribution in the test section was determined by means of pitot-tube surveys. A typical result of the calibration is given in Fig. 6. The centerline Mach number distribution is uniform within about 0.5 percent, whereas off-center the flow is uniform to about 0.2 percent. The average Mach number is again a function of pressure level and approximately follows the empirical relation, $M = 10.250 - 150/(p_0 + 500)$, where the stagnation pressure, p_0 , is measured in psia over the range from 200 to 2000 psia. Again there is a slight mean axial gradient on the order of 0.01 Mach number per foot. The AEDC-VKF Mach 10 Tunnel has been operational since May 1961.

MODEL SUPPORT

A unique feature of the AEDC-VKF Mach 10 Tunnel is the model support system. As shown in Fig. 4, a tank is located directly under the test section. The model and its support can be retracted into this tank which can then be sealed off from the test section and vented to atmospheric pressure while the airflow is maintained in the test section. Personnel can then enter the tank to change the model configuration. For testing, the personnel entrance door is closed, and the tank is vented to the test section pressure, after which the doors between the tank and test section are opened and the model and support

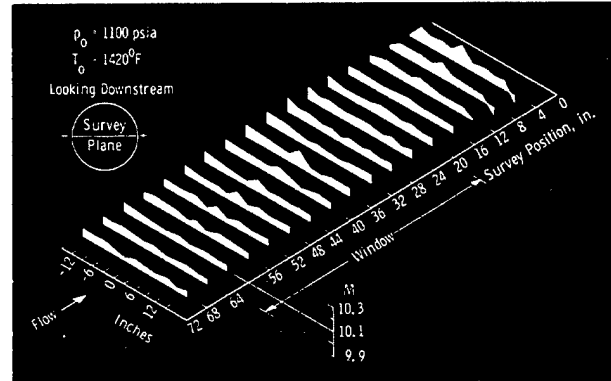


Fig. 6 Mach Number Distribution in the Mach 10 Tunnel

can be injected into the airstream. Injection time is approximately two seconds, with a maximum acceleration or deceleration of about one g. For prolonged tests, fairing doors are closed to preserve the circular cross section of the tunnel and to protect the tank equipment from excessive temperatures. For transient heat-transfer tests, the model is cooled in the retracted position and injected into the airstream for the five to ten seconds required to obtain the time history of the model skin temperatures.

Through the use of this model injection system, a considerable amount of time is saved which is normally lost in a continuous wind tunnel in which the airflow must be stopped each time the model configuration is changed. Also, the tunnel starting and stopping loads on the model are eliminated, the tunnel starting pressure ratio is reduced without the model in place, and the life of the heater and other plant equipment is prolonged since the deterioration is reduced by steady operating conditions.

REFERENCES

1. Sivells, James C. "Aerodynamic Design and Calibration of the VKF 50-Inch Hypersonic Wind Tunnels." AEDC-TDR-62-230, March 1963.
2. Cresci, Robert J. "Tabulation of Coordinates for Hypersonic Axisymmetric Nozzles Part 1 - Analysis and Coordinates for Test Section Mach Numbers of 8, 12, and 20." WADC-TN-58-300, Part 1, October 1958.
3. Sivells, James C. and Payne, Robert G. "A Method of Calculating Turbulent-Boundary-Layer Growth at Hypersonic Mach Numbers." AEDC-TR-59-3, March 1959.
4. Sherman, R. and Cook, J. P. "Stress and Thermal Analysis of the Throat Sections - 50-Inch Mach 10 and 12 Tunnel." AEDC-TDR-62-231, February 1963.
5. Howard, Charles M. and Wood, H. T., Jr. "Mechanical Design of the 50-Inch Mach 10-12 Tunnel." AEDC-TDR-62-229, April 1963.

THE HOTSHOT STORY

The two contributions here included summarize the development of the hotshot-type tunnel technique, which was originated by the VKF in the mid-fifties and has since been carried out to the point of routine acquisition of reliable force, pressure, and heat-transfer data in the Mach 20 range, at flow velocities of about 10 kft/sec. Limitations of hotshot-type tunnels and characteristics of inductive power supplies are discussed. The latter installations are unique and are capable of generating currents up to a million-ampere level.

DEVELOPMENT OF HOTSHOT-TYPE WIND TUNNELS

By

J. Lukasiewicz and R. Jackson

Several years ago the name hotshot was coined in the VKF (then known as the Gas Dynamics Facility) to describe a new type of blow-down hypersonic wind tunnel in which the working gas was directly energized by a short-duration electric arc discharge. The term was soon universally accepted and for some years now has been consistently used with reference to this particular type of arc-driven wind tunnel.

The development of hotshot tunnels started in the VKF in about 1955 and followed experimentation with arc-driven shock tubes. Although the basic principle of the hotshot tunnel remained unchanged throughout a decade, it has been only since 1961 that reliable aerodynamic results could be obtained from hotshots. As is often the case with technological innovations, the success was obtained only after extensive, careful, and often tedious development had been completed.

Following introduction of hotshots at the AEDC, several hotshot installations have been built in this country and abroad. The following organizations are among the hotshot operators today: Boeing Aircraft Company, Chance Vought Corporation, McDonnell Aircraft Company, North American Aviation Company, ONERA (France), Lockheed Missile Division, University of Michigan, Stanford University, NASA-Langley Research Center, and United Aircraft Corporation.

The hotshot tunnels, in their present stage of development, provide aerodynamic simulation in terms of Mach and Reynolds numbers, at Mach numbers on the order of 20 and at actual flow velocities of about 10,000 ft/sec. Compared to other $M = 20$ tunnels, shock-tube-driven tunnels, for example, hotshots offer an order of magnitude longer running time (in the 50-msec range) and hence an ease of instrumentation. On the other hand, based on the VKF studies, their potential for development to operation at actual space-flight velocities (20,000 ft/sec or more) is not promising.

It is pertinent to recall at this point that the hotshot principle was originally conceived as one which would enable attainment of hypervelocities in a wind tunnel. As indicated, this objective has not been achieved to date; nevertheless, the idea has resulted in the development of a most useful aerodynamic tool.

The development of hotshot tunnels, which was accomplished in the VKF before 1962, has been reported in considerable detail*; only the salient phases of this work will be here mentioned.

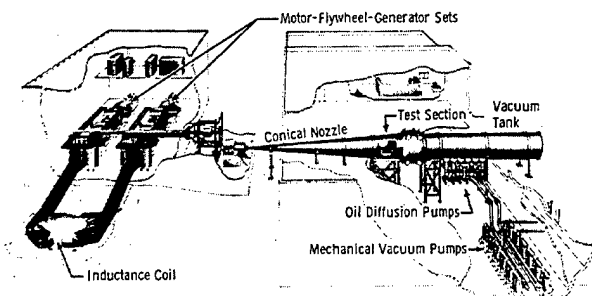


Fig. 1 The 100-Inch Hypervelocity Tunnel Installation

BASIC FEATURES OF HOTSHOT TUNNELS

At present two large hotshot tunnels are in daily use in the VKF. Their test sections measure 50-in. and 100-in. in diameter, and the tunnels are driven by nominal inductive coil energy supplies of 10 million and 100 million joules capacity, respectively. The original, 16-in.-diam, one-million-joule, condenser-driven, prototype hotshot tunnel, with which much basic development was done, is no longer in existence.

*A list of references related to development of AEDC-VKF hotshot tunnels is given on page 57.

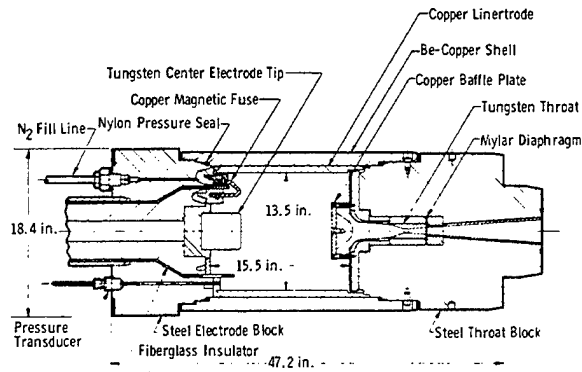


Fig. 2 Arc Chamber for the 100-Inch Hypervelocity Tunnel (F)

The 100-in. hotshot, which is the largest hypersonic tunnel known, is shown in Fig. 1, with Fig. 2 giving the details of the arc chamber. The electrical circuit is shown schematically in Fig. 3.

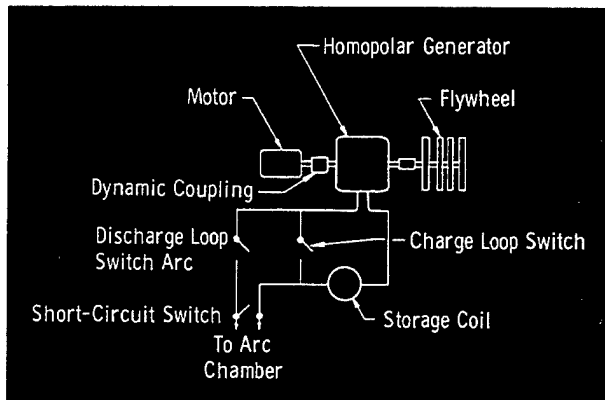


Fig. 3 Schematic of Inductive Drive for a Hotshot Tunnel

The operation of a hotshot tunnel consists essentially of storing the electrical energy in an inductive coil or in a condenser bank and discharging it in the arc chamber, thus pressurizing and heating the working gas. This causes a diaphragm, located near the nozzle throat, to burst and the gas to expand to a high Mach number into the previously evacuated nozzle. A quasi-steady flow period, of some 20- to 60-msec duration, is obtained in the test section, the reservoir pressure and temperature continually decreasing during this time to the extent of some 10 percent.

MAJOR STAGES OF HOTSHOT DEVELOPMENT

ARC CHAMBER

Early investigations of the hotshot tunnels have clearly indicated that flow contamination was mainly responsible for large deviations of measurements (e.g., drag and heat transfer) from expected theoretical values. The effects of contamination of the working gas with the arc-chamber materials were considered to be of two distinct

types: (1) chemical and thermodynamic effects which affect the chemical composition of the working gas and its thermodynamic state and (2) mechanical effects of contamination of the working gas with solid particles consisting of either metals or products of chemical reactions (e.g., oxides). Since effects of both types of contamination increased in severity with temperature, it was desirable to first reduce them to acceptable limits when operating in the lower temperature range from 3000 to 4000°K at peak pressures from 15,000 to 20,000 psi.

Experience with air and early arc-chamber designs, in which considerable areas on nylon insulators were exposed to the working gas, had shown that pyrolysis of nylon took place and resulted in the addition of hydrogen. This, in turn, caused large errors in the calculated arc-chamber enthalpy, based on the assumption of pure air. At higher energy levels, these errors amounted to as much as 100 percent. Moreover, with the air (hence oxygen) present, formation of water and other oxides took place, the oxygen having been seriously depleted.

These chemical effects are indicated in Table 1, which shows composition of test section gas (collected during a run) with air used in the arc chamber. Appreciable depletion of oxygen is evident in all cases, with large amounts of hydrogen present when nylon arc-chamber liners were used.

Table 1
Test Section Gas Composition

Arc-Chamber Liner Material	T ₀ , °K	Gas Composition, Percent by Volume							
		N ₂ + CO	O ₂	H ₂	H ₂ O	CO ₂	NO	H ₂ O + H ₂	
Nylon	6000	52	8.5	10.7	17	1.1	---	27.7	
Nylon	4000	75	3.7	4.7	12.1	3.6	---	16.7	
Copper	4000	78	8	0.1	7.1	3.1	2.2	7.2	
Steel	4000	81	12	0.3	3.8	2	---	4.1	

The thermochemical effects were virtually eliminated by the use of nitrogen as the working gas instead of air and by elimination, inasmuch as possible, of the exposed insulation. From the point of view of aerodynamic measurements, the use of nitrogen was not considered detrimental since calculations had shown that only small differences would exist between air tests and nitrogen tests in the above-mentioned temperature range (Ref. 1). For example, normal shock and wedge pressure coefficients would differ by less than five percent; stagnation point heat transfer, for the same stagnation enthalpy and Mach number, would differ by not more than eight percent. Such differences were within the accuracy of experimental measurements in the "high" hypersonic facilities.

It was also established that the use of nitrogen resulted in one other additional benefit: it eliminated the erosion of tungsten throats. This was consistent with the observed ignition temperature of 1500°K of tungsten in air.

EXPERIMENTAL TECHNIQUES

The mechanical contamination effects mentioned were reduced to an acceptable level by the development of arc-chamber design. The main steps in its evolution were as follows:

1. replacement of a silver solder fuse by a copper fuse which was opened by magnetic force;
2. change of electrode configuration from opposed or parallel to coaxial, with the arc-chamber cylindrical liner used as one electrode (linertrode);
3. addition of a baffle plate which shielded the nozzle throat from the electric arc.

These features of arc-chamber design are shown in Fig. 2. The significance of these arc-chamber design improvements can be judged from Fig. 4, where electrode weight losses (absolute and relative), particle collector weight increases, and stagnation-point heat-transfer rates are shown. Inspection of Fig. 4 indicates that in all cases an improvement of an order of magnitude has been realized. The losses of material from electrodes and fuse have been reduced to less than two percent (by weight) of the gas in the arc chamber. As an indication of the amount of solid particles in

the stream, measurements were made of the increase in weight during a run of a so-called particle collector (a small plate normal to the test section flow). Weight increases from over 10 mg/in.² have been reduced to 0.5 to 2 mg/in.². As was shown in Ref. 2, the stagnation point heat-transfer rate was extremely sensitive to the contamination of flow with solid particles. This was borne out by data shown in Fig. 4, which indicated that the ratio of experimentally measured to theoretically predicted heat-transfer rates, from values of 2.5 and higher, had been reduced to 1 ± 0.3 . The random scatter of measurements about the correct value indicated that, as discussed later, the variations probably were not caused by contamination, since the latter could account only for an increase of the heat-transfer rate.

DETERMINATION OF FREE-STREAM CONDITIONS AND HEAT-TRANSFER MEASUREMENTS

The above-summarized arc-chamber development resulted in 1961 in the ability to consistently obtain good pressure and force

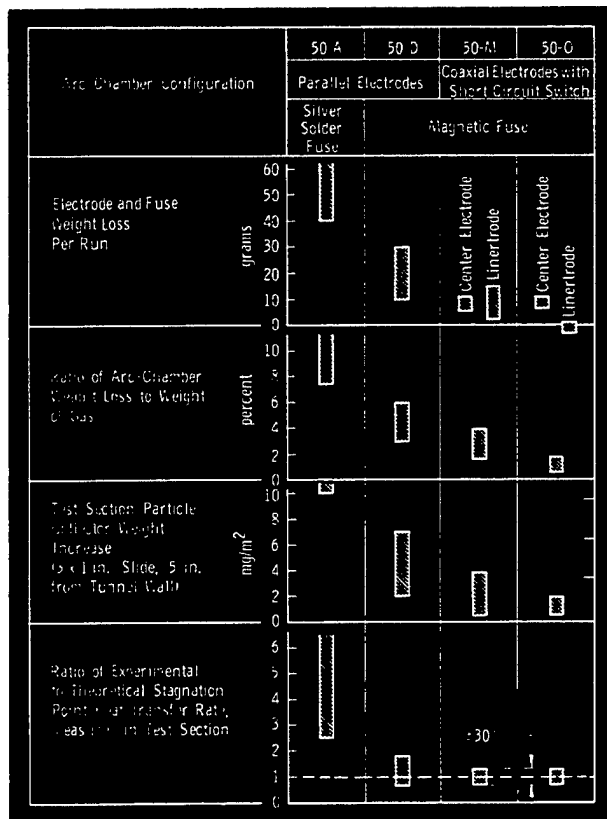


Fig. 4 Effects of Arc Chamber Development on Test Section Flow Purity

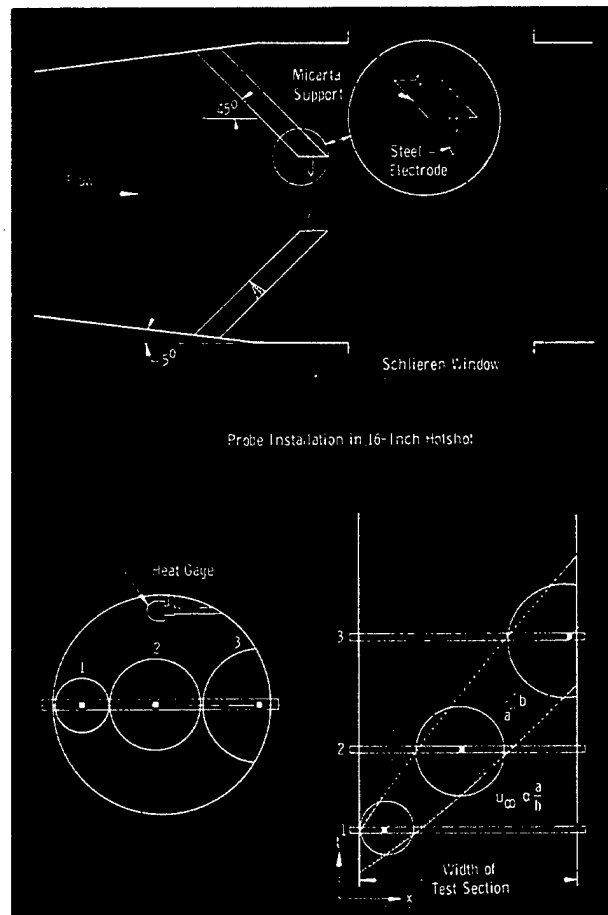


Fig. 5 Direct Measurement of Test Section Velocity by Blast Wave - Schlieren Smear Technique

data in hotshot tunnels, with a repeatability of ± 10 percent; however, as stated above, the timewise and run-to-run scatter in heat-transfer measurements was not yet acceptable.

The cause of this difficulty was traced to the non-uniformity of temperature and density distribution in the arc chamber, and the problem was satisfactorily resolved by direct measurement of flow velocity in the test section, which enabled the free-stream conditions to be determined with the desired accuracy at all times during a run.

The direct flow velocity measurements consisted essentially of the production of several cylindrical blast waves during a run and observation of their translation across the test section window by means of schlieren-smear photography. The blast waves were generated by electric arc discharges between electrodes located just upstream of the test section, as shown in Fig. 5.

Typical results of such measurements made in the 50-in. hotshot are shown in Fig. 6. Here U_{BW} , or free-stream velocity determined from the observations of blast waves (Fig. 6a), was compared with the velocity U_q deduced from the heat-transfer measurements on the shoulder of a 1-in.-diam hemispherical probe* and (Fig. 6b) with the velocity U_{AC} computed from the calculated, mean arc-chamber enthalpy (based on arc-chamber mean pressure measurements). Whereas U_q and U_{BW} are seen to agree to within ± 5 percent, much larger deviations were present in the U_{AC} vs U_{BW} correlation, clearly indicating that the assumption of uniform arc-chamber conditions was not valid. The excellent correlation between U_q and U_{BW} indicated that the flow enthalpy could be accurately calculated from the heat-transfer measurements.

The above experiments not only resolved the problem of heat-transfer measurements in hotshot tunnels, but also pointed out a convenient method of monitoring the flow contamination during every run; this was desired because of the possibility of a malfunction of the arc chamber. These two objectives were attained with a hemisphere-cylinder, heat-transfer probe, instrumented with two gages, one located at the stagnation point and the other at the shoulder. The former, being contamination sensitive, served as a monitor of flow purity, whereas the latter, together with the pitot pressure measurement, provided a measure of the flow enthalpy. Thus, the heat-transfer measurement, initially thought to be the

least accurate one, could now be used to provide reliable measurements of free-stream velocity and heat transfer on models.

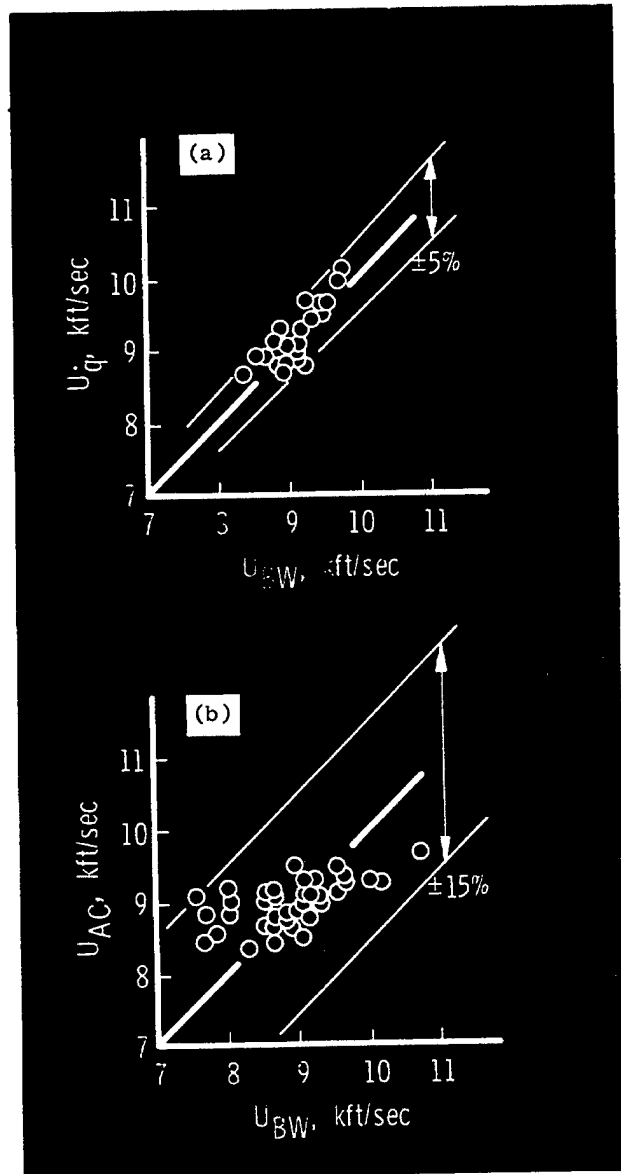


Fig. 6 Correlation of Measured Free-Stream Velocity with Computed Velocities

AERODYNAMIC TESTING IN HOTSHOT-TYPE TUNNELS

Some of the typical results of force, pressure, and heat-transfer measurements obtained in the VKF hotshot tunnels are shown and discussed elsewhere in this collection (see pages 5 and 17). All such measurements are being obtained with a reliability of ± 10 percent. Typical heat-transfer measurements on the surface of a 9-deg half-angle, blunted (0.3 bluntness

*Velocity U_q was calculated from the measured heat-transfer rate on the basis of Fay-Riddell theory for stagnation point heating (with zero dissociation for N_2 of reservoir densities above 20 amagats and reservoir temperatures below 5000°K) and Lees' distribution of heat-transfer rate.

ratio) cone obtained in the 100-in. hotshot, are compared with the theoretical values in Fig. 7. It is evident that low absolute heat-transfer rates are being satisfactorily measured.

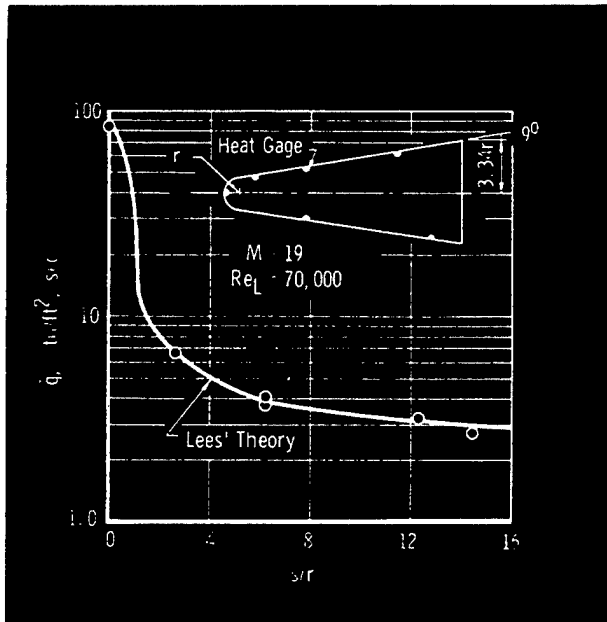


Fig. 7 Heat-Transfer Measurements on a Slender Blunted Cone

Typical operating range of hotshot tunnels is shown in Fig. 8, in terms of Mach and Reynolds numbers, the appropriate simulation parameters. Corresponding altitudes for duplication of Mach and Reynolds numbers with full-scale models are also indicated.

As regards utilization of hotshot tunnels, in view of their large size it is often possible to test two or more models simultaneously. The models may differ in configuration or they may be identical models at different angles of attack. A multi-model setup is shown in Fig. 9 in the test section of the 100-in. hotshot. It has also been possible, at least in one case so far, to test a full-scale model in the 100-in. hotshot (in connection with the space nuclear auxiliary power (SNAP) project).

LIMITATIONS OF HIGH TEMPERATURE OPERATION

Operation with air at enthalpies at which measurable real gas effects are present is the goal of all hypervelocity test facilities. Although hotshot tunnels have not been used in this regime, some of the difficulties and limitations to be expected became evident from the available experimental data (Refs. 5 and 6). They related to two distinct problems, namely: (1) the ability of arc-chamber components to withstand high enthalpy, high pressure conditions and (2) the heat losses from the working gas.

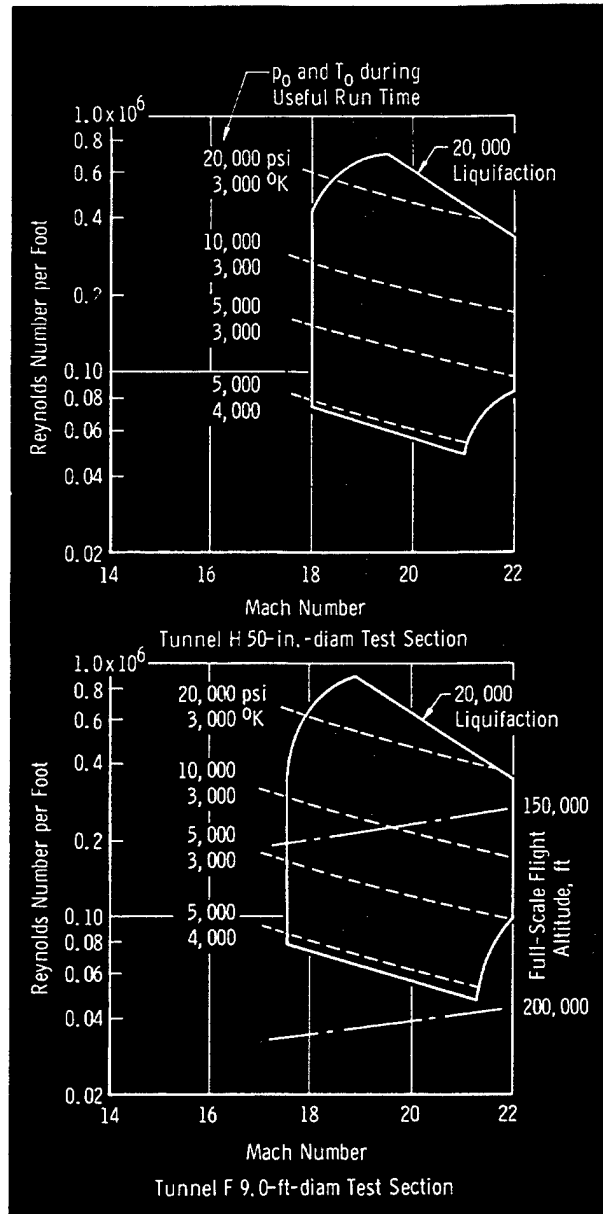


Fig. 8 Mach-Reynolds Number Range of Operation of Hotshot Tunnels

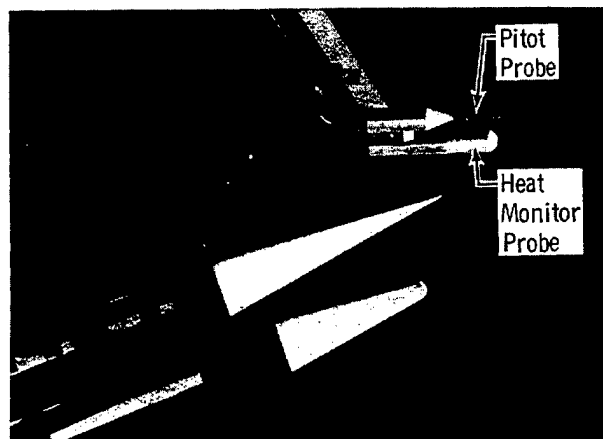


Fig. 9 Multi Model Test

From a limited experimental program it was found that at reservoir temperatures from 6000 to 9000°K, the loss of mass of arc-chamber components increased by an order of magnitude or more compared to the operation at 4000°K or below. This was also reflected by the stagnation point heat-transfer measurements which showed a several-fold increase over the theoretical values.

An even more basic limitation was established as a result of analysis of heat losses from the gas to the arc-chamber walls. Figure 10 shows a comparison of experimental heat losses with theoretical, blackbody radiation losses to a cold wall. At temperatures exceeding about 4000°K, the blackbody radiation assumption is seen to predict reasonably well the heat loss rate. Based on this finding, Fig. 11 was constructed in which decay of enthalpy of air caused by radiation is shown in terms of the At/V parameter which relates arc-chamber surface area, A , volume, V , and time, t . Figure 11 is generally applicable to any aerodynamic

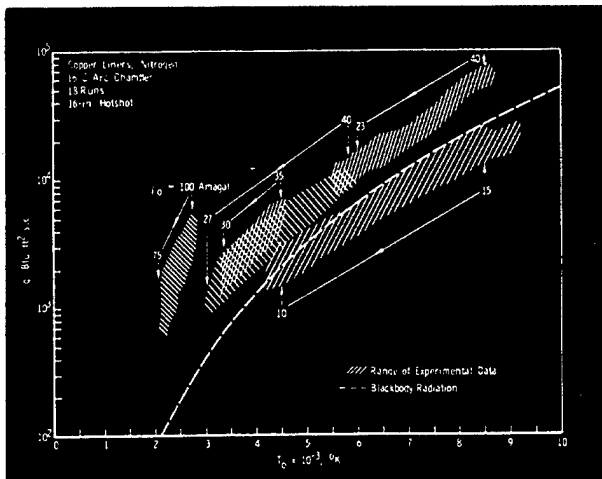


Fig. 10 Arc Chamber Heat Loss Rate

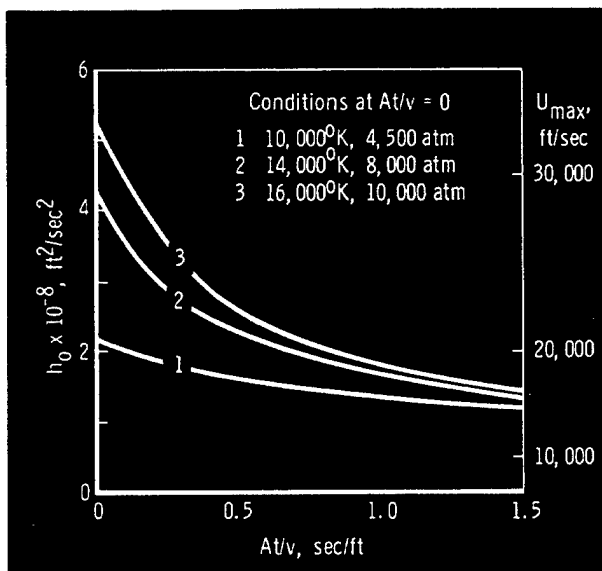


Fig. 11 Decay of Enthalpy of Air due to Radiation

test facility which employs reservoir heating and indicates that for such facilities, because of heat losses alone, short heating and running times are mandatory for operation at high enthalpies. For hotshot tunnels, the parameter At/V ranges from 0.4 to 1 sec/ft. At values of $At/V < 0.1$, a temperature of only 10,000°K at 4500-atm pressure is required to reach 20,000 ft/sec; however, in the hotshot range of At/V , initial reservoir temperatures from 14,000 to over 16,000°K (or an initial reservoir enthalpy over two times higher) would be required to achieve this velocity in the test section, thus compounding many times the arc-chamber and flow contamination problems which are already extremely severe at 10,000°K.

From such evidence and analyses it was concluded in early 1962 that hotshot tunnels in their present form are less likely than other types of facilities to be capable of operation at space-flight enthalpies.

REFERENCES

1. Perry, R. W. and MacDermott, W. N. "Development of the Spark-Heated Hypervelocity, Blowdown Tunnel-Hotshot." AEDC-TR-58-6, June 1958 (AGARD Report No. 233).
2. Lukasiewicz, J., Harris, W. G., Jackson, R., van der Bliek, J., and Miller, R. M. "Development of Capacitance and Inductance Driven Hotshot Tunnels." AEDC-TN-60-222, January 1961; Hypervelocity Techniques Symposium, Proceedings of National Symposium on Hypervelocity Techniques, IAS, 1960, pp. 67-92 (Meeting held at Denver, Colo., October 1960).
3. van der Bliek, J., Deskins, H. E., and Walker, R. R., III. "Further Development of an Inductance-Driven Hotshot Tunnel." AEDC-TN-61-80, July 1961.
4. Grabau, M., Humphrey, R. L., and Little, W. J. "Determination of Test-Section, After-Shock, and Stagnation Conditions in Hotshot Tunnels Using Real Nitrogen at Temperatures from 3000 to 4000°K." AEDC-TN-61-82, July 1961.
5. van der Bliek, J. "Further Development of Capacitance and Inductance-Driven Hotshot Tunnels." AEDC-TDR-62-50, March 1962; Advances in Hypervelocity Techniques, Plenum Press, 1962, pp. 47-86, (Second Symposium on Hypervelocity Techniques, Denver, Colo., March 1962).
6. Lukasiewicz, J., Jackson, R. and Whitfield, J. D. "Status of Development of Hotshot Tunnels at the AEDC." AEDC preprint, to be published by AGARD (AGARD Meeting on "The High Temperature Aspects of Hypersonic Flow" at TCEA, Rhode-St. Genese, Belgium, April 1962).
7. Whitfield, J. D. and Norfleet, G. D. "Source Flow Effects in Conical Hypervelocity Nozzles." AEDC-TDR-62-116, June 1962.
8. Ball, H. W. "Calibration of the 100-Inch Hypervelocity Tunnel (F)." AEDC-TDR-63-46, March 1963.

INDUCTANCE ENERGY STORAGE SYSTEMS

By

R. R. Walker, III

The inductive power supplies used to drive the AEDC-VKF 50-in. and 100-in. tunnels have already been briefly described (see page 52). A schematic circuit diagram is given in Fig. 1a, and a cross-section of a unipolar generator is given in Fig. 1b.

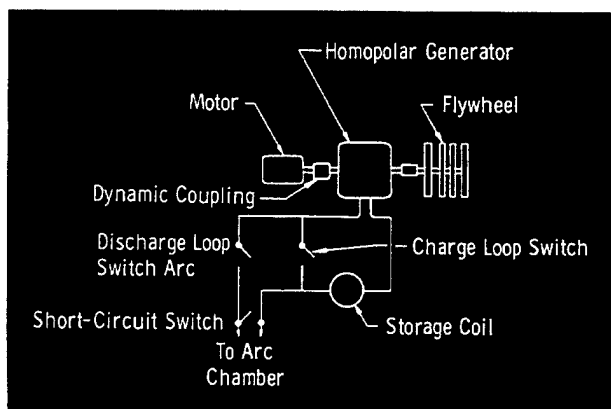


Fig. 1a Schematic of Inductive Drive for a Hypervelocity Tunnel

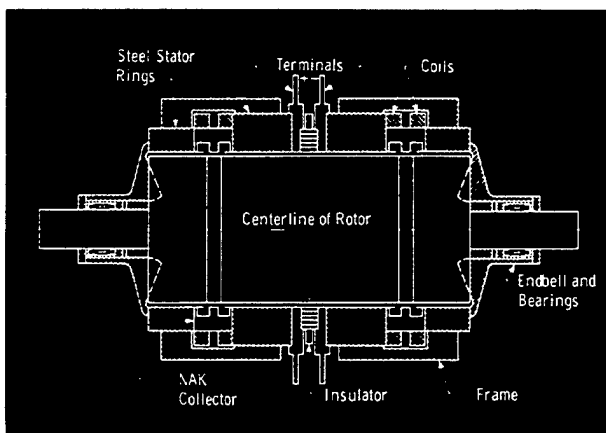


Fig. 1b Cross Section - Unipolar Generator

In general, energy is transferred from the electric power system to the flywheels in approximately 20 minutes, after which the kinetic energy is transformed to electrical energy via the unipolar generator. The electrical energy is transferred to the storage coil in a charging period of approximately 6 sec and is discharged via the

electric arc in the arc chamber in approximately 10 to 80 msec. Theoretically, during the charging cycle the unipolar generator can be treated as a capacitor (Ref. 1), and thus the inductance energy storage system becomes a standard electric RLC circuit with an initial voltage on the capacitor. During the discharge cycle, the arc resistance is nonlinear and theoretically, because of the short discharge times, the capacitor can be neglected so that the system becomes a standard, electrical, nonlinear RL circuit. Typical arc-current and voltage traces with and without short circuit switch (see Fig. 1a) are shown in Fig. 2 for the 10^7 -joule system. The traces are essentially the same for the 10^8 -joule system except for magnitudes. These systems are described in more detail in Refs. 2 through 5.

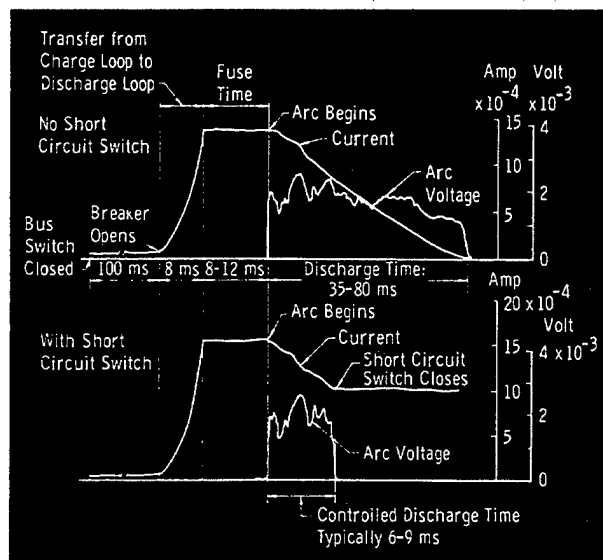


Fig. 2 Typical Current and Voltage Traces without and with Short Circuit Switch, 10^7 -joule Inductance Energy Storage System

It is interesting to note that if a 10^8 -joule system were discharged in 10 msec, the average power would be 10^{10} watts. At present, this power level practically equals the entire installed generating capacity of the Tennessee Valley Authority and represents approximately five percent of the installed generating capacity of the entire United States.

During development of the inductive power supplies several problems were encountered. One problem was switching the current from the charging circuit to the discharging circuit (Fig. 1a). This required transferring the current from the main breaker S-1, which had a very low resistance, into the arc chamber, which had a high resistance. In order to do this, a fuse was installed inside the arc chamber to carry the total current for approximately 10 msec while the main breaker S-1 opened and deionized. This was done to prevent an arc restriking in the breaker and dumping the energy outside the arc chamber. The fuse used initially consisted of silver-solder between the arcing tips of the electrodes (Fig. 3), however, complete melting of the fuse was required to draw the arc and resulted in high contamination of the test gas. To lower the contamination, a magnetic fuse was designed (Fig. 3); the magnetic forces break the fuse in tension when it is heated to a predetermined temperature. Thus, very little melting occurs, and the arc is very quickly transferred to tungsten arcing tips. A comparison of the weight losses for both types of fuses is shown in Fig. 3. By properly choosing the fuse cross-sectional area, the desired holding time may be obtained for a given current. In addition to operational flexibility, the magnetic fuse provides increased freedom in electrode design and also is simpler to fabricate.

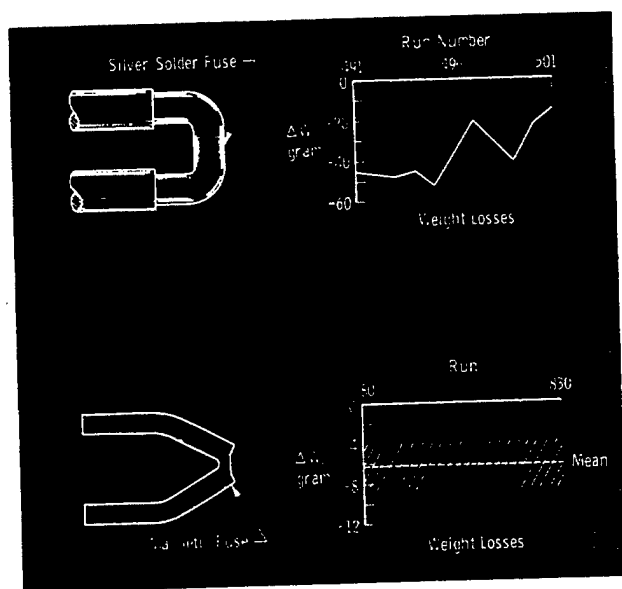


Fig. 3 Fuse Configurations Use in Inductance Energy Storage Systems

Another problem encountered was that of predicting the electrical characteristics of the arc for different energy requirements, arc-chamber configurations, electrode spacings, and initial test gas charge densities. From the experimentally observed

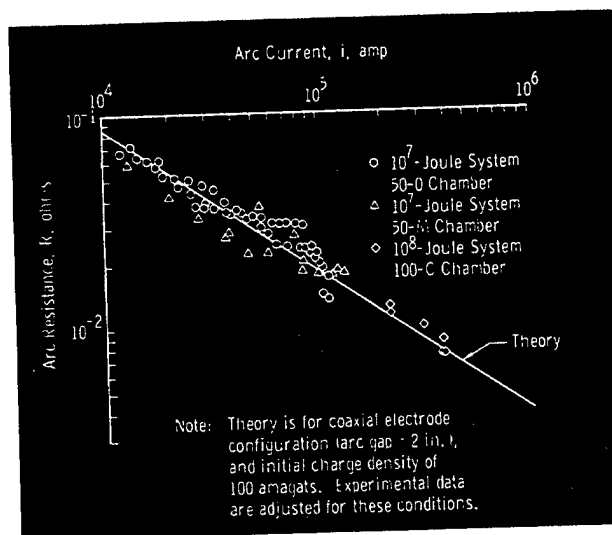


Fig. 4 Resistance - Current Characteristics of High Current, High Pressure Arcs

variation of arc resistance with current (Fig. 4), a semi-empirical theory for an inductance-driven arc discharge was developed. The experimentally determined variation of arc resistance with current was found to be

$$R = ai^{-n} \quad (1)$$

where a and n are empirical coefficients. Coefficient a was found to be a function of, at least, arc-chamber geometry, electrode arc gap, and initial charge density of the test gas. A systematic variation of coefficient n was not detected, and n was assumed constant. Substitution of eq. (1) into the differential equation for an RL circuit with an initial value i_0 of current yielded the following normalized equations which describe the arc discharge:

$$\text{Arc Current} \quad \bar{i} = i/i_0 = (1 - n\bar{t})^{1/n} \quad (2)$$

$$\text{Arc Voltage} \quad \bar{v} = v/v_0 = (\bar{i})^{1-n} \quad (3)$$

$$\text{Energy Delivered to the Arc} \quad \bar{E} = \Delta E_{\text{arc}}/E_0 = (1 - \bar{i}^2) \quad (4)$$

$$\text{Arc Resistance} \quad \bar{R} = R/R_0 = \bar{i}^{-n} \quad (5)$$

In Eqs. 2-5, $\bar{t} = t/T_0$, where $T_0 = L/R_0$ and $R_0 = a/i_0^n$. Thus, when a and n are known, the arc discharge characteristics are defined. A comparison of the experimental data from both the 10^7 - and 10^8 -joule systems with this semi-empirical theory is

shown in Fig. 5. A plot of \bar{v} vs \bar{i} for these arcs (Fig. 6) shows a positive characteristic which is of interest since most of the data in the published literature show a negative VI characteristic for arcs.

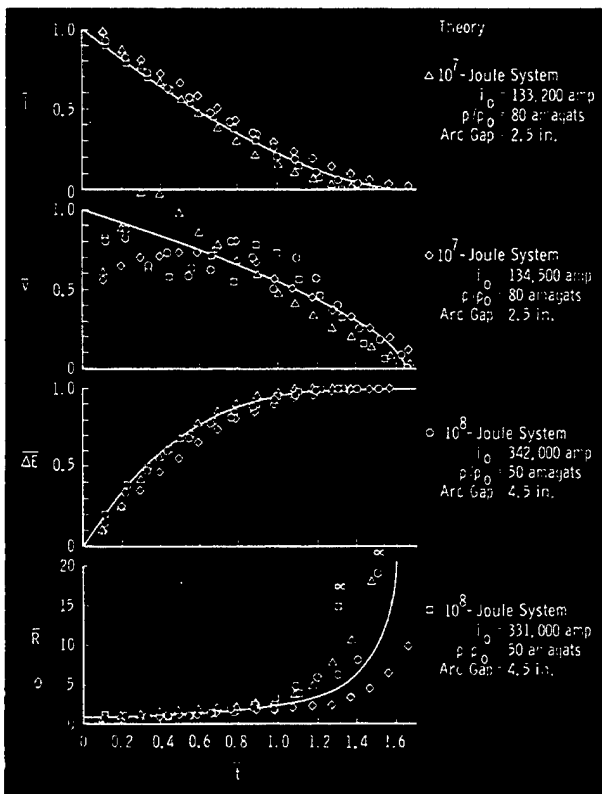


Fig. 5 Comparison of Normalized Current, Voltage, Energy, and Resistance Characteristics of High Current, High Pressure Arcs to Experimental Data

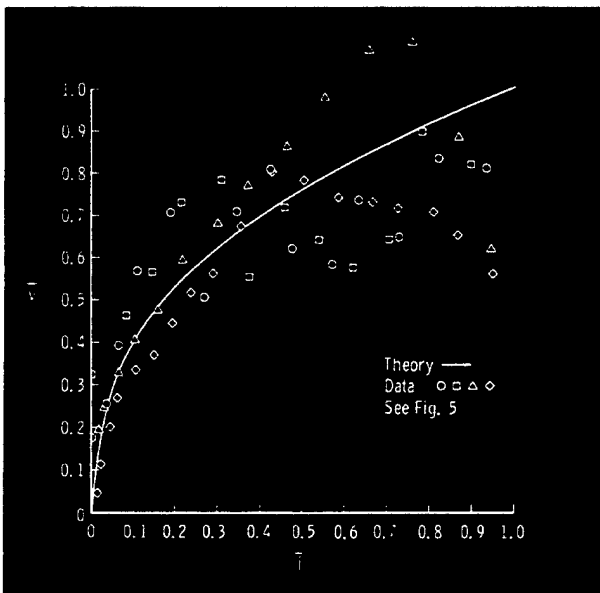


Fig. 6 Comparison of Normalized Voltage-Current Characteristic of High Current, High Pressure Arc to Experimental Data

In still another effort to reduce contamination of the test gas, the use of a short circuit switch (Figs. 1a and 2) to control the duration of the arc discharge, combined with the development of a coaxial electrode arc chamber, led to a considerable reduction in contamination of the test gas. The details of this development work are given in Ref. 3. Typical voltage and current traces with and without the short circuit switch are shown in Fig. 2 for the 10^7 -joule system. A drawing is shown in Fig. 7 of the short circuit switch, which is described in detail in Ref. 5.

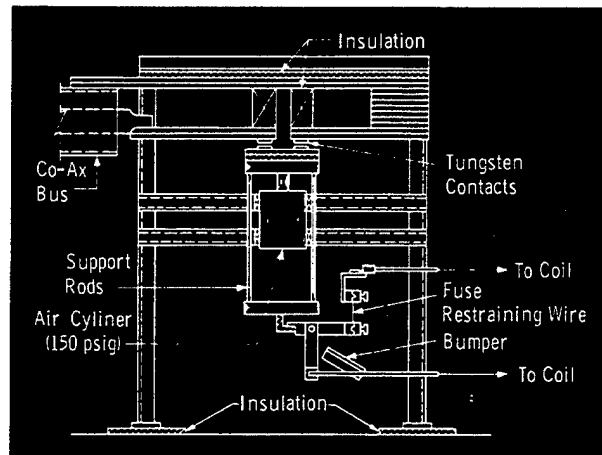


Fig. 7 Short Circuit Switch Used with 10^7 -joule Inductance Energy Storage System

These are but a few of several problems encountered in the development of suitable power supplies for arc-driven wind tunnels. Development is continuing to attain better and more flexible performance characteristics of the existing power supplies.

REFERENCES

1. Boyajian, Aram. "The D-C as a Capacitor." *Electrical Engineering*, Vol. 72, No. 2, February 1953, pp. 154-155.
2. Lukasiewicz, J., et al. "Development of Capacitance- and Inductance-Driven Hotshot Tunnels." AEDC-TN-60-222, January 1961.
3. van der Blik, J. A., Deskins, H. E., and Walker, R. R., III. "Further Development of an Inductance-Driven Hotshot Tunnel." AEDC-TN-61-80, July 1961.
4. van der Blik, J. A. "Further Development of Capacitance- and Inductance-Driven Hotshot Tunnels." AEDC-TDR-62-50, March 1962.
5. Fillers, A. H., Jr. "Inductive Power Supply for a Hotshot-Type Tunnel." AEDC-TDR-62-157, July 1962.

LOW-DENSITY FACILITY

It was evident in 1958 that although a number of low-density facilities existed in the country, none of them operated at high Mach numbers. And yet, in practice, the low-density conditions are unavoidably encountered at high Mach numbers, and, moreover, the theory indicates that it is a combination of high Mach number and low density which results in important viscous interaction effects. Hence, it was decided to proceed with the design and construction of a pilot, low-density, hypersonic wind tunnel. It was realized that major components required for the construction of such a tunnel existed and that only a minimum of development work would be necessary to obtain a useful test facility. The construction of the VKF pilot, low-density, hypersonic wind tunnel started in 1959 and the tunnel began to run in July 1960. The design of the LDH tunnel, including some of the more important advances made, is here described.

LOW-DENSITY, HYPERSONIC (LDH) WIND TUNNEL "L"

By

J. Leith Potter

The tunnel here described was completed in July 1960, and since that date it has been used continuously for investigations of low-density, high Mach number flows and various aspects of tunnel design. The aerodynamic investigations are separately dealt with (see page 21); a description of the wind tunnel is given, together with some experimental results relating directly to the tunnel design.

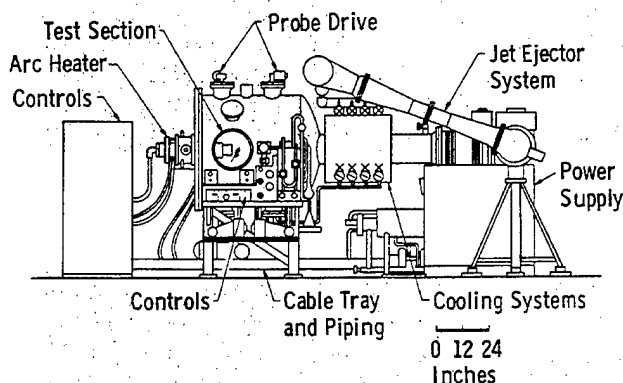


Fig. 1 AEDC-VKF-LDH Tunnel with Major Components Identified

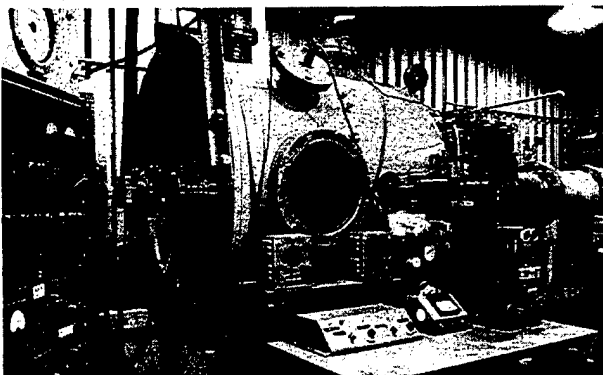


Fig. 2 AEDC-VKF-LDH Tunnel from the Operator's Side

TUNNEL L

This is a continuous-type, arc-heated, ejector-pumped design first described in Ref. 1. Figure 1 shows a simplified, elevation view of the tunnel, and Figs. 2 and 3 are photographs of the tunnel. The major components are (1) d-c arc-heater of the constricted, non-rotated arc type, with a 40-kw power supply; (2) settling section of variable length but normally about 6-in. long and 3 in. in diameter; (3) aerodynamic nozzle of varying design with 0.10-in.- to 0.75-in.-diam throat and up to 10-in.-diam exit; (4) a tank 48 in. in diameter surrounding the test section and containing instrumentation and probe carrier; (5) interchangeable diffuser; (6) air-ejector of two stages; and (7) the VKF vacuum pumping system. All critical components of the tunnel are protected by back-side water cooling. The two-stage ejector system is driven by air instead of steam because of the ready availability of the former and the expense of providing a steam supply. This tunnel has proved highly satisfactory, always yielding excellent repeatability of data.

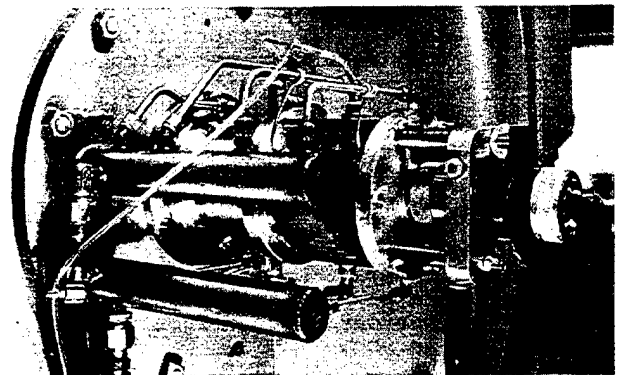


Fig. 3 Arc-Heater and Settling Chamber of AEDC-VKF-LDH Tunnel

The working gas normally is nitrogen or argon, although other gases may be used. Typical ranges of operating variables with heated flow and presently available nozzles are given in Table 1.

Table 1
LDH Tunnel Operating
Conditions with Arc-Heater

	Nitrogen	Argon
Total pressure, psia	7.0-29.4	0.5-6.4
Total enthalpy, Btu/lb	740-2130	280-960
Total temperature, °R	2300-7200	2300-7700
Mach number	4.8-10.8	3.7-16.1
Unit Reynolds number, free stream, in. ⁻¹	300-3500	270.0-4700
Unit Reynolds number behind normal shock, in. ⁻¹	35.0-1140	14.0-1080
Mean free path, free stream, billiard-ball gas model, in.	0.002-0.058	0.002-0.057
Uniform flow core diameter at test section, in.	0.2-1.2	0.5-1.5

Reservoir conditions have been established on the basis of measurements of total pressure, mass flow rate, and nozzle throat area. The total enthalpy computed from knowledge of these quantities has been verified by calorimeter measurements giving directly the total enthalpy downstream of the nozzle throat (Refs. 1-3).

Test section conditions have been established on the basis of measured or calculated reservoir conditions and determination of the existence of an inviscid core flow along the nozzle plus measurements of impact pressure, local mass flow rate, static pressure, and local total enthalpy (Refs. 1-3). These have been supplemented by measurements of drag and heat transfer which yield indirect verification of the calibration when compared to other experimental and theoretical data. Theoretical analysis of molecular vibrational relaxation (Ref. 4) has been relied on for final interpretation of experimental measurements. On this basis it is considered that molecular vibration is frozen at all stations downstream of the nozzle throat when nitrogen is the medium.

A typical calibration measurement of total enthalpy is compared with the computed total enthalpy in Fig. 4, and typical nozzle flow surveys are shown in Fig. 5. It will be noted that the usable, uniform test section core diameter is about 0.8 in. in this example. Computed boundary-layer thicknesses (Ref. 5) are compared with corresponding experimental data in Fig. 5; good agreement is evident. A photograph of a local total enthalpy probe is shown in Fig. 6, and data from the probe are presented in Fig. 7 where it will be noted that the measurements are

in good agreement with the flow model assumed for calculating theoretical total enthalpy. Figure 8 contains data obtained by use of a local mass flux probe, and there, too, it will be observed that measured and theoretically estimated values are in satisfactory agreement.

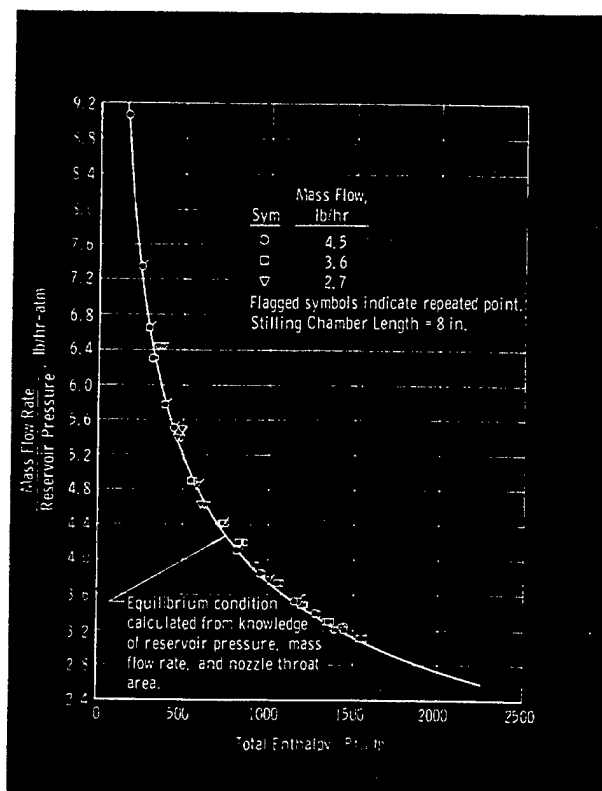


Fig. 4 Total Calorimeter Results for 8-in.-Long Stilling Chamber

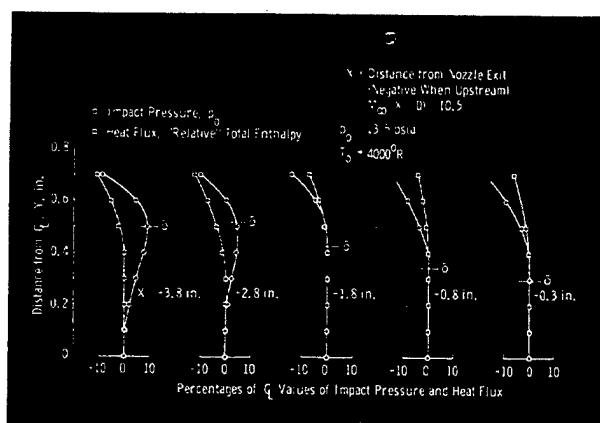


Fig. 5 Typical Results of Transverse Surveys at Various Axial Stations in the LDH Tunnel Conical Nozzle (Total Angle = 30 deg) (The edge of the boundary layer as computed from Ref. 5 is indicated by δ at each station. Nozzle radius at $X = -0.3$ in. is 2.84 in.)



Fig. 6 Photograph of Local Total-Enthalpy Probe in Hypersonic Argon Flow

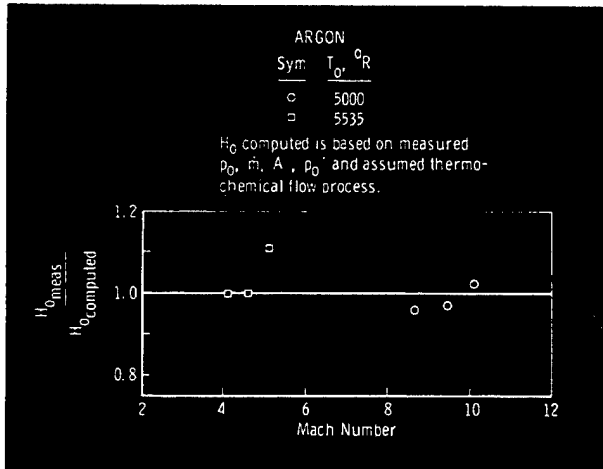


Fig. 7 Results from Local Total-Enthalpy Probe in the Low-Density, Arc-Heated Tunnel

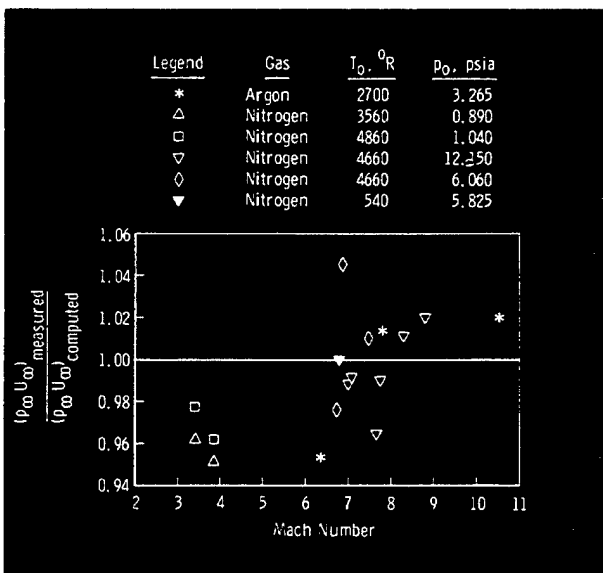


Fig. 8 Comparison of Measured and Calculated Local Mass Flux, $\rho_\infty U_\infty$

DIFFUSER STUDIES

Only a preliminary investigation has been reported at this date, but a more complete report is in preparation. The result of the earlier study is of utmost value in connection with the design of low-density, hypersonic tunnels because it offers clear proof

of significant pressure recovery from diffusers in low-density, hypersonic tunnels. Inasmuch as this has been reported in Ref. 1, no details are presented here. The pressure recovery is not comparable with that achieved in tunnels operating at high pressures, being only approximately ten percent of normal shock recovery at a Mach number of 10.5 for the present Tunnel L diffusers. However, this represents a factor of roughly four in the tunnel exit pressure which the pumping system must produce. The saving in cost of the pumping system is obvious.

OVEREXPANDED NOZZLE OPERATION

In the past it has been customary to provide sufficient vacuum pumping to enable the nozzle of the usual open-jet, low-density tunnel to exhaust to a pressure equal to the static pressure at the exit plane of the nozzle. The Tunnel L nozzle is operated with an overexpansion to test section static pressure varying from one to one-fifth of the pressure in the large tank surrounding the nozzle exit. The suitability of this arrangement has been established by flow surveys (Ref. 6). The diffuser and overexpansion together allow pressure at the entrance of the ejector system to be fifteen to thirty times as great as static pressure in the test section of the nozzle. Again, the saving in cost of the pumping system is significant.

REFERENCES

- Potter, J. L., Kinslow, M., Arney, G. D., Jr., and Bailey, A. B. "Initial Results from a Low-Density Hypervelocity Wind Tunnel." *Progress in Astronautics and Rocketry*, Ed. by F. R. Riddell, Academic Press, 1962, pp. 599-624.
- Arney, G. D., Jr. and Boylan, D. E. "A Calorimetric Investigation of Some Problems Associated with a Low-Density Hypervelocity Wind Tunnel." AEDC-TDR-63-19, February 1963.
- Potter, J. L., Arney, G. D., Jr., Kinslow, M., and Carden, W. H. "Gasdynamic Diagnosis of High-Speed Flows Expanded from Plasma States." IEEE International Symposium on Plasma Phenomena and Measurement, San Diego, California, 29 October - 1 November 1963.
- Lewis, A. D. and Arney, G. D., Jr. "Vibrational Nonequilibrium with Nitrogen in Low-Density Flow." AEDC-TDR-63-31, March 1963.
- Potter, J. L. and Durand, J. "Analysis of Very Thick Laminar Boundary Layers in Axisymmetric, High-Speed Fluid Flow." *Developments in Theoretical and Applied Mechanics*, Vol. 1, Plenum Press, 1963, pp. 341-360.
- Potter, J. L. and Boylan, D. E. "Experience with an Overexpanded Nozzle in a Low-Density, Hypervelocity Wind Tunnel." AEDC-TDR-62-85, April 1962.

HYPERVELOCITY RANGES

Work on development of hypervelocity range techniques has been proceeding in the VKF since 1957 in preparation for operation of the 1000 ft range, now being activated. In the field of launchers it has resulted in construction of practical, high performance, light gas guns and in the development of advanced design methods for this type of launcher. Introduction of powder heated hydrogen propellant in preference to the helium and steam formerly used was a significant step in this work. Instrumentation developments have included original Fresnel lens shadowgraph systems for operation at 30 kft/sec, microwave and model telemetry measuring methods, etc. The more significant results of these activities are treated in the two contributions which follow.

DEVELOPMENT OF LAUNCHERS FOR AEROBALLISTIC AND IMPACT RANGES

By

W. B. Stephenson

PERFORMANCE

Since 1959, various types of single- and two-stage, light-gas model launchers have been developed in the VKF for aerodynamic and impact testing. The first of these was a single-stage, 40-mm launcher which used a combustible mixture of hydrogen and oxygen to heat helium. This launcher was in a configuration which had been designed by the Naval Ordnance Laboratory. The computation of its performance is described in Ref. 1. Velocities up to about 15,000 ft/sec were obtained with a 40-gm projectile.

Another early development effort in the VKF was directed toward the use of electric arc heating of the light-gas propellant. A 20-mm launch tube was used with the arc chamber, and a maximum velocity of about 13,000 ft/sec was achieved with a 4-gm projectile. In Ref. 2, the difficulties inherent in arc heating, owing especially to the contamination of the propellant, are described, and experimental results are given. It was concluded that the simple arc heating method is not feasible for obtaining high launch velocity. Figure 1 shows some of the results of experiments demonstrating the loss in velocity as the contamination level increased. As the helium density decreased, the temperature and theoretical velocity increased. However, the experimental velocity decreased because of the rapid increase in material loss from the arc chamber.

Early in 1960, experiments were begun with a two-stage launcher based on a configuration used at the Ames Research Center (Fig. 2). With this arrangement, a plastic piston one to four diameters long is driven through the pump tube by hydrogen compressed by smokeless powder in the chamber. Ahead of the piston, the propellant hydrogen is compressed to about 20,000 atm by exchange of kinetic energy from the piston to the propellant. The projectile starts to move

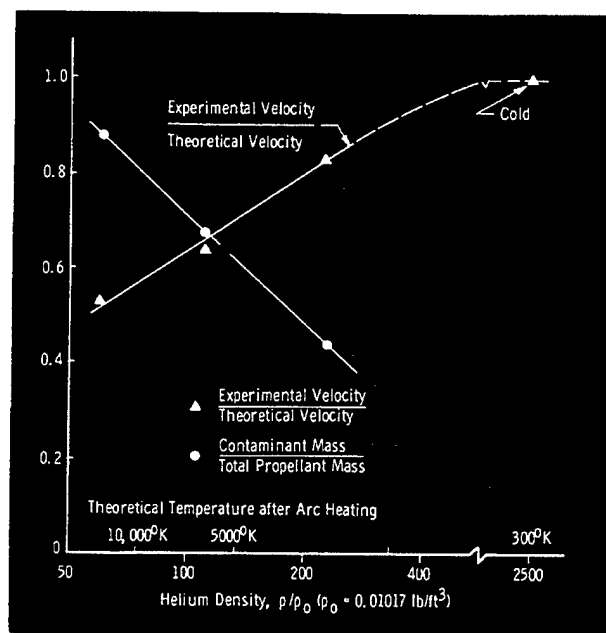


Fig. 1 20-mm Electric Launcher
- Contamination and Its Effect
on Launch Velocity (Ref. 2)

when the shock generated by the piston motion arrives at the end of the pump tube. Later, the high pressure that arrests the piston is transmitted down the launch tube to accelerate the projectile to high velocity.

A systematic analytical-experimental program was started (Refs. 3 and 4) to develop methods of computing the performance of two-stage launchers and of designing them for a specified performance. Reference 4 gives the design optimization procedure used for the large launcher for the VKF 1000-ft range, which is now being put into service (Figs. 3 and 4). The above studies led to the conclusion that useful improvement in launch velocity could be achieved by preheating

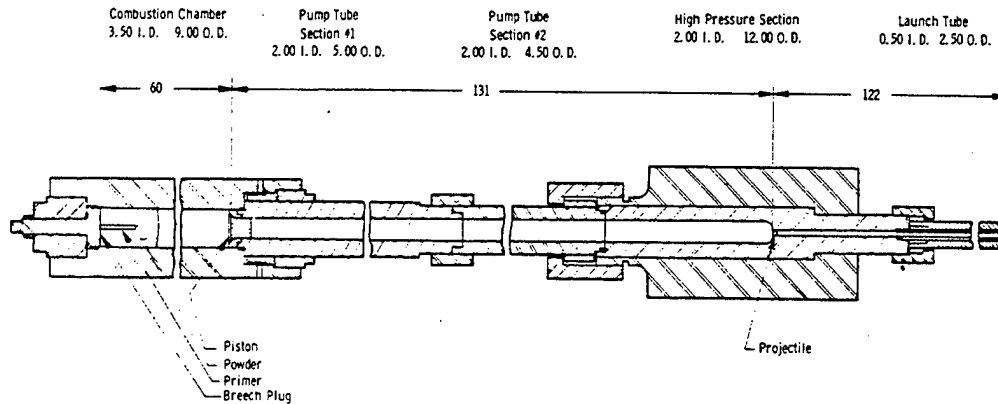


Fig. 2 Typical VKF Two-Stage Launcher

the propellant. A heating system was built and tested with the result that the velocity of an experimental launcher was increased from 27,500 to nearly 30,000 ft/sec at the same maximum pressure by doubling the propellant initial temperature (Fig. 5). These results are reported in Refs. 5, 6, and 7. The estimated effects of propellant preheating are shown in Fig. 6 for one of the VKF small launchers. Included also are the effects of projectile restraint. An unrestrained projectile is assumed to accelerate as soon as the first shock impinges on its base, whereas a restrained one is capable of resisting the first reflected shock pressure. It is apparent that the velocity gains decrease as the temperature increases. This effect is produced by heat losses and contamination, the maximum effective preheating temperature being limited to about 1000°K.

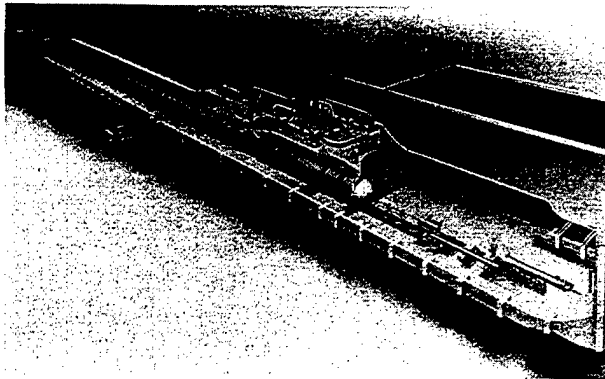


Fig. 3 1000-ft Hypervelocity Range

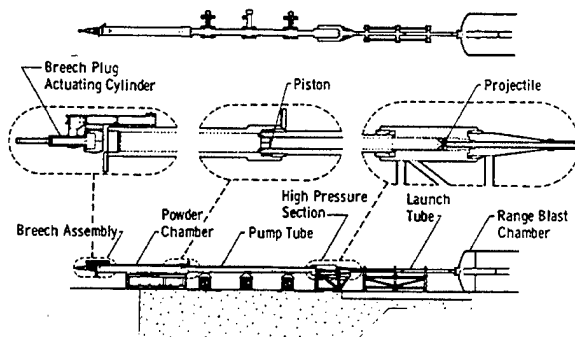


Fig. 4 8- by 2.5-in. Two-Stage Launcher

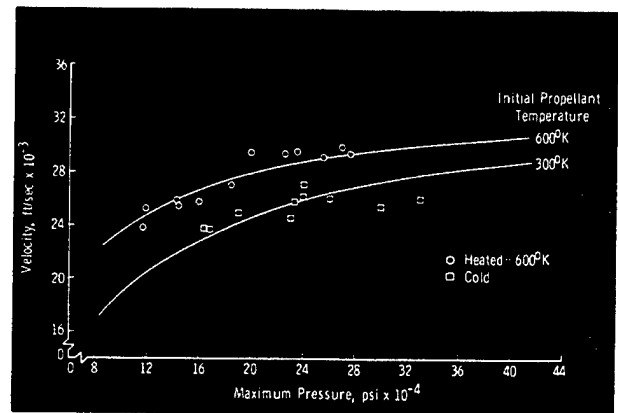


Fig. 5 Two-Stage Launcher - Effects of Maximum Pressure and Propellant Temperature on Launch Velocity (Ref. 6)

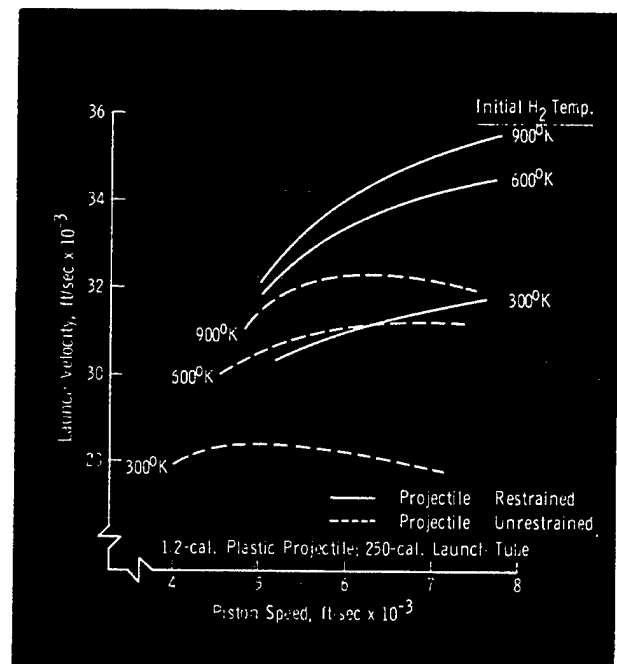


Fig. 6 0.5-cal Two-Stage Launcher - Calculated Performance at 20,000 atm Maximum Pressure with Heating and Projectile Restraint

Reference 8 presents performance calculations and experimental results for a small powder-driven launcher used in impact testing, and Ref. 9 gives some additional information on the effect of launch tube length (up to 400 calibers) on velocity for this launcher (Fig. 7).

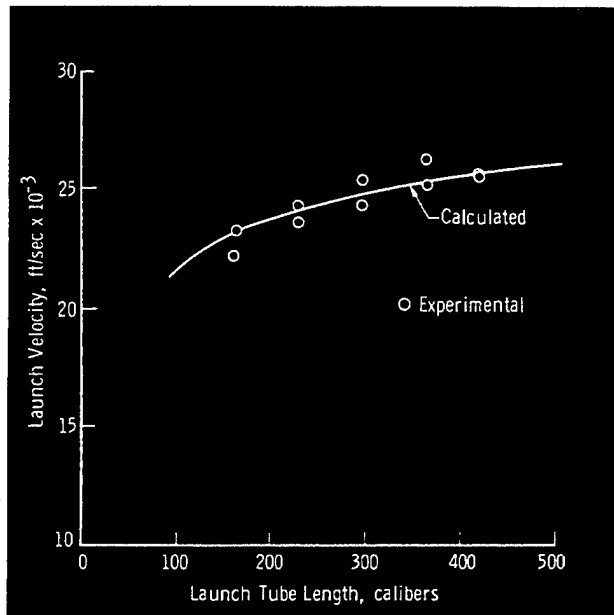


Fig. 7 0.3-cal Powder-Driven Two-Stage Launcher - Effect of Launch Tube Length (Ref. 9)

HIGH PRESSURE SECTION DESIGN

To achieve high velocities, it is necessary that quite high pressures (over 200,000 psi) be contained in the high pressure section and in the initial portion of the launch tube. In the course of the experimental program it was found that during the firings the ID of the high pressure section would grow. Figure 8 shows some of the measured diameters during a series of shots using a 6-in.-OD high pressure section (Ref. 6). The performance of the gun did not seem to deteriorate even though the ID of the nominal 1.58 in. section had grown above 1.75 in., with the piston apparently swelling and filling the increased diameter. This, then, indicated that, if necessary, the high pressure sections could be used to the full overstrain pressure (the pressure at which plastic flow reaches the outer wall) and perhaps even beyond.

The curves of Fig. 9 indicate the relative magnitudes of the pressures which can be contained by purely elastic behavior and by allowing the plastic flow to progress to the outer wall. Shrink fit of two concentric cylinders allows higher operating pressures than does a monobloc cylinder, but at pressure levels well below the overstrain value. The connections to the high pressure section are made far enough uprange and downrange of the maximum pressure region so that the seals do not experience pressures over 100,000 psi, a pressure which can be accommodated by conventional sealing methods. The inside of

the high pressure section can be made with a taper which corresponds to an inversion of the expansion expected at the overstrain pressure, so that after stressing, the inside diameter is almost constant.

It should be noted that a constant yield stress throughout the wall is assumed in the equations for calculating the overstrain pressure, and that the elongation of the material has to be sufficient to allow the radial growth. When the wall thickness of a material such as SAE 4340 is over 3 in., it is difficult to heat treat uniformly, and a multi-layer construction with some shrink fit between sections becomes desirable. The shrink fit increases the over-strain pressure only slightly. To allow sufficient elongation and to maintain high impact strength, it has been found necessary to keep the hardness of the SAE 4340 or H-11 type materials

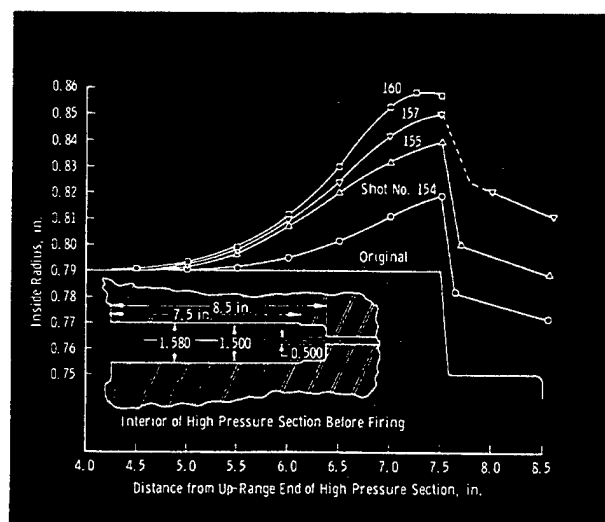


Fig. 8 Growth of Bore of High Pressure Section

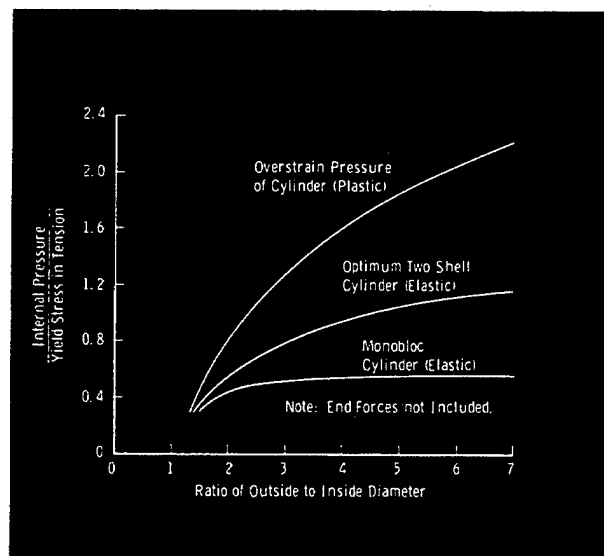


Fig. 9 Comparison of Internal Pressure Capability for Different Construction Methods

below a Rockwell "C" hardness of 40. This hardness usually gives a yield strength near 185,000 psi, and with an outside-to-inside-diameter ratio of 5, the maximum operating pressure is 350,000 psi.

REFERENCES

1. Lord, M. E. "Performance of a 40 mm Combustion-Heated, Light-Gas Gun Launcher." AEDC-TN-60-176, October 1960.
2. Lukasiewicz, J., Stephenson, W. B., Clemens, P. L., and Anderson, D. E. "Development of Hypervelocity Range Techniques at AEDC." AEDC-TR-61-9, June 1961.
3. Stephenson, W. B. "Theoretical Light Gas Gun Performance." AEDC-TR-61-1, May 1961.
4. Stephenson, W. B. and Anderson, D. E. "Design of a Large Two-Stage Light-Gas Model Launcher." AEDC-TR-61-6.
5. Stephenson, W. B. and Anderson, D. E. "Performance of Two-Stage Light Gas Model Launchers." IAS 30th Annual Meeting, New York, January 1962; also Aero-space Engineering, August 1962.
6. Anderson, D. E. and Prince, M. D. "Design of Light-Gas Model Launchers for Hypervelocity Research." Second Symposium on Hypervelocity Techniques, Denver, Colorado, March 20-21, 1962; also AEDC-TDR-62-97, May 1962.
7. Stephenson, W. B. and Knapp, R. E. "Performance of a Two-Stage Launcher Using Hydrogen." AEDC-TDR-62-32, March 1962.
8. Stephenson, W. B. "Performance of a Small Two-Stage Light Gas Gun Used for Impact Testing." AEDC-TN-61-166, January 1962.
9. Stephenson, W. B. "Investigation of High Speed Impact." Aerospace Engineering, November 1962.

HYPERVELOCITY RANGE MEASUREMENTS

By

P. L. Clemens

SHADOWGRAPH SYSTEM

In the VKF 1000-ft Hypervelocity Range, a multi-station shadowgraph system will provide data correlating projectile position and attitude with time. A severe set of performance requirements dictated the design of these shadowgraphs. In addition to the customary criteria demanding brief (i.e. submicrosecond) exposure duration and large field of view, the shadowgraphs were required to be impervious to the effect of the self-luminous shroud of gases enveloping the projectile. The use of ultra-high-speed shutters (e.g., Kerr cells or Faraday shutters) was to be avoided in order that the cost of the shadowgraphs not be excessive, and this meant that flash source intensity and optical efficiency had to combine to "overpower" the effect of the self-luminosity of the projectile. Otherwise, a meaningless smear of light would appear across the shadowgram, masking whatever projectile image the light source might have made latent. Extremely intense light sources tend inherently to be long duration sources, and a compromise here is difficult to achieve.

It was considered desirable that the bulk of the shadowgraph equipment be located outside the range tank to reduce its vulnerability to destruction by wayward projectiles and to facilitate its maintenance. The need for high optical efficiency implied that refocusing optics were required, and this requirement, together with that for a large view field, seemed to demand either the use

of large mirrors within the range or of large windows or both. Either of these alternatives would have run contrary to the desire that costs be kept low.

The solution which was chosen involves the use of simple, inexpensive, plastic Fresnel lenses in a design (Fig. 1) proven in the VKF 100-ft Hypervelocity Pilot Range. (Reference 1 presents a detailed analysis of the optics of this shadowgraph.) A spark light source of 1/10-microsecond (μ sec) duration provides the illumination which silhouettes the projectile against the Fresnel lens. With the exception of the 41-in.-diam Fresnel lenses, all shadowgraph components are located outside the range tank, relieving their vulnerability and facilitating their maintenance. Surveyed fiducial indices inscribed on each lens encasement serve as references in assessing projectile position and attitude. Although the optical quality of the Fresnel lenses is not great, resulting shadowgrams (Figs. 2a and b) yield adequate data. (It is intended that flow visualization be provided by a single, high performance schlieren system.)

Regardless of the quality of the optics, the shadowgraph is useless unless the 1/10- μ sec spark discharge of the point light source coincides with the arrival of the projectile within the field of view of the shadowgraph. In systems of ordinary design, recognition of the projectile and triggering of the spark source is done photoelectrically by a light screen device. An electric photo-detector and a light source face one another

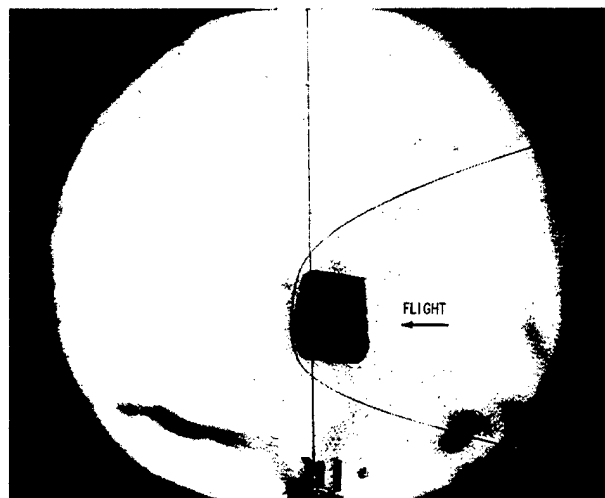
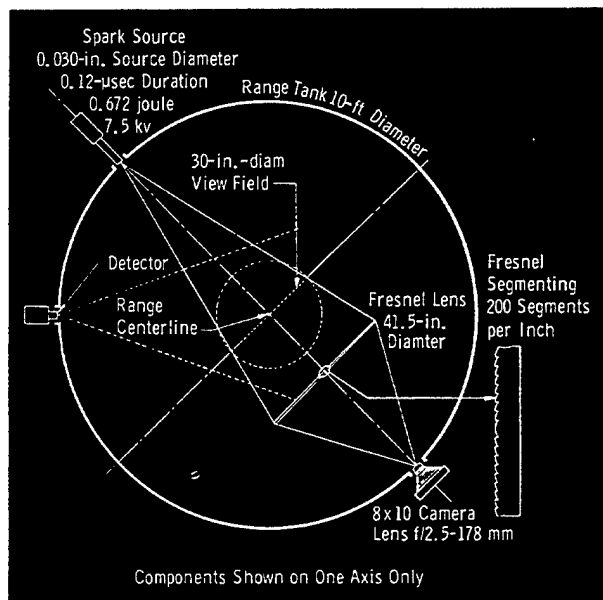


Fig. 2a Hypervelocity Range Shadowgraph; 40-mm, 0.5-cal Cylinder at 11,500 ft/sec; 20-mm Hg Range Pressure

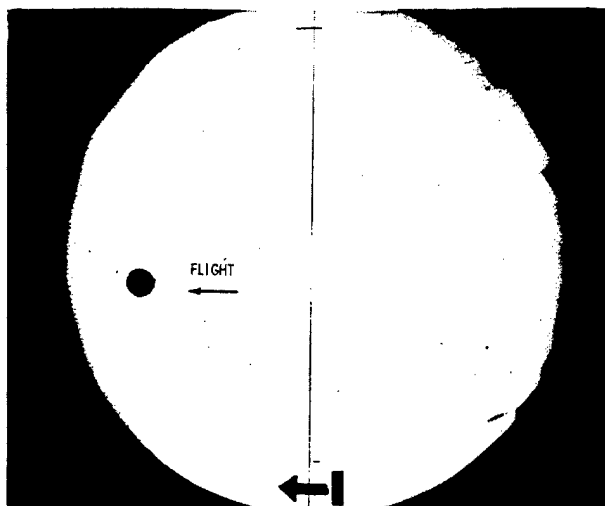


Fig. 2b Hypervelocity Range Shadowgram; 0.5-in., 0.5-cal Cylinder at 26,200 ft/sec; 1.5 mm Hg Range Pressure

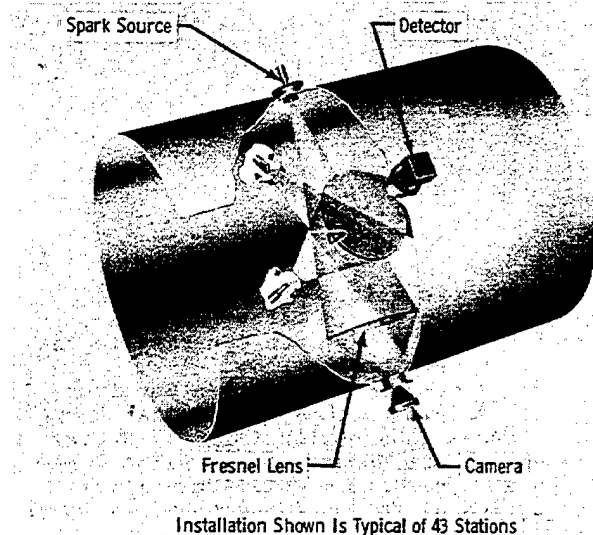


Fig. 1 Fresnel Lens Shadowgraph Configuration

from opposite sides of the trajectory. As the projectile passes between the detector and the source, the detector is partially shaded and its electrical output pulse triggers the discharge of the shadowgraph spark source. This conventional light screen system has several severe disadvantages.

First, the continuous light source which illuminates the detector must be ripple-free if variations in illumination intensity are not to be mistaken by the detector for passing projectiles.

Second, if a large field of view is to be covered and small projectiles are used, shading of the detector by the projectile becomes minute, and the signal-to-noise ratio of the detector limits its ability to recognize passing models.

Third, light from the continuous source exposes the film in the cameras used in the shadowgraph. This occurs because camera shutters are left open throughout the flight of the model, and shadowgraph exposure is limited only by the duration of the spark source output. To prevent fogging of the film by the continuous source, elaborate baffling becomes a requirement, and the light screen detector must be located up-range from the shadowgraph. This introduces another complication in that delay circuits must be used, and projectile velocity must be anticipated so that the shadowgram exposure will be properly synchronized.

Fourth, at high velocities the gas around the projectile is self-luminous. The intensity of this self-luminous glow may equal or exceed that of the continuous source

which is viewed by the detector; hence, this glow is ill-suited to casting a shadow. By increasing the intensity of the continuous source to accommodate variable luminosity, the saturation limit of the detector is approached, and the sensitivity of the detector suffers.

An improved projectile detector system which overcomes these difficulties has been developed within the VKF. A transistorized detector (Fig. 3) views the darkened wall of the range beyond the model's trajectory. (A complete description of the circuitry of this detector is found in Ref. 2). As the projectile with its self-luminous shroud enters the view field of the detector, it is recognized and a pulse is generated which triggers the spark source. Darkening of the range wall opposite the detector ensures that no stray light, as from the muzzle blast, will be reflected into the detector. Since the detector views a dark field rather than a light screen, it is located to coincide with the shadowgraph, and no delay circuit is required nor is the film in the camera fogged by exposure to a continuous source.

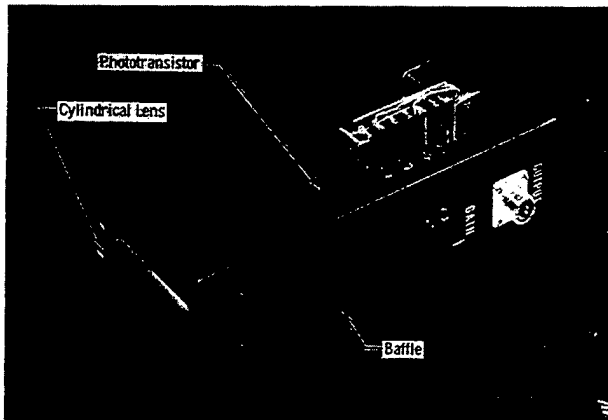


Fig. 3 Luminosity Detector

The luminous intensity of the gaseous flow which cloaks the projectile diminishes as projectile velocity decreases. Self-luminosity is also lessened as the projectile encounters atmosphere of decreasing density. Thus, there will be a velocity-density profile at which a dark-field detector will fail to recognize passing projectiles. Typical range of operation of a dark-field detector is shown in Fig. 4 in terms of ambient density and projectile velocity.

Although the shaded operating region of Fig. 4 accommodates the vast majority of test circumstances, infrequent occasions arise when combined projectile velocity and range density fall outside this zone. In these instances, a light screen detection system serves. Use of red lamps with blue camera filters and the application of careful baffling attenuates the effect of the detector source light on resulting shadowgrams.

TELEMETRY FOR AEROBALLISTIC RANGES

Conventional experimental techniques used in aeroballistic range testing provide only

those measurements which can be made by external observation of the aerodynamic projectile and its flow field. The usefulness of the aeroballistic range for aerodynamic tests would be significantly increased if, in addition, direct measurements of model surface pressures, temperatures, and heat-transfer rates could be made. It is with the view of achieving this goal that methods of telemetering from models launched into a variable density range have been under development in the VKF during the past few years (Refs. 3-6).

Development of a telemeter suitable for application to aeroballistic range work is riddled with difficulties, the most serious being small size and extreme acceleration during launching. A telemeter-equipped model may have to withstand structural loads resulting from application of nominal pressures up to 200,000 psi; under these severe conditions, it must preserve not only its structural integrity but also its calibration.

To facilitate the evaluation of test results during the early phases of development, it was considered desirable that the telemetered variable should lend itself well to static calibration, and also that it should be one for which in-flight theoretical values might readily be determined. Of all variables considered, stagnation pressure

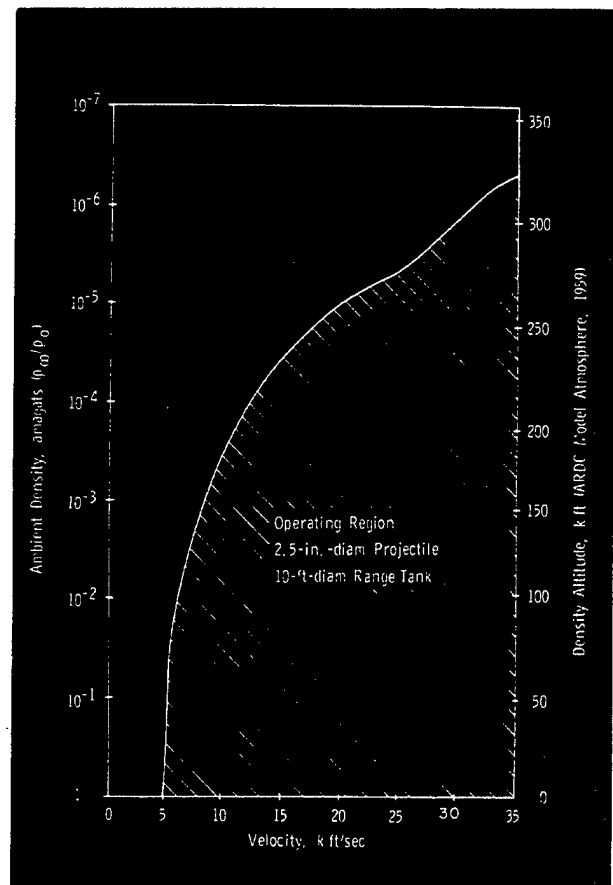


Fig. 4 Operating Region of a Dark-Field Detector

appeared most nearly to fulfill these requirements (Ref. 4). For convenience, simple cylindrical models (Fig. 5) are used for telemetry development.

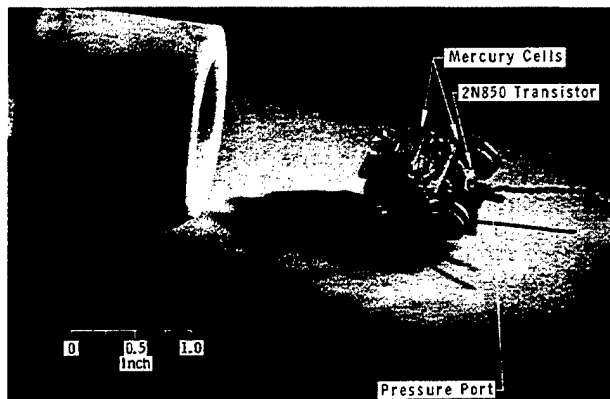


Fig. 5 Pressure Telemeter and Body Shell

The telemeter circuit in current use appears in Fig. 6. The nominal center frequency for this modified Colpitts FM oscillator is 150 mc. The variable capacitance pressure transducer has a quiescent value of 3 pf, and full-scale pressure excursions alter its capacitance to produce a shift in the r-f signal of 600 kc. Transducers accommodating full-scale pressures of 0.3 to 100 psia have been constructed, and tests involving their use are now in progress.

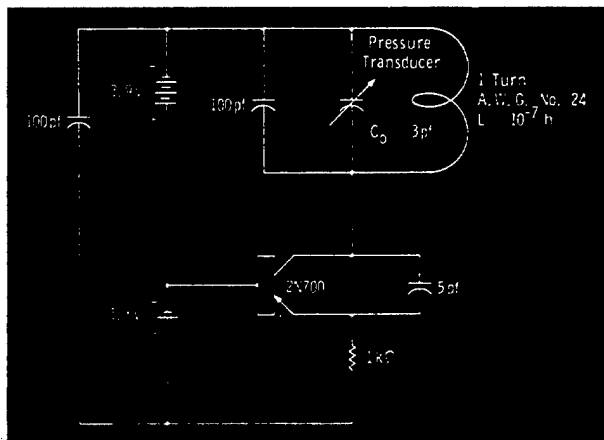


Fig. 6 150-mc Telemeter Circuit

Typical data telemetered from a model in flight through a range at atmospheric pressure appear in Fig. 7. The nominal peak acceleration experienced by the model during launching in this case was 215,000 g. Telemetered stagnation pressure data are compared with corresponding theoretical pressure values. The notch-like depression in the pressure data resulted from the flight of the projectile through a helium-filled, in-flight calibration chamber (Ref. 5). The data telemetered during this flight differed from the theoretical curve by some 18 percent

of full-scale pressure. The amplitude of the excursion in telemetered pressure, corresponding to the flight through the helium-filled calibration chamber, reveals that sensitivity of the telemeter in flight differed by 11.6 percent from that established during static calibration before launching.

Tests made with telemeters which did not contain transducers have shown that the telemeters continue to function in flight after launching at nominal peak accelerations up to 560,000 g. It has become evident that, at present, the transducer is the most limiting single component within the pressure telemeter (Ref. 6).

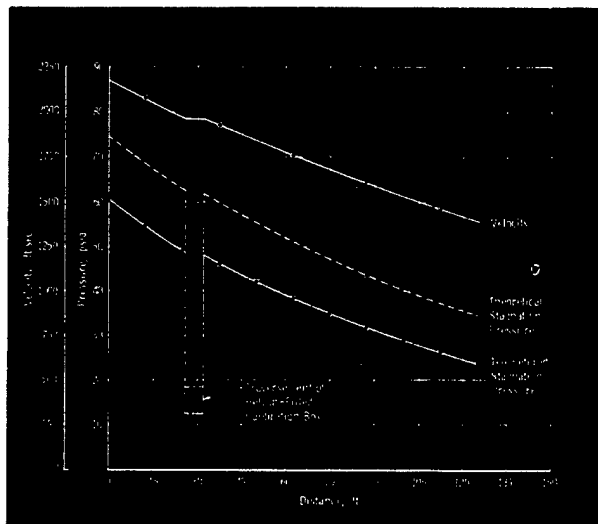


Fig. 7 Comparison of Theoretical with Telemetered Data

PROJECTILE KINEMATICS WITHIN LAUNCHER BARRELS

The kinematic behavior of projectiles in launcher barrels and of free pistons in pump tubes is of great interest in the development of hypervelocity range launchers and radio telemeters. An assortment of instrumentation systems has been used by various investigators in attempts to obtain data describing projectile kinematics. Crusher switches have been installed at stations along the length of launcher barrels to indicate arrival of the projectile at a few discrete positions. The use of similarly disposed pressure transducers has been tried. Attempts have also been made to infer interior ballistics from barrel strain measurements. Shortcomings are evident in each of these schemes. Crusher switches require modification of the barrel. They usually have low reliability, absorb energy from the projectile, and present the risk of damage to the round. Pressure measurements also require barrel modification. Like crusher switches, they limit kinematic

data to the few stations at which transducers have been installed. In addition, they introduce the considerable inconvenience of time-lag in pressure transducer response. Little needs to be said of the complications in dynamic loading of structures which must be considered if barrel strain measurements are to be exploited as a means of determining projectile velocities and accelerations during launching.

There is remarkable similarity between the ordinary launcher barrel with its projectile and the classical cylindrical wave guide with a movable shorting stub. This similarity suggests microwave reflectometry as an attractive means of measuring projectile kinematics. Barrel modification in most cases is limited to the installation of a single, simple antenna. Projectile position data are taken continuously rather than taken only at discrete barrel stations. Frequency response of microwave apparatus is more than sufficient to accommodate the launcher velocities encountered.

The results obtained from the microwave reflectometer system when used to instrument both 20- and 40-mm barrels have been quite satisfactory (Refs. 1 and 7). Figure 8 indicates the time history of projectile displacement during a firing of a 40-mm, single-stage, cold-gas gun. The broken curve indicates the fitting of a computed expression to the empirical data. The value of peak acceleration, found by double differentiation of the equation for the computed curve, agrees within some 8 percent with results obtained using another method.

REFERENCES

1. Clemens, P. L. and Hendrix, R. E. "Development of Instrumentation for the VKF 1000-ft Hypervelocity Range." Proceedings of the Second Symposium on Hypervelocity Techniques, sponsored by the University of Denver, Denver Research Institute, March 1962 (Proceedings published by Plenum Press).
2. Bock, O. H. and Clemens, P. L. "Aerodynamic Measurements in a Hypervelocity Gun Range." Electronics (McGraw-Hill), Vol. 34, No. 44, November 1961.
3. Kingery, M. K. "Hypervelocity Telemetry Experiments at the Arnold Engineering Development Center." Proceedings of the 1958 National Symposium on Telemetry, sponsored by the Institute of Radio Engineers, Miami Beach, Florida, September 1958.
4. Clemens, P. L. and Kingery, M. K. "Development of Instrumentation for a Hypervelocity Range." AEDC-TN-60-230 (AD-248572), December 1960.
5. Kingery, M. K. and Clemens, P. L. "An Assessment of Readout Errors Encountered in Radio Telemetry from Gun-Launched Hypervelocity Projectiles." AEDC-TN-61-58 (AD-256778), May 1961.
6. Lukasiewicz, J. et al. "Development of Hypervelocity Range Techniques at Arnold Engineering Development Center." AEDC-TR-61-9 (AD-258782), June 1961.
7. Hendrix, R. E. "Microwave Measurement of Projectile Kinematics within Launcher Barrels." AEDC-TDR-62-213 (AD-288923), November 1962.

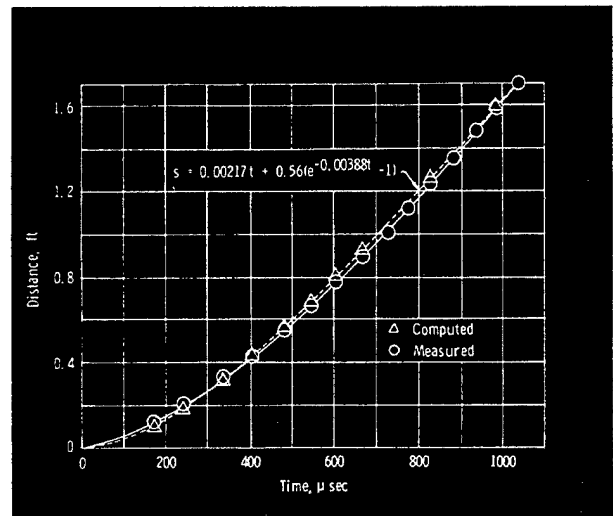


Fig. 8 Projectile Displacement vs Time

INSTRUMENTATION

It is a truism to state that an experimental test facility is never better than the instrumentation with which it is equipped. Recognizing this, a considerable effort has been devoted in the VKF to development of instruments and data handling systems, particularly for application to advanced types of wind tunnels and specialized measurements for which commercially produced instruments are not available. In fact, some of the transducers, originally developed in the VKF, have been eventually produced commercially and are being used in many domestic and foreign laboratories. Some highlights of the VKF instrumentation activities are described in this section.

DYNAMIC STABILITY MEASUREMENTS

By

L. K. Ward

The stability of a dynamic system, such as a vehicle in flight, is determined by its static and dynamic characteristics. A vehicle is statically stable if the forces and moments caused by a disturbance (such as, e.g., entry into atmosphere at a large angle-of-attack attitude) tend to bring it to its equilibrium attitude; it is dynamically stable if its response is damped, i.e., the amplitude of the motion decreases with time.

Two techniques are used in VKF to measure dynamic damping of models in wind tunnels. The free-oscillation technique involves displacing the model to some initial amplitude, releasing it, and monitoring the ensuing oscillatory motion. Damping data are then obtained by determining the logarithmic decay of amplitude with time. The forced-oscillation technique consists of oscillating the model at a constant amplitude, whereby the forcing torque required to sustain the oscillation is monitored. The forced-oscillation balance systems include an amplitude controller which provides positive amplitude control for testing both positively and negatively damped configurations.

Dynamic test data, obtained with either of the two methods, are converted into a digital form by a Beckman 210 analog-to-digital converter and recorded on a magnetic tape, which is then processed by an IBM 7074 computer to obtain dynamic stability coefficients. This automatic data handling system provides test results quickly and with a high degree of precision.

Development of dynamic stability balance systems and associated equipment began in VKF in 1956 for use in supersonic wind tunnels (Refs. 1, 2, and 3). In order to apply these systems to tests in hypersonic wind tunnels (Mach 8 and 10), the problems of balance cooling and of measurement of usually small aerodynamic damping at hypersonic Mach numbers had to be resolved.

Cooling of balance systems was satisfactorily achieved with the use of water jackets on the basic sting assembly; however, the forward section of the balance could not be water cooled since water passing across the pivot axis would introduce additional tare damping into the system. This problem was resolved by the use of high pressure air sprays in the region of the model attachment bulkhead, as indicated in Fig. 1; the sprays are operated when data are not being obtained.

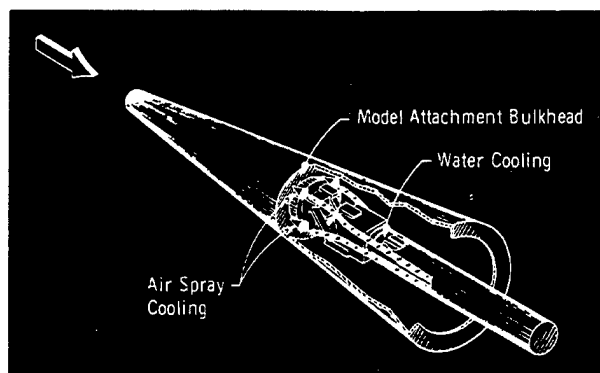


Fig. 1 Cooling of Model Balance Systems for Hypersonic Dynamic Stability Measurements

The problem of the precision of measurements at hypersonic speeds is illustrated in Fig. 2. At the higher Mach numbers the aerodynamic damping becomes a very small percent of the total damping as measured with the cross flexure balance system. Since the aerodynamic damping is obtained as a difference between total damping and tare damping precise evaluation of the system tare damping is required. It should be pointed out that Fig. 2 relates to a balance with 45-deg cross-flexures at the pivot axis which has very low structural damping.

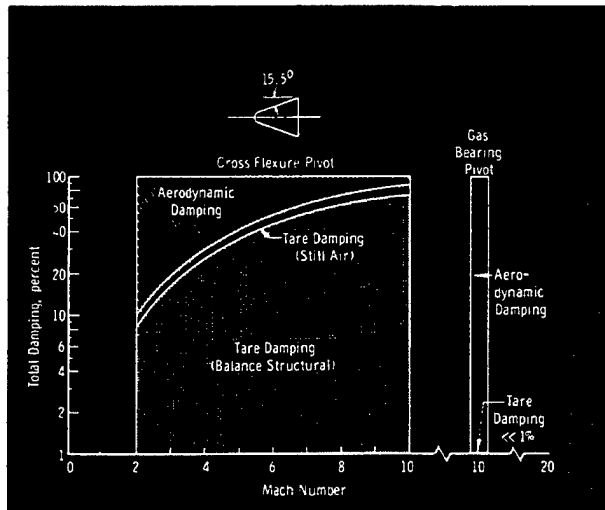


Fig. 2 Aerodynamic Damping Measurements

Incidentally, it is interesting to note in Fig. 2 the magnitude of the still-air tare present. If the tare value of the system were not evaluated under vacuum conditions, the still-air tare would appear as aerodynamic damping, thus giving large errors at the higher Mach numbers.

In spite of the difficulty indicated in Fig. 2, a considerable amount of dynamic stability data has been obtained by VKF at Mach numbers up to 10, using conventional balances with cross-flexure pivots. More recently, as a result of continuing effort to reduce tare damping, a gas (nitrogen) bearing was developed in VKF (Ref. 4) for use in free-oscillation type balances at supersonic and hypersonic Mach numbers.

With this type of pivot the tare damping is extremely low; for the particular model shown in Fig. 2, it is negligible even at Mach 10, as indicated on the right of the figure.

The nitrogen bearing can be used with either sting- or transverse-rod supported systems. A special angular displacement transducer (see page 77) has been developed in VKF for use with the freely oscillating balances.

At this time, dynamic damping data can be obtained in VKF in the Mach number range from 1.5 to 10 at oscillation amplitudes up to ± 180 deg. Work is now in progress on a balance system designed for use in the 50-in. Hypervelocity Tunnel (H) (see page 52) in the Mach 20 range.

REFERENCES

1. Welsh, C. J. and Clemens, P. L. "A Small-Scale Forced-Oscillation Dynamic Balance System." AEDC-TN-58-12, June 1958.
2. Welsh, C. J., Hance, Q. P., and Ward, L. K. "A Forced-Oscillation Balance System for the von Kármán Facility 40-by 40-Inch Supersonic Tunnel." AEDC-TN-61-64, June 1961.
3. Welsh, C. J., Ledford, R. L., Ward, L. K., and Rhudy, J. P. "Dynamic Stability Tests in Hypersonic Tunnels and at Large Model Amplitudes." AEDC-TR-59-24, December 1959.
4. Hodapp, A. E., Jr. "Evaluation of a Gas Bearing Pivot for a High Amplitude Dynamic Stability Balance." AEDC-TDR-62-221, December 1962.

TRANSDUCERS

By

D. S. Bynum

TRANSDUCERS FOR HOTSHOT TUNNELS (Ref. 1)

REQUIREMENTS

The hotshot-type tunnels impose several unique and severe requirements on transducers used to measure the parameters of interest. One is the rejection of electrical noise, both electrostatic and electromagnetic, which results from the high currents and voltages of the arc discharge. (Careful shielding and grounding, and the use of low impedance circuits are necessary to reduce the electrical interference to a negligible level.) Another requirement is the time response. In general, 10 to 20 msec are required for the test section flow to be established, and the usable flow lasts for about 40 msec. At the termination of the usable flow, severe

turbulence is encountered with the test section pressure increasing as much as an order of magnitude. Model pressure, heat-transfer rate, and force transducers must have a sufficiently high frequency response to follow the flow rise time and sufficiently low frequency response to follow the quasi-steady conditions of the remainder of the run. Model and test section pressures range from 0.001 to 3 psia full scale, whereas typical arc-chamber pressures range from 10,000 to 20,000 psi. Heat-transfer rates from one to several hundred Btu/ft²-sec are encountered. Stagnation temperatures of 2,500 to 4,000°K are typical. Forces of less than one pound to more than 50 lb (in special cases) are imposed on the force transducers. Since the pressure transducers must be placed inside the model because of the time response

EXPERIMENTAL TECHNIQUES

problem, transducer size becomes a limitation. Heat-transfer rate and force transducers must also fit inside the test models. A 3-in. base diameter, 9-deg half-angle cone model might require as many as 25 pressure and heat-transfer transducers.

Transducers capable of meeting these requirements were not commercially available when the first hotshot tunnel began operation in the late 1950's. Some are now on the market as a result of AEDC-VKF transducer development.

PRESSURE

For arc-chamber pressure measurements, a strain-gage, pressure-vessel-type transducer has been developed. A cross-sectional view is shown in Fig. 1. Because of the high voltage developed between the arc chamber (where the transducer is mounted) and electrically isolate the transducer from its respective carrier amplifier by transformers in both the transducer power and signal leads.

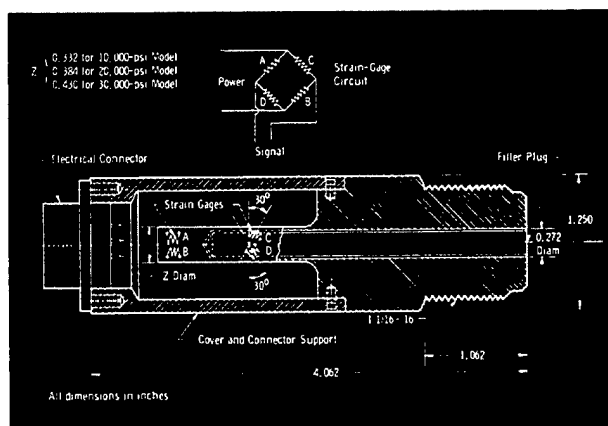


Fig. 1 Arc-Chamber Pressure Transducer

For model and test section pressure measurements, a variable-reluctance transducer has been developed. Typical transducer signal levels are 25 to 100 mv for 5-v, 20 kc excitation. The transducer is used in three configurations (see Fig. 2): (1) a standard wafer transducer (with mild steel case) for full-scale pressures from 0.05 to 3 psi (Ref. 2), (2) a low pressure wafer (same design as (1) but with an Invar case) for pressures from 0.001 to 0.1 psi, and (3) an acceleration-compensated fast response configuration for low pressure where model vibration adversely affects the uncompensated transducers and/or a shorter rise time is desired. The time response of the three configurations plotted versus absolute pressure is shown in Fig. 3. This is the result of much trial and error development of internal volume and shape of the transducers. Obviously, a reduction in internal volume should result in a shorter rise time. As this was carried to an extreme, an orifice was formed at the junction of the port and diaphragm. Potting (Meniscus

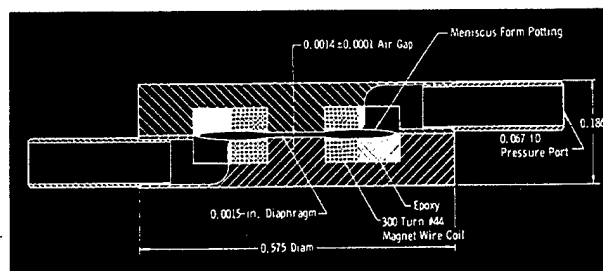


Fig. 2a Wafer Transducer Configuration

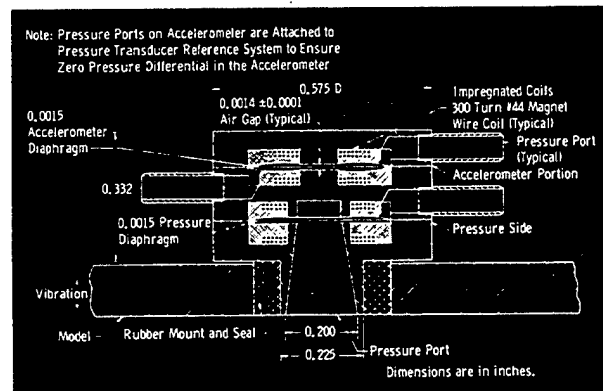


Fig. 2b Acceleration Compensated Transducer Configuration

potting, see Fig. 2) to form a circular channel around the wafer transducer and radial grooves in the fast response transducer shortened the response time as compared to the minimum volume configurations.

In the course of development of the low pressure wafer gage, a considerable change in sensitivity was noted when the absolute pressure level inside the transducer was changed from 1 atm down to a few thousandths of 1 psia. After a rather tedious investigation, it was found that the coil potting epoxy was defective. This allowed the coil geometry to change with pressure which in turn changed the transducer sensitivity. More rigid potting corrected the difficulty.

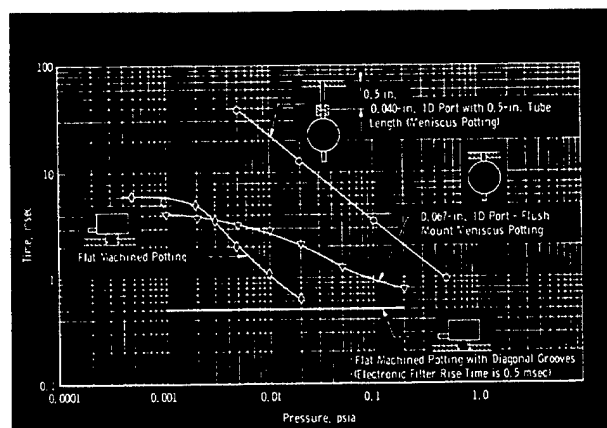


Fig. 3 Transducer and Associated Instrumentation Response Time

The acceleration-compensated transducer and its related instrumentation must be adjusted to cancel the effects of model acceleration in the data recordings. This is done by mounting the model in the tunnel, pumping the tunnel down to a few μ Hg, and then shaking the model with an eccentric weight on a motor shaft. Amplifier gain adjustments are then made so that the outputs from the transducer and its accelerometer exactly cancel. This procedure was first attempted with the tunnel at 1 atm and with the pressure transducer sensitivity set at 0.001- to 0.005-psi full scale. The signals never exactly cancelled, and very little compensation was achieved during the tunnel run. The trouble was found to be caused by the acoustics of the tunnel and the model pressure generated by the model motion. Evacuation of the tunnel produced good cancellation during the compensation adjustment and also good compensation during the tunnel operation (Ref. 7).

HEAT TRANSFER

Several types of transducers for measuring heat-transfer rate have been tried in the hotshot tunnels. The best results have been obtained from a calorimeter gage using a thermocouple temperature sensor, commonly called a thermocouple heat-transfer gage (Ref. 3 and Fig. 4). Even though the

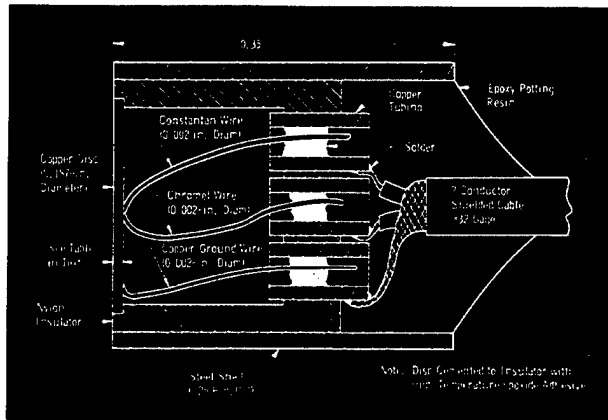


Fig. 4 Thermocouple Heat Transfer Gage

principle of this transducer is an old one, considerable development was necessary to overcome the calorimeter heat loss problem so that simple calorimeter theory could be used in the data reduction. Obviously, heat losses can take two paths: through the insulator and through the thermocouple and ground wires. The cement holding the disc to the insulator was found to account for most of the losses. Therefore, only the minimum amount of cement necessary to hold the disc in place is used.

Any transducer whose manufacturing tolerances introduce excessive unknowns in the theoretical sensitivity must be calibrated by applying a known input. In the case of the thermocouple gage, calibration is accomplished by applying a known heat-transfer rate with an oxyacetylene torch which has been calibrated with a standard calorimeter. The torch is rotated onto the gage by means of a solenoid, held there for about 80 msec, then released and moved off the gage by a spring. The calibration setup is shown in Fig. 5. In the case of the standard calorimeter, the application time is several seconds.

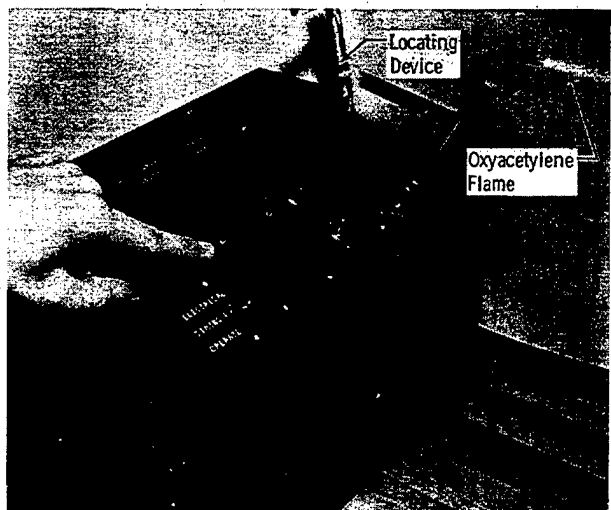


Fig. 5 Heat-Transfer Rate Calibration Torch

Some care is required in selecting the proper disc thickness for a particular heat-transfer rate. The disc must be thin enough to give a temperature rise sufficient to produce a measurable output voltage from the thermocouple during the useful part of the flow and thick enough to prevent overheating after the useful flow has terminated. Generally, the latter temperature rise is several times the former. The table below gives disc thickness for various heat-transfer rates as used in the AEDC-VKF hot-shot tunnels.

Disc Thickness, in.	0.002	0.003	0.005	0.010	0.020
Nominal Sensitivity, (mv/sec)/(Btu/ft ² -sec)	4.25	2.83	1.70	0.850	0.425
Recommended Range of Heat-Transfer-Rate Measurement Capabilities, Btu/ft ² -sec	1-15	4-25	8-40	15-75	30-150

FORCE

Force measurements in the VKF hotshot tunnels are made with strain-gage balances of the force type, i.e., no moment transducers are employed. A combination of light models and rigid force transducers generally produces natural frequencies ≥ 1000 cycles per second, sufficiently high to meet the frequency response requirements. Models are constructed of a combination of fiber-glass-reinforced plastic, balsa, and magnesium (Fig. 6). Typical model weights range from 0.1 to 0.2 lb in the 50-in. hotshot up to as much as 1.0 lb in the 100-in. hotshot.

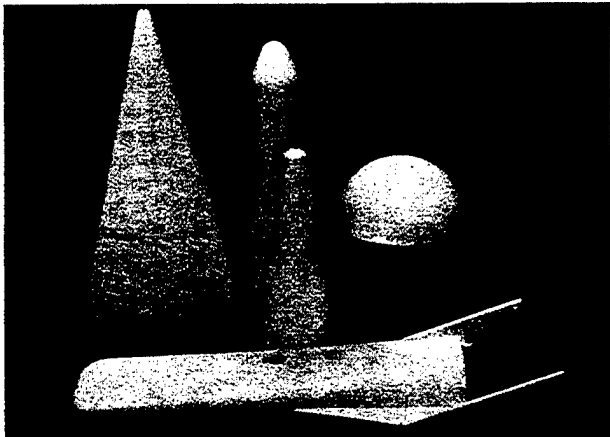


Fig. 6 Force Models Used in Hotshot Tunnels

For mounting in the tunnel, a sting-type support is used. The tunnel starting process initiates vibrations in the sting which are sensed by the model-balance combination acting as an accelerometer. The signal attributable to acceleration can be greater than the aerodynamic force being measured. The signals from accelerometers mounted in the balance are used to cancel the unwanted acceleration signals from the balance (Ref. 4). Adjustment is made while the sting is vibrated at its natural frequency by an eccentric weight on a motor shaft.

The hotshot tunnel starting process produces model loads which exceed several times the quasi-steady loads during the useful flow. Considerable difficulty has been experienced with zero shifts in the accelerometers because of the starting acceleration. This has been almost completely overcome by the use of semiconductor strain gages which allow more rigid and stronger structures.

One- and three-component balances have been developed and are in common use (Fig. 7). Some work has been done with six-component balances. The most difficult problem is the measurement of rolling moment. A moment transducer sensitive enough to detect the rolling moment is not rigid enough in conjunction with the model mass moment of inertia about its longitudinal axis to produce a sufficiently high natural frequency. The most promising results have been obtained using semiconductor strain gages.

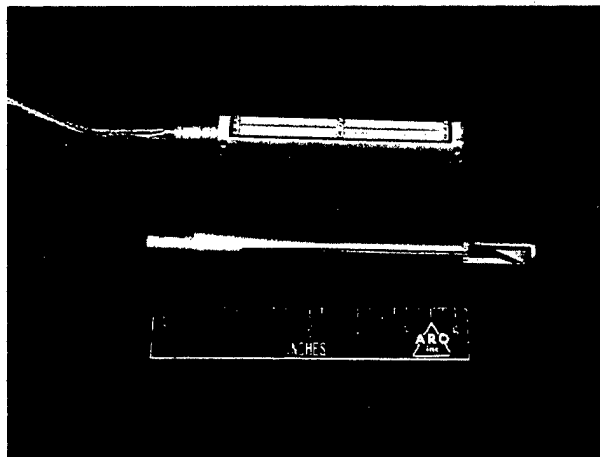


Fig. 7 Three-Component (Top) and One-Component (Bottom) Balances for Hotshot Tunnels

BALANCES FOR SUPERSONIC AND HYPERSONIC WIND TUNNELS

The continuous-flow supersonic and hypersonic wind tunnels in the VKF present a wide range of forces and ambient temperatures. A six-component balance design has evolved that can be adapted to the wide range of requirements. The balances are composed of mechanical strain-element-type force and moment transducers instrumented with electrical resistance strain gages. All forces and moments, with the exception of axial force, are derived from the moment transducer electrical signals using the appropriate laws of statics; axial force is measured directly with a force transducer.

When the model temperatures exceed the maximum allowable strain-gage temperature, a water-cooled jacket is employed. Water is transferred to and from the jacket with plastic tubing. The tubing is flexible enough so as not to interfere with the balance operation. Several typical six component balances are shown in Fig. 8.

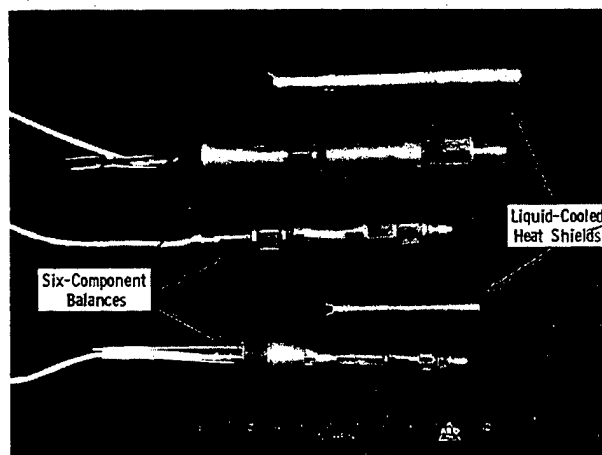
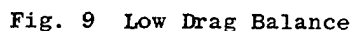


Fig. 8 Six-Component Balances and Liquid Cooled Heat Shields

SPECIAL TRANSDUCERS

In order to study viscous interaction in the AEDC-VKF hypersonic tunnels, it was necessary to employ models too small for an internal balance. Also, the axial forces were much smaller than the minimum ones for standard balances. To meet these requirements, an axial-force balance was developed with a maximum full-scale range of 0.3 lb. Forces as low as 0.002 lb have been measured with a repeatability of ± 5 percent. The device is a mechanical strain element with a linear-variable-differential transformer as a deflection sensor (Fig. 9). Power for the transformer and signal conditioning for the output signal are provided by a 20-kc carrier amplifier. Water cooling for both the model and the balance is provided. Provisions for helium ejection into the model boundary layer are also made.



In dynamic stability measurements in the wind tunnel, the fundamental parameter which must be measured is the attitude of

Model Mounting Pans Arr.
Attached to the Outer Ring

Section A-A

Note: Outer Ring

0.002 Bearing Clearance

0.002 Surface

Nitrogen Inlet for Bearing

Outer Ring

Inner Support

Transducer Housing (Attached to Inner Support)

Transverse Rod or Spline Is Attached to Ends of Inner Support

1.78

3.75

All dimensions in inches

The initial angular transducer design used ball bearings for support. The damping resulting from bearing friction was excessive as compared to the aerodynamic damping being measured. Therefore, a nitrogen bearing was developed to replace the ball bearings. Under similar conditions, the nitrogen bearing produces at least an order of magnitude less friction than a ball bearing support.

REFERENCES

- 77

EXPERIMENTAL TECHNIQUES

3. Ledford, R. L. "A Device for Measuring Heat Transfer Rates in Arc Discharge Hypervelocity Wind Tunnels." AEDC-TDR-62-64, May 1962.
4. Edenfield, E. E. and Ledford, R. L. "Compensation of Dynamic Sting Effects in Hotshot Force Measurements." AEDC-TDR-62-122, June 1962.
5. Welsh, C. J., Ledford, R. L., Ward, L. K., and Rhudy, J. P. "Dynamic Stability Testing in Hypersonic Tunnels and at Large Model Amplitudes." AEDC-TR-59-24, December 1959.
6. Hodapp, A. E., Jr. "Evaluation of a Gas Bearing Pivot for a High Amplitude Dynamic Stability Balance." AEDC-TDR-62-221, December 1962.
7. Smotherman, W. E., Maddox, W. V. "Variable Reluctance Pressure Transducer Development." AEDC-TDR-63-135, July 1963.